DOTTORATO DI RICERCA IN
SCIENZE DELL'INGEGNERIA

CICLO **XXXII**

COORDINATORE **Prof. TRILLO STEFANO**

APPLICATIONS OF COUPLED RESONATORS IN PHOTONIC INTEGRATED CIRCUITS

Settore Scientifico Disciplinare **ING-INF/02**

Dottorando
Dott. ALI EMRE KAPLAN

_____

Tutore
Prof. GAETANO BELLANCA

_____

Cotutore
Prof. PAOLO BASSI

_____

Anni **2017/2019**

Contents

List of Figures

x

List of Tables

List of Acronyms

AWG   Arrayed Waveguide Grating

BB   Building Block

BER   Bit Error Rate

B2B   Back to Back

CDC   Colourless, Directionless, Contentionless

CMOS   Complementary Metal Oxide Semiconductor

CMT   Coupled Mode Theory

CROW   Coupled Resonator Optical Waveguide

CW   Clock Wise

CCW   Counter Clock Wise

DC   Directional Coupler

DVS-BCB   divinylsiloxane-bis-benzocyclobutene

DUT   Device Under Test

DWDM   Dense Wavelength Division Multiplexing

EDFA   Erbium Doped Fiber Amplifier

ER   Extinction Ratio

EIT   Electromagnetically-Induced Transparency

FEM   Finite Element Method

FDTD   Finite Difference Time Domain

FMM   Film Mode Matching

FOM   Figure of Merit

FSR   Free Spectral Range

FWHM   Full Width Half Maximum

ICR   Indirectly Coupled Resonators

IL   Insertion Loss

iLOD   Intrinsic Limit of Detection

IMOS   InP-Membrane-On-Silicon

InP   Indium Phosphide

INT   Interleaver

ITU   International Telecommunication Union

LOD   Limit of Detection

MMR   Micro Ring Resonator

MUX	Multiplexer
MPW	Multi Project Wafer
MZI	Mach–Zehnder Interferometer
NoC	Network-on-Chip
OSA	Optical Spectrum Analyser
OLS	Optical Line Switch
PDK	Process Design Kit
PIC	Photonic Integrated Circuit
PSE	Photonic Switch Element
Q-factor (Q)	Quality factor
ROADM	Reconfigurable Optical Add/Drop Multiplexer
RIU	Refractive Index Unit
SEM	Scanning Electron Microscope
SOA	Semiconductor Optical Amplifier
SOI	Silicon-On-Insulator
SM	Single Mode
TE	Transverse Electric
TEC	Thermoelectric cooler
TM	Transverse Magnetic
TMM	Transfer Matrix Method
TLS	Tunable Laser Source
TPA	Transponder Aggregator
WDM	Wavelength Division Multiplexing
WSS	Wavelength Selective Switch

Chapter 1

Introduction

The developments in the photonic integration platforms endow the fabrication of Photonic Integrated Circuits (PICs) that can lead the way of the mass production of high performance optical devices at low cost. At present, PICs are considered as the complementary circuits to those of electronic integration to provide faster communication with lower power dissipation, mostly in fiber-optic communication. Other fields such as computing, sensing and neural networks are also in the interest of PICs. However, comparing to electronics, the photonic integration technology is still underway in terms of maturity and standardization. There is not yet a common agreement on a standard photonic circuitry template. One of the reasons is that PICs can be fabricated in different materials, while for electronic circuits, Silicon is the dominant material. Moreover, each fabrication facility has its own fabrication recipe which depends on the used materials, application type and design approach. Therefore, PIC design procedure requires preliminary information about the related platform (material, fabrication techniques etc.) and also so much effort to obtain the optimized device performance by the simulations and analysing the characterization results of test samples.

So far, photonic integration technologies considered different materials such as Indium Phosphide [1], Silicon [2–4] and Silicon Nitride [5]. The range of optical functions that can be carried out PICs depends on the material choose. For instance, Indium Phosphide (InP) based integration technology can support to monolithic integration of a semiconductor optical amplifier (SOA) for fabrication of integrated semiconductor lasers. Even though Silicon is not an efficient material for lasing due to its indirect bandgap, Silicon-on-Insulator (SOI) technology comes into prominence thanks to its Complementary Metal Oxide Semiconductor (CMOS) compatible fabrication process that can enable integration of optics and electronics on the same chip [6, 7]. Moreover, Silicon photonics benefits from high-index-contrast structures that can support to dense integration of small footprint PICs on chip. On the other hand, Indium-phosphide membrane on silicon (IMOS) integration scheme is a developing technology that aims the integration of InP based optical layer and Silicon based electronic layer on the same chip [8]. The IMOS technology is a promising candidate since it allows

also the integration of active devices and similar to SOI, it provides high-index-contrast structures.

The reproducibility with guaranteed performance of PICs is the main goal of a fabrication foundry. The concept so called "generic foundry approach" to PICs fabrication aims to expedite the procedures of design, fabrication and characterization of PICs [9, 10]. In generic foundry approach, the designers use the basic building blocks (BBs) provided by the Process Design Kits (PDKs). BBs are the elementary components, which can be assembled to compose more complicated structures. PDKs are the set of files regarding materials and device geometries to the model fabrication process. The number of BBs offered by a foundry determines a variety of applications that the foundry can offer. The design of a BB requires then strong interactions between theoreticians, able to create a numerical model of the considered device, and technologists, able to to fabricate and characterize the devices. They should mix their expertises to create a model able to describe the functional characteristics of the considered BB. Introducing novel photonic devices increases the inventory of PDKs and therefore, allows to design more complex circuits for advanced photonic applications in a time efficient way. The key factor of this way of working comes from the fact that the designer is not interested in the actual shape, geometrical feature an size of any component, but only in its transfer function or any other functional characteristic. The real device features are managed by the foundry which has rules to convert the required functionalities into physical characteristics.
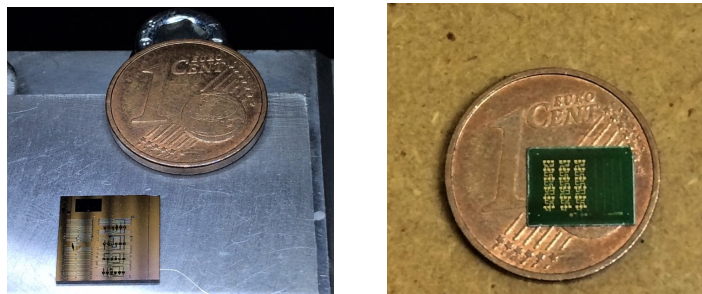
Figure 1.1: The characterized chip samples of SOI (*left*), fabricated by the INPHOTEC and IMOS (*right*), fabricated by the NanoLab@TU/e.

Moreover, further cost reduction is obtained by Multi Project Wafer (MPW) services in integration photonics which allow to reach more users, as they integrate a number of PIC designs on a wafer. The devices studied in this thesis have been fabricated through two MPW runs. The examples of the fabricated chips are shown in Fig. 1.1. The SOI PICs were fabricated by the INPHOTEC of the Scuola Superiore Sant'Anna, while the devices in IMOS platform were fabricated in the NanoLab@TU/e facilities of the Eindhoven University of Technology.

1.1 Motivations of thesis

Before describing the content of this thesis and the theoretical and experimental results obtained with this work, it seems important to me also to evidence the important personal and professional achievements I obtained during this PhD activity. I have been personally involved (as it will be explained later) in the theoretical modelling activity, developing original codes and using commercial CAD tools (COMSOL, Lumerical and OptoDesigner), in the design of the mask layouts for technological fabrication (OptoDesigner and Nazca Design), in the implementation of experimental setups (both in TU/e and UniFe), in the measurement of the realized devices and in the elaboration and the interpretation of the obtained results. This wide spread range of activities gave me an initially unexpected broad experience in this field where cross competences are reasonably expected both in photonic research and industrial environments.
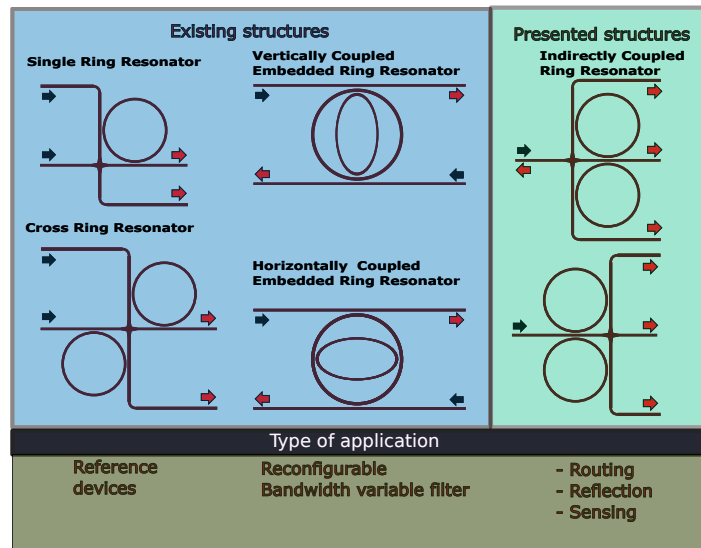
Figure 1.2: Schematics of the studied structures with their applications. The single ring and cross-grid ring resonator structures (*left column*) are considered as the reference devices for performance comparisons with the proposed devices (*right column*). The embedded resonators (or Eye-like ring resonator) (*middle column*) are only reviewed in terms of bandwidth variable add/drop filtering applications.

The presented research is focused on the design and characterization of a novel micro ring based coupled resonators aiming at introducing a new building block by investigation its performance for wavelength routing, reflection and sensing applications. Since the proposed device has two cavities that are coupled to each other via a bus waveguide, the structure is referred to as indirectly coupled resonators (ICR). Indirect coupling has an advantage from a design point of view. The preliminary design work regarding the coupler sections requires only the optimization of bend-to-waveguide coupling, which usually exists in PDKs of many fabrication facilities, since the single ring resonators are one of the basic building blocks. Consequently, once the single ring resonator parameters are well known, designing an ICR is straightforward. Setting up the second ring in the configuration allows to introduce new photonic functions such

as non-reciprocal wavelength routing, reconfigurable single or multiple wavelengths reflection and differential sensing.

Performance assessments of the studied ICRs are carried out by comparison of existing devices as shown in the blue coloured domains of Fig. 1.2, where the single ring and cross ring resonators have been considered as the reference devices. On the other side, the embedded ring resonators are reviewed in terms of bandwidth tuning capabilities. The characterized MRR based structures in this thesis are mainly fabricated in SOI technology, except an IMOS based ICR has been used as a supportive structure for the reflection analysis. The main contribution obtained from the IMOS devices in the presented research relies on the characterization of quasi-TE (Transverse Electric) and quasi-TM (Transverse Magnetic) polarized directional couplers.

1.2 Micro Ring Resonators

Optical ring resonators have been first proposed by Marcatili in 1969, to investigate propagation losses in waveguide bends [11]. Since then, micro ring resonators have been utilized in various applications, such as wavelength channel filters [12–14], laser cavities [15, 16], modulators [17, 18], switches and routers [19–24]. Recently MRRs are being considered also in the implementation of photonic neural networks [25–28]. MRRs can be fabricated in different integration technologies. However, Silicon based MRRs are of a particular interest in realizing compact CMOS compatible photonic circuits [29].
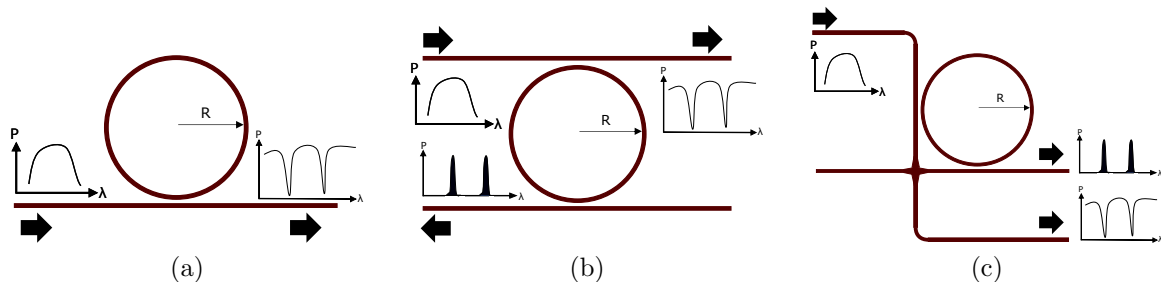
Figure 1.3: Type of single micro ring resonators: (a) all-pass, (b) add-drop, (c) cross-grid.

Ring resonators are often used with evanescent coupling to optical waveguides. A close-loop of a bend waveguide (it must not necessarily be circular. Alternatively, circular rings with longer rectilinear coupling regions are called racetrack) is placed in proximity of a bus waveguide where the power of the propagating light can couple into the resonator. The three types of configurations and their working principles are illustrated in Fig. 1.3. The basic configuration shown in Fig. 1.3(a) is called all-pass configuration. It consists of a straight waveguide and a ring resonator. In this configuration, the incoming wavelengths are either transmitted (non resonant wavelengths)

or stopped (resonant wavelengths) at the output port (through port). Resonant wavelengths of the resonator appear as transmission dips in the spectra. Separation of two consecutive resonances in wavelength domain depends on circumference of the resonator cavity and effective refractive index of the optical mode. The add/drop configuration shown in Fig. 1.3(b) retrieves individual resonance peaks at the bottom port due to the presence of the second waveguide that performs drop function. The same dropped wavelengths can be added to the through port transmission if the right-bottom port is used as an input port. As shown in Fig. 1.3(c), the cross-grid configuration uses a waveguide crossing to connect a cavity to two perpendicular waveguides. As the input and add ports are located in a row, cross-grid resonators allow to fabricate compact and scalable switching matrices.

Coupled Micro Ring Resonators

Single MRRs are categorized as first order resonators. Second and higher orders can be achieved by placing multiple rings in proximity so that, they become coupled resonators. A variety of the applications of coupled resonators depends on topological ways of cascading cavities. Externally and internally coupled resonators in all-pass configurations are shown in Fig. 1.4. The first scheme (Fig. 1.4(a)) called Coupled Resonator Optical Waveguides (CROWs) can be constructed by two and more resonators that are placed side by side to increase resonator order (referring to number of rings). On the other side, higher order rings can be embedded inside a ring cavity, as shown in Fig. 1.4(b). This structure is useful to make small footprint devices. But, the device order is limited by the first ring's area. Therefore, there is a trade-off between order number and footprint. Rotational position of the internal resonator can be freely chosen. Typical second order embedded rings have horizontally placed internal resonators. In this way, the overall structure resembles to an eye, thus they are sometimes called Eye-like ring resonators.

(a) (b)

Figure 1.4: Type of coupled micro ring resonators: (a) CROW (b) Embedded (Eye-like).

Precise control on the coupling and resonant wavelength of CROWs enables the implementation of various optical phenomena such as slow light [30], coupled-resonator induced transparency [31] as well as Fano resonances that can offer unique spectral characteristics. Fano resonances are known especially for their very narrow and sharp asym-

metric line shape [32]. As a special case of Fano resonance, the Electromagnetically-Induced Transparency (EIT) effect can be generated by two directly coupled resonators [33–35]. EIT effects can be created also in the embedded ring configuration that has been proposed and studied for many applications such as switching [36], modulation [37], sensing applications [38, 39] and slow light [40].

1.3 Indirectly coupled ring resonators

Up to now, we have introduced the ring configurations presented in the literature. In the following, we will present a new configuration based on indirect coupling. Unlike to the previously reported coupled resonators where the cavities have direct power exchange, indirectly coupled resonators in the cross-grid configuration are assisted by a bus waveguide placed between them and a waveguide crossing, as shown in Fig. 1.5. Therefore, coupling occurs in three-waveguide system in horizontal direction, while the vertical coupling sections remain the same as shown for the single ring configuration in Fig. 1.3(c). The reason of referring to this configuration as ICR has two aspects: firstly, the interaction of the resonators through the bus waveguide obeys a 3×3 coupling formalism and the interaction of the cavities exists through another waveguide (central bus waveguide). Secondly, resonance wavelengths of each resonator encounter the presence of the other ring due to the shared routing path that connects the two rings by a vertically placed straight waveguide. The former is valid when the rings are placed behind the crossing waveguides according to the input port (Type-I) as shown in Fig. 1.5(a).
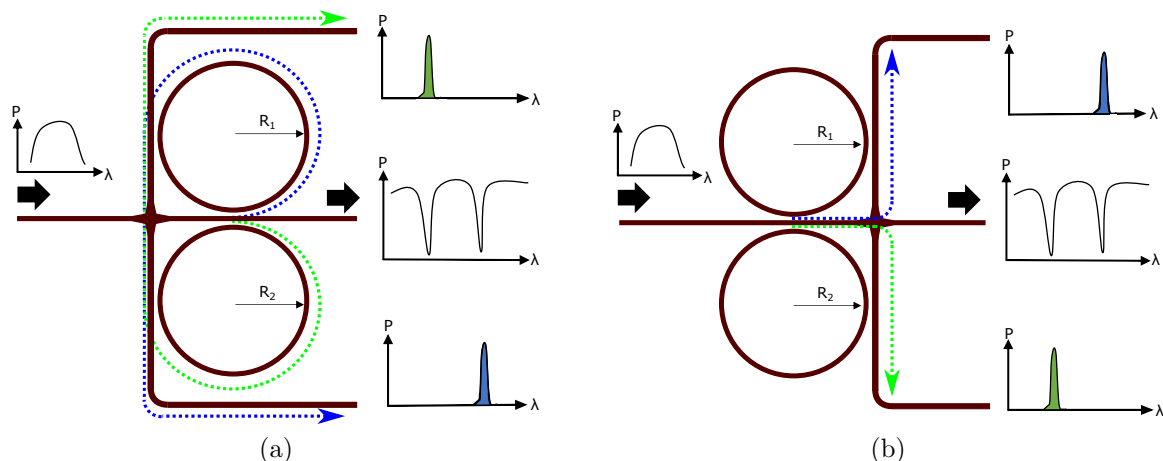
Figure 1.5: Wavelength routing of indirectly coupled resonators according to the position of the rings. Type-I (a) and Type-II (b).

If the rings resonate at different wavelengths, i.e., rings have different radii ($R_1 \neq R_2$), Type-I configuration has two resonance wavelengths present at the upper (Green) and bottom (Blue) drop ports, which are routed by the bottom and the upper rings, respectively. On the other hand, in Type-II configuration, rings are positioned in front

of the crossing. In this case individual resonances inversely route to the drop ports with respect to those of Type-I configuration (Fig.1.5(b)).

It can be said that the choice of the position of the coupled rings is not trivial, since wavelength routing behaviour of the device is non-reciprocal, meaning that Type-I and Type-II configurations can be interchanged simply by swapping the input and through ports. Moreover, when the rings resonate at the same wavelength, Type-I acts as a reflector and Type-II acts as a splitter. While the former will be investigated in details, the latter is out of the scope of the thesis.

ICRs can be operated in two working regimes depending on whether the rings have the same resonances. If so, we define such condition as synchronous (the same resonance wavelength) for reflection condition, otherwise non-synchronous (different resonance wavelengths), which allows wavelength routing. Each type of application that has been considered in this thesis requires a certain type of ICR in a defined operation. Operational functions of the device will be explained in Chapter 3.

1.4 Application fields for the assessment of ICR

We consider three different areas of applications to assess the optical features of ICR. A major part of research effort is spent on the applications concerning the wavelength routing properties of the proposed device for flexible optical networks and network-on-chip systems. Secondly, the device is analysed to investigate possible wavelength reflection applications. Finally, a theoretical work is developed in the field of biosensing applications. Each application of interest can be performed under the certain working conditions and type of device. Hence, the photonic functions of the ICR and the related application fields studied in the presented work can be grouped as follows:

- **Wavelength routing**

  Both Type-I and Type-II configurations are used to introduce the concept of bidirectional communication in a reconfigurable add/drop multiplexer architecture for wavelength division multiplexing (WDM) based flexible optical networks. Additionally, an ICR based switch fabric is confronted by conventional topologies in Network-on-Chip (NoC) systems in terms of scalability. For implementing wavelength routing operations, the device must be in non-synchronized condition.

- **Reflection**

  This application strictly requires synchronized condition in Type-I configuration. The same device can be switched from routing mode to reflection mode by thermal tuning of the rings via integrated heaters on-chip. SOI devices are characterized for single wavelength reflection. Transmission measurements of a racetrack ICR fabricated in IMOS are presented as an example of a reflection comb generation.

- **Sensing**

  In this application, both synchronized and non-synchronized conditions in Type-I configuration are needed to introduce differential optical sensing scheme. The synchronized condition supports to on-chip calibration process, while the non-synchronized condition is considered for measurement process. This application is studied only theoretically, by using analytical models developed in this thesis.

Different chapters are dedicated to each type of application. In each one, the related application background and research motivations are presented together with the results obtained from both simulations and experiments.

1.5 Thesis outline

The thesis is structured as follows:

In Chapter 2, the layer stacks of the SOI and IMOS technologies are introduced and basic waveguide propagation parameters are presented. The quasi-TE and quasi-TM mode directional couplers fabricated in the IMOS technology are experimentally characterized. In addition to standard S-bend curves, the presented directional couplers include ultra sharp bend corners that reduce the footprint and power coupling contributions induced by the bend sections. The results are discussed in terms of fabrication tolerances for optimum device performance and the validity of the coupled mode theory applied to high-index-contrast structures.

In Chapter 3, analytical models based on the Transfer Matrix Method are developed for the single ring, embedded rings and ICR structures. The experimental characterization results of the fabricated SOI single micro ring resonators are reported. Theoretical transmission characteristics of the ICR and the embedded rings are analysed for the working conditions of the desired applications.

Chapter 4 topologically investigates wavelength routing properties of ICRs, considered as novel photonic switching elements in the interest of WDM technology based Flexible Optical Networks and Network-on-Chip applications. By using non reciprocal wavelength routing properties of the ICR, the concept of bidirectional communication is introduced and used to propose a 2-direction 4-channel transponder aggregator (TPA) scheme for the next generation reconfigurable add-drop multiplexer systems. Moreover, scalability analysis of an ICR-based wavelength router topology is carried out and the results are compared with the conventional photonic switch element based on the cross ring configuration. Network communication performances of single silicon MRR, cross ring and ICRs are investigated by means of Bit-Error-Rate implemented with 10Gbps Dense WDM links.

In Chapter 5, the reflection properties of the Type-I ICR are studied. The conditions for driving the resonator in the reflection regime are experimentally tested and the results are presented. The required design parameters to increase the reflectivity are

addressed. In addition to the single wavelength reflection, the condition for multiple-wavelength reflection generation is commented and the measured reflection spectra of an ICR reflector fabricated in the IMOS platform is provided to demonstrate a comb reflection spectrum.

In Chapter 6, an ICR based differential optical sensing scheme is proposed and theoretically analysed. An on-chip sensor calibration method provided by the scheme is introduced. The presented assessments of the sensing performance are carried out by a comparison with the results obtained from an identically designed conventional single ring resonator based sensing scheme.

Finally, conclusions about the most important results achieved in this thesis are drawn in the last chapter together with future works that can follow the research presented in this thesis.

Chapter 2

Basic photonic circuit elements

In this chapter, we first introduce material systems of the SOI and IMOS technologies. Before discussing the components which are of interest for this thesis, it is in fact better to summarize the most important features of the materials which will be used to fabricate the devices and some of the features of the basic components used in the following: straight waveguides and directional couplers. These devices are the simplest BBs of more complicated PICs. Transmission measurements of single quasi-TE mode Si and InP waveguides are provided. Further, an experimental characterization of directional couplers fabricated in IMOS is presented. The content of this chapter is largely transcribed from the published article: Ali Emre Kaplan, Gaetano Bellanca, Jorn P. van Engelen, Yuqing Jiao, Jos J. G. M. van der Tol, and Paolo Bassi, "Experimental characterization of directional couplers in InP photonic membranes on silicon (IMOS)," OSA Continuum 2, 2844-2854 (2019).

2.1 Waveguide Layer Stacks

Waveguides are the principal elements of PICs where light propagates at a certain optical mode. The waveguide cross sections of SOI and IMOS integration platforms are illustrated in Fig. 2.1. In the SOI platform, the deep etched Silicon (Si) waveguide on the top of the SiO_2 cladding has 480×220 nm^2 cross section. On the other side, the deep etched Indium phosphide (InP) membrane core with the size of 400×300 nm^2 is bonded on an adhesive polymer, divinylsiloxane-bis-benzocyclobutene (DVS-BCB), that is used for wafer bonding of Si and InP [8]. While the SOI waveguides of the studied structures support only the single quasi-TE (*Transverse Electric*) mode, the InP waveguides support both quasi-TE and quasi-TM (*Transverse Magnetic*) modes. The structures characterized in this thesis were designed for the TE polarization except the directional couplers where also the TM couplers are considered. Therefore, modal analysis presented here is done for the fundamental quasi-TE mode and obtained by Finite Element Method (FEM) simulations [41].

The refractive index contrast of the core and cladding $\Delta n = (n_{core} - n_{cladding})/n_{core}$
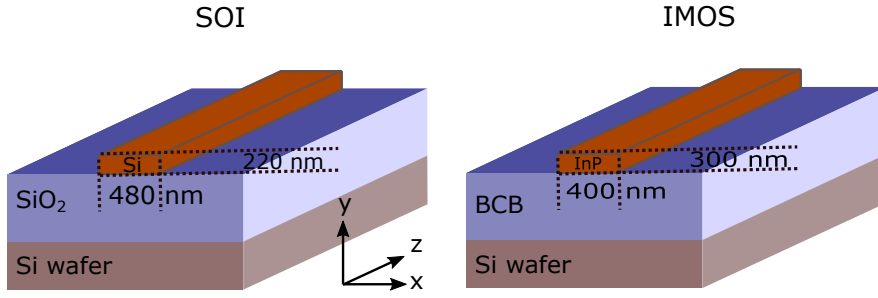
Figure 2.1: Cross sections of SOI (*left*) and IMOS (*right*) deep etched waveguides.

plays a critical role to realize compact devices. Even though scattering losses in waveguides increase at higher values of Δn, overall insertion loss of the device could be reduced since higher value of Δn increases the light confinement and therefore reduces the minimum bending radius [42]. Both integration schemes offer high index contrast structures by having the refractive indices $n_{Si} \approx 3.47$ and $n_{SiO_2} \approx 1.45$ for the SOI, and $n_{InP} \approx 3.17$ and $n_{BCB} \approx 1.5$ for the IMOS at wavelength $\lambda = 1550$ nm. The upper claddings, which are not visible in Fig. 2.1, have similar indices as the bottom claddings.

The effective index evolution with respect to wavelength can be seen in Figure 2.2, that shows the simulated effective refractive indices of the fundamental TE mode propagation in a wavelength range of 50 nm. The group index (n_g) is responsible for phase delay in cavity and can be calculated by using the slope of the effective index curves together with respect to λ and the relation $n_g(\lambda) = n_{eff}(\lambda) - \lambda(\partial n_{eff}(\lambda)/\partial \lambda)$ holds. The values of n_g and n_{eff} reported in Table 2.1 are used in the analytical models as the technology parameters.
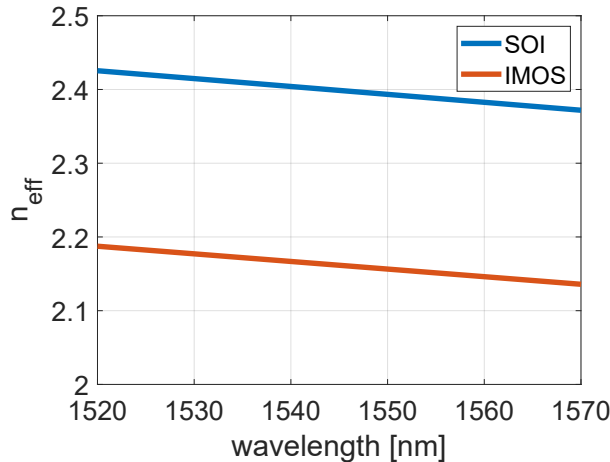
Figure 2.2: Effective refractive index of the fundamental TE mode in SOI and IMOS waveguides as a function of wavelength.

Figure 2.3 shows simulation results of the propagation losses in the bend sections due to power scattering expressed in dB per 90° for different values of the radius of curvature. The results are obtained through an OptoDesigner (Phoenix Software) script (provided during a training at INPHOTEC), which uses the Film Mode Matching

Parameter	SOI	IMOS
n_{eff}	2.40	2.15
n_g	4.08	3.75

Table 2.1: Effective refractive index and group index of the fundamental TE mode in SOI and IMOS waveguides at λ = 1550 nm.

Method [43]. The loss becomes significant below a 3 μm radius for the IMOS waveguides. On the other hand, the bend loss in SOI can be neglected down to about a radius of 2 μm. However, these results do not give any information regarding surface roughness based scattering losses since the calculated bend loss is based on modal field distributions. Therefore, it is most likely that fabricated waveguides would have more losses than expected. Furthermore, bend waveguides may cause polarization conversion in bends. Depending on curvature radius, the mode index in a bent waveguide can be different from that of a straight waveguide becasue of the large index contrast. This difference can cause an additional loss in transition from bend to straight waveguide [44].
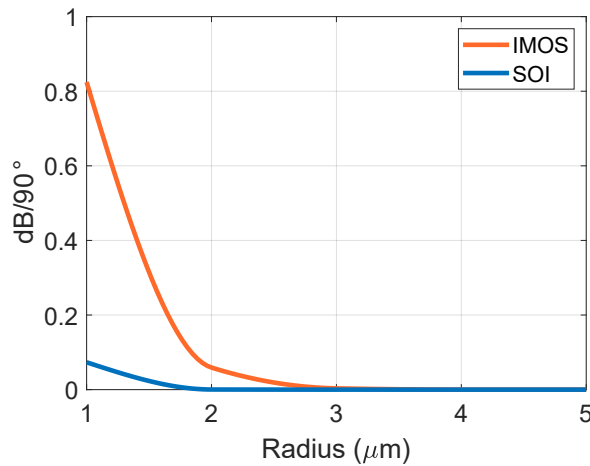
Figure 2.3: Loss per 90° bend waveguide with respect to curvature radius

Overall, according to the simulation results, both technologies can offer very compact resonators. However, the SOI, thanks to higher index contrast and wider geometry, shows slightly better performance in terms of bend loss. The simulation results presented so far are the main required parameters for the preliminary analysis of PICs. For ring resonators, the parameters n_g, and loss factor of the entire cavity are crucial since they are related to the Quality factor and Free Spectral Range [45].

2.1.1 Waveguide transmission

The measurement setup is sketched in Fig. 2.4. Light from a tunable laser source (TLS) feeds an optical component tester which measures the ratio of its output power and the power measured at the input. Measurement process is controlled by a software that

synchronizes wavelengths emission from the TLS and reading process of a photodiode. The output signal of the tester is used to excite the couplers (device under test, DUT) with the polarization adjusted by a polarization controller. The signal, guided by a standard cleaved SM fiber, is vertically coupled to the SM input waveguide of the DUT via the on-chip grating couplers. The transmitted signal is then retrieved by another SM fiber connected to the tester to obtain the transfer function. This signal is also monitored by the OSA using a 90:10 splitter. Thermal stabilization of the chip during the experiments was done using a thermoelectric cooler (set at 24 °C), driven by a temperature controller, placed under the aluminium chip holder.
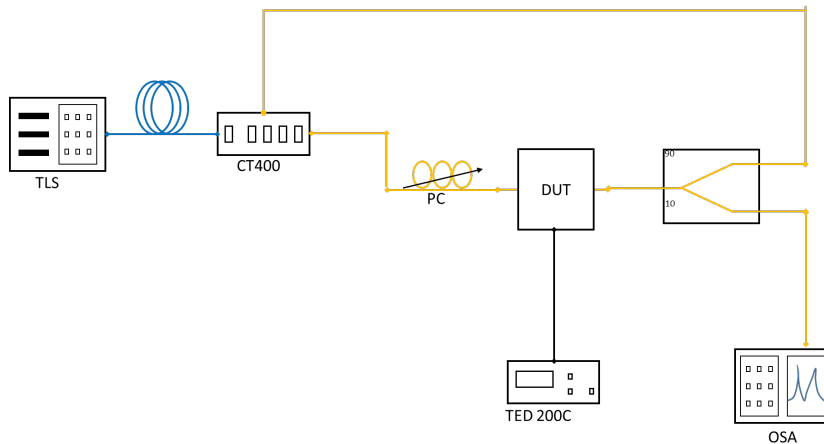
Figure 2.4: Experimental setup for transmission measurements. TLS: Tunable laser source (Yenista T100S-HP), CT400: Optical component Tester (Yenista CT400), TED 200C: -Thermoelectric temperature controller (Thorlabs), OSA: Optical spectrum analyzer (Yokogawa -AQ6370), DUT: Device under test and PC: Polarization controller.

Normalized transmissions of the SOI and IMOS waveguides are shown in Fig. 2.5 with an image example of a fabricated IMOS waveguide as an inset. The measured SOI waveguide has two 1200 μm long straight waveguides connected to a S-bend in the middle that has 10 μm curvature radius. The IMOS waveguide consists of two 185 μm long straight waveguides connected by the bend sections with 20 μm radius. Light couples from fiber to single mode waveguides through focusing grating couplers placed at the ends of the waveguides that excites the fundamental quasi-TE mode. Those couplers allow vertical coupling to the fibers, which are positioned over the chip at an angle (typically 10°) and are available as BBs in process design kits of the fabrication facility.

The insertion losses of SOI and IMOS waveguides are around 10 dB and 7 dB, respectively. Due to the lack of waveguides designed with different lengths, it was not possible to know, and then compare, their propagation losses in terms of dB/cm. If one can neglect the waveguide losses, then the coupling losses of SOI and IMOS grating couplers can be estimated as 5 dB and 3.5 dB per grating, respectively. It is generally assumed that waveguides in the two materials have both a maximum transmission wavelength at 1550 nm. The discrepancy between the two measured maxima (1542 nm
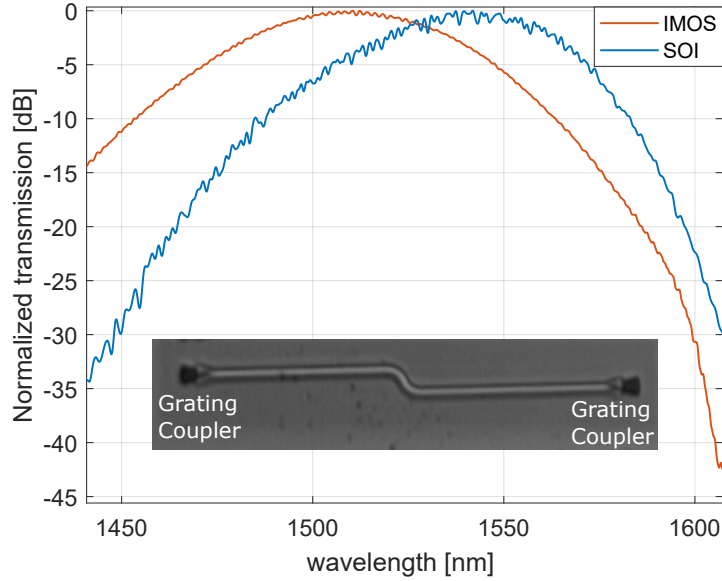
Figure 2.5: Normalized transmission measurements of single TE mode in SOI and IMOS waveguides and an example picture of a fabricated IMOS waveguide.

for SOI and 1510 nm for IMOS) can be ascribed to the grating performance. Besides possible fabrication variations, the inclination of the input and output fibers can also affect the maxima. We set the fibers inclined by 10° in both cases, however, gratings fabricated in different materials can require slightly different angles. We noticed, in fact, that the shift of the maxima in the spectra is around 10 nm from 8 to 11 degrees. Since grating couplers are wavelength dependent, this limits the significant measurements to a certain wavelength range. As seen in Fig. 2.5, each curve has a certain transmission bandwidth. The wavelength span used to measure the studied devices covers the C-band in the telecommunication window (roughly, 1530 - 1565 nm), except the IMOS directional couplers which are characterized at the fixed wavelength of 1550 nm. Note that the measured 3-dB bandwidths of both grating couplers (~ 50 nm) is sufficient to cover the C-band, if their maxima are at 1550 nm.

After having introduced the main characteristics of straight waveguides and before starting the discussion on ring resonators, it can be helpful to analyse Directional Couplers (DCs), which their optical features should be taken into account for designing ring resonators. Therefore, a part of the thesis is dedicated to study the IMOS DCs. Nevertheless, the ring resonators characterized in this thesis were mostly Silicon, the working attributes of DCs are applicable to both technologies.

2.2 Directional Couplers

Directional couplers are one of the fundamental building blocks of photonic integrated circuits. They allow electromagnetic power exchange between two or more closely spaced waveguides. Typical applications of DCs are power splitting or wavelength

filtering, as well as switching, if electrical controls are present. In fact, a micro ring resonator coupled to waveguides is basically composed of two 2×2 directional couplers and two straight waveguides, as previously shown in Fig. 1.3.

In this section, we experimentally study the performance of directional couplers. Analytic modelling of this component is generally done using the Coupled Mode Theory (CMT) [46–55], but this simple model has been originally proposed for low index contrast waveguides, which is not our case. In [56], it has been theoretically shown that the CMT can still be used for high index contrast devices if a careful choice on the coupling coefficient calculation is done. Here we experimentally validate that theoretical results comparing calculations with experimental results obtained with IMOS devices. Besides investigating the validity of the Coupled Mode Theory (CMT) applied to directional coupler structures with high index contrast, we can study the effect of some different topological choices in device fabrication. In particular, in addition to the conventional curved structures, we also consider ultra sharp corner bends that reduce the footprint. The effect of fabrication tolerances on the different guided mode polarizations is also discussed.

The task of determining the functional parameters of DC components is challenging. The use of a numerical approach would certainly lead to realistic answers, since any device can be precisely modelled even in 3D. However, this approach is not applicable in our design process since it requires specific modelling of the considered devices, while we want to limit our attention to the device functional behaviour. So, in practice, we look for an analytical model set up with characteristic parameters extracted from the results of many numerical simulations, fabrication runs and experimental measurements.

The studied Directional Coupler structures

In the following, we will consider directional couplers made by two parallel waveguides. In particular, two different types of DCs have been investigated. They are sketched in Fig. 2.6.
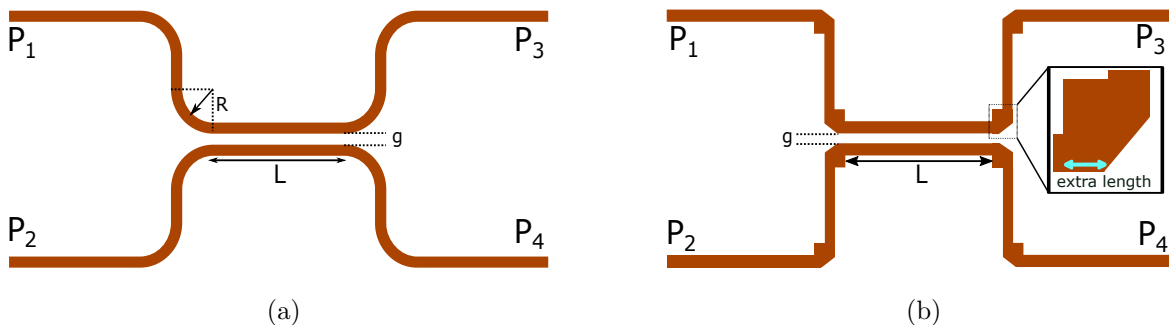
Figure 2.6: Sketches of the two studied symmetric coupler structures: (a) with bends; (b) with mirrors. The corner bend is placed as an inset for showing the extra length to the coupling section.

The former structure (shown in part (a) of the figure) has the classical shape, with two parallel waveguides close enough to couple the desired amount of power from one waveguide to the other, and input and output sections made by curved bends. Both curves of each arm have radius R. Inevitably, some coupling occurs also in these bends. This affects the overall coupler performance. Though such undesired coupling decreases when R decreases, it cannot be fully eliminated, since too small values of R cause unwanted high radiation losses. It is then better to include this effect in the design procedure. This can be done simply by increasing the real coupler length L by a further coupling length L_b that represents the effective extra length resulting from the bend coupling. Alternatively a sharp corner with low loss can be made by a mirror [57] instead of bend, as sketched in part (b) of the same figure. This provides the advantage of further reduction of the circuit foot print. However, as shown by the inset of the figure, representing a corner, the mirror shape has an extra waveguide section which is in proximity with another mirror in the coupling section. So, also in this case, an extra coupling length L_b should be considered.

In both designs, the ports labeled as P_1 and P_2 are the input ports, while P_3 and P_4 are the output ones. The straight sections of the coupler, with length L, are spaced by a gap g, which is defined from edge to edge of waveguide cores. Two sets of devices with curved bends have been fabricated with R equal to 10 or 15 μm. This allowed to investigate the strength of the coupling contribution imposed by the curves. Values of R have been chosen large enough to limit bending loss and polarization conversion. The values of the gap g and the length L of the parallel waveguide sections of both type of couplers are summarized in Table 2.2. For each value of g, ranging from 100 to 400 nm, some values of the coupler length L are considered. This will allow to determine, by fitting the experimental results, the value of the coupling length L_c, i.e. the distance necessary to ensure a complete power transfer from one guide to the other.

g (nm)	L (μm)
100	5, 10, 15, 20
200	10, 20, 30, 40
300	15, 30, 45, 60
400	35, 70, 105, 140

Table 2.2: Couplers design parameters.

2.2.1 Theoretical model of the directional couplers

The schematic of the central part of both type of couplers is shown in Fig. 2.7(a), while Fig. 2.7(b) shows the picture of one of the fabricated directional couplers. In this picture, the dark parts are the InP whereas the brighter parts correspond to 2 μm wide trenches of the BCB bonding layer. Two types of grating couplers are used to excite either a quasi-TE and a quasi-TM mode.
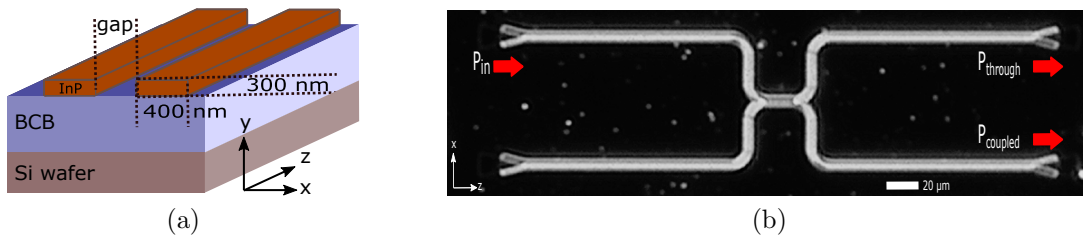
Figure 2.7: (a) Coupler structure schematic; (b) picture of a fabricated device.

The CMT model conventionally considers only the part of the device where the two waveguides are parallel and assumes that only one of the two input ports is excited by its guided mode. Using symbols introduced in Fig. 2.6 and normalizing powers so that $P_1(z = 0) = 1$ and $P_2(z = 0) = 0$, the two output powers are shown (see for example [46]) to be given by

$$P_3(z) = \cos^2(\kappa z) = P_t \tag{2.1}$$

$$P_4(z) = \sin^2(\kappa z) = P_c \tag{2.2}$$

where κ is the coupling strength and z is the longitudinal coordinate. P_t and P_c are also known as the *through* and *coupled* powers of the device. The distance at which coupling is complete is known as the coupling distance L_c. It depends on the coupling strength, described by the coupling coefficient κ. The relationship between L_c and κ can be found through the mismatch $\Delta\beta$, different for TE and TM polarizations, between the propagation constants of the two modes with even and odd symmetries of the full coupler, the so called device super-modes. It holds [58]:

$$L_c = \frac{\pi}{\Delta\beta} = \frac{\pi}{2\kappa}. \tag{2.3}$$

The CMT does not use super-modes, but computes the coupling coefficient using the modes of the single waveguides. Different expressions of κ have been proposed in these years, trying to adapt the original model to the new device features (higher index contrast, larger coupling, etc). In [56] some of the proposed CMT formulations have been checked to verify how successfully they can be used in the most demanding case of high index contrast and strong coupling, as it occurs in semiconductor waveguides. In particular, it has been shown that the coupling coefficient κ should consider not only the coupling between the transverse mode field distributions of the two single waveguides, but also between the no longer negligible longitudinal components. In other words, the coupling coefficient κ should be calculated as:

$$\kappa = \kappa^t + \kappa^z = \frac{\omega}{4} \int_{S_{\Delta\varepsilon}} \Delta\varepsilon \, \mathbf{E}_{t1} \cdot \mathbf{E}_{t2}^* \, dS + \frac{\omega}{4} \int_{S_{\Delta\varepsilon}} \Delta\varepsilon \, E_{z1} E_{z2}^* \, dS. \tag{2.4}$$

Superscripts t and z denote the transverse and longitudinal contributions due to the

corresponding components of the electric field $\mathbf{E}$ of the two single parallel guides (named 1 and 2) and $\Delta\varepsilon$ is the dielectric constant perturbation that one guide introduces to the other to create the coupler. Values of (2.3), which can be considered exact since they are obtained from super-modes, have been shown [56] to be in quite good agreement with those given by (2.4), while other expressions did not behave so well. The values of κ obtained from the super-modes and CMT have been calculated using a Finite Element Method (FEM) mode solver [41].

The experimental check of the CMT model results requires however some further comment. In fact, as mentioned before, the simple model of parallel waveguides cannot be used to describe real structures. For example, the effect of the extra (variable) coupling due to transition regions (bends or mirrors) should be included in the equations. To do so, (2.1) and (2.2) have been rewritten as

$$P_{through} = \cos^2[\kappa(L + L_b)] \tag{2.5}$$

$$P_{coupled} = \sin^2[\kappa(L + L_b)] \tag{2.6}$$

where, as before, normalized powers $P_1 = 1$ and $P_2 = 0$ have been considered and κ is always the coupling coefficient given by the CMT. L is the length of the straight parallel waveguides (values listed in Table 2.2) while the extra coupling due to bends or mirrors has been then described by a fictitious length L_b, to be determined, which is added to the length L [59].

Moreover, the input and output powers depend also on the efficiencies of the input/output grating couplers and might perform differently from device to device. In order to take into account also these effects, the measured output responses can be expressed as:

$$\left.\begin{aligned} P_{coupled_1} &= \sin^2[\kappa(L + L_b)] \cdot \alpha_1 \cdot \alpha_4 \\ P_{through_1} &= \cos^2[\kappa(L + L_b)] \cdot \alpha_1 \cdot \alpha_3 \end{aligned}\right\} \text{when } P_1 \text{ is considered as input} \tag{2.7}$$

and

$$\left.\begin{aligned} P_{coupled_2} &= \sin^2[\kappa(L + L_b)] \cdot \alpha_2 \cdot \alpha_3 \\ P_{through_2} &= \cos^2[\kappa(L + L_b)] \cdot \alpha_2 \cdot \alpha_4 \end{aligned}\right\} \text{when } P_2 \text{ is considered as input} \tag{2.8}$$

where α_i represents the overall attenuation induced by these effects in the i-th arm.

These four sets of measured data (two for each through and coupled ports) can be combined to eliminate the fiber-to-waveguide, bend and waveguide losses. One gets

$$\frac{P_t^2}{P_c^2} = \prod_{n=1}^{2} \frac{P_{through_n}}{P_{coupled_n}} = \frac{1 - P_c^2}{P_c^2} = R' \tag{2.9}$$

where P_c and P_t have been defined by (2.1) and (2.2).

One can then finally get the set of values

$$P_c = \frac{1}{1 + \sqrt{R'}} \qquad (2.10)$$

which will be fitted by (2.6) to find κ and L_b.

The couplers behavior will be studied only at the fixed wavelength $\lambda = 1550$ nm. The mode confinement and coupling strength depend in fact on the wavelength and we did not want to consider this further variable.

2.2.2 Experimental results and fitting procedure

In order to determine the coupler parameters and validate also experimentally the results obtained in [56], which suggest that Eq. (2.4) provides the best way to calculate the coupling coefficient κ to be used in the CMT, we have measured 96 devices (48 devices per polarization) fabricated with the design parameters reported in Table 2.2. The measurement setup is the same as sketched in Fig. 2.4. The incident polarization at the input port for the two modes is controlled by adjusting the polarization controller according to the maximum achievable transmission.

The values of the parameters κ and L_b were found by fitting the experimental results expressed by values given by (2.10) with those obtained by the theoretical model and given by (2.6). The fit process is critical for accurate interpretations of the experimental results. The fitting procedure to determine the values of κ and L_b was implemented by a MATLAB code [60]. Values of κ and L_b valid for each polarization have been determined applying a best fit procedure (nonlinear least squares method) to each set of measurement results corresponding to couplers with the same shape and gap g, but different lengths L to find the best fitting values of κ (or, according to 2.3, L_c) and L_b. The initial guesses of κ and L_b were found to be crucial, since the error function had many local minima, but not all of them could be associated to physically reasonable results. In particular, as the extra coupling imposed by the bends can not be larger than the coupling resulting from an equi-length structure of parallel waveguides, L_b must be positive but also lower than the coupling length L_c. Moreover κ must decrease for increasing gaps. Considering these conditions, the optimization was implemented by making iterations of different initial guesses of κ and L_b. The expected values of κ were chosen using CMT while the maximum of expected values of L_b were normalized to L_c. Then, 20 iterations for κ were done by using $0.1 \cdot \kappa \cdot m$ where $m = 1, 2, 3, ..., 20$. and 10 iterations for L_b by $0.2 \cdot L_b \cdot n$ where, $n = 1, 2, 3, ..., 10$. Lastly, the local minima of error function are inspected to check if it meets the conditions mentioned before. If not, this solution is discarded and a new minimum of the error function is checked, until all conditions are satisfied. As each iteration step for κ requires the whole set of iterations for L_b, so the total number of implemented iterations (200) was sufficient to

provide full coverage of all possible fitted values according to the previously mentioned procedure conditions which can be listed as:

- The value of root mean square error (rmse) of the fit function must be minimized.

- L_b obeys $0 < L_b < L_c$.

- κ must decrease as the gap increases.

Figures 2.8 and 2.9 show the results for the TE and the TM polarizations for different values of the gap g, respectively. The symbols refer to measured data, while the lines show the best fitting curves. The blue symbols or lines refer to devices with corner bends, while the red color characterizes results obtained for devices with curved bends with 10 μm curvature radius, and green refers to devices with curved bends with 15 μ m curvature radius. Part (a) of both figures refers to g = 100 nm, (b) refers to g = 200 nm, (c) refers to g = 300 nm and (d) refers to g = 400 nm. For a gap of 100 nm the effect of the extra coupling due to different transitions is evident. For larger gaps (and then longer devices) such effect tends to reduce. The overall standard deviation of rmse was found to be 4.6×10^{-3}, confirming the quality of the fit procedure.

An ideal DC coupler should have equally coupled powers independent from the input port. However, due to the measurement errors and possible imbalances in the upper and lower branches of the coupler (including total length and grating coupler performance), there can be some differences between the two measured coupled powers that can be defined as

$$\Delta P_c = \left| \frac{P_{coupled_1}}{P_{coupled_1} + P_{through_1}} - \frac{P_{coupled_2}}{P_{coupled_2} + P_{through_2}} \right|. \tag{2.11}$$

The error bars in Fig. 2.8 and Fig. 2.9 refer the mean value of a set of ΔP_c obtained from four measurements of each type of coupler (four different lengths for each gap). The small value of the standard deviation (7.6×10^{-3}) of overall ΔP_c reasonably shows the repeatability of the measurements.

The fitting procedure allows to determine κ and then, once L_c has been calculated using (2.3), also to separate the bend contribution, given by L_b, which can be expressed introducing the parameter k_b defined by

$$k_b = \frac{L_b}{L_c}. \tag{2.12}$$

Values of k_b for the different configurations (bend radii of 10 and 15 μm and corner sections) are shown in Fig. 2.10. As expected, the weakest contribution comes from the corner bends, while larger curvatures contribute more to the total coupling. The negative trend of k_b for increasing gaps confirms also that bend contributions weakens
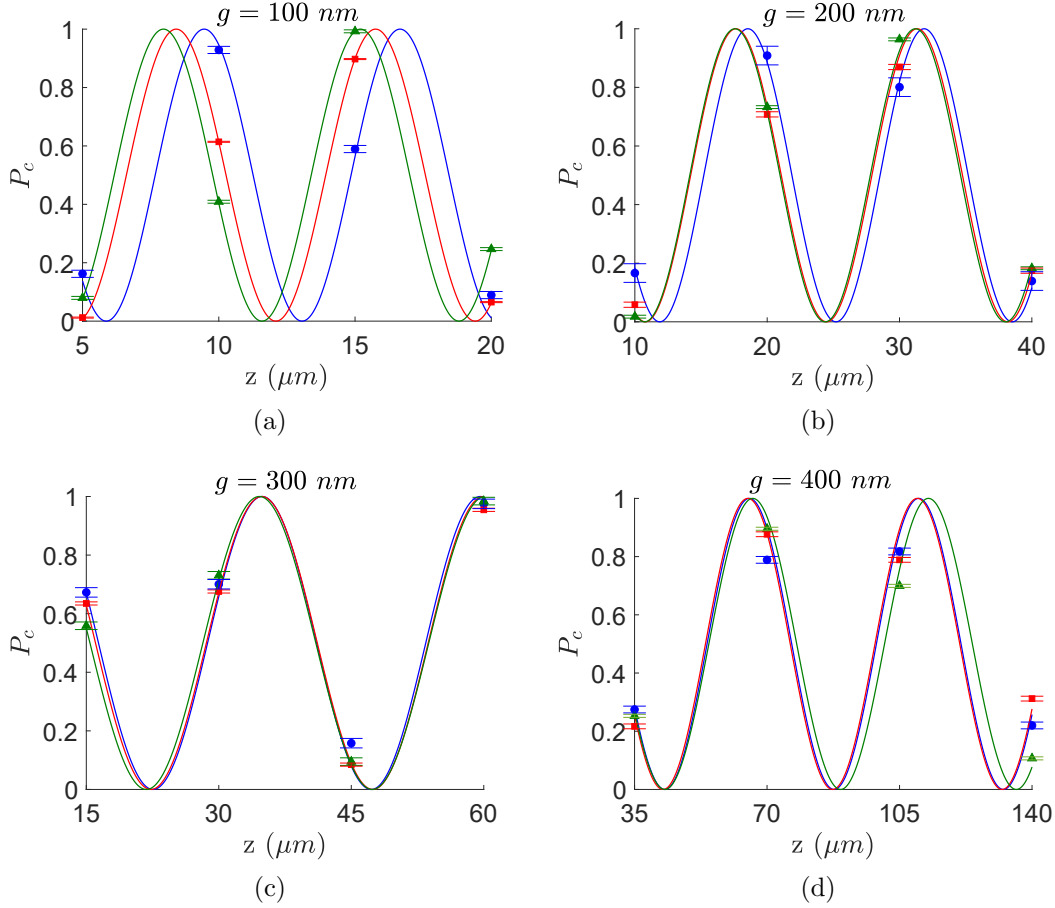
Figure 2.8: Fit curves of measured P_c for TE polarized excitation of couplers with gap of (a) 100 nm, (b) 200 nm, (c) 300 nm and (d) 400 nm. Symbols refer to measured data, lines to best fitting curves. Blue refer to corner bends, red to curved bends with 10 μm curvature radius, green to curved bends with 15 μm curvature radius.

for larger waveguide spacing. But even at larger gaps such as 400 nm, there is still some interaction between waveguides in both corner and curved bends. These results also confirm that coupling of the TM polarization is stronger than that of the TE one.

More interesting results needing careful comments come from the fitted values of the coupling coefficients κ. These values are shown in Fig. 2.11. Symbols show the values obtained by the fitting procedure of the different structures, the dashed line shows the result of the CMT theory and the solid line shows those derived from super-mode simulations. One can note first that the symbols are always superimposed, i.e. that values of κ do not depend on the type of structure (bends or mirrors), which proves the quality of the fitting process. One can also see that the agreement between the experimental and the theoretical values of κ is much better for the TM polarized modes (Fig. 2.11(b)). Rather surprisingly, on the contrary, the coupling coefficients of TE coupler are measured to be larger than the simulated ones (Fig. 2.11(a)). If we assume that both TE and TM couplers share the same fabrication tolerances, a possible reason of this mismatch can be related to some technological issues that can be more effective for TE polarized fields.
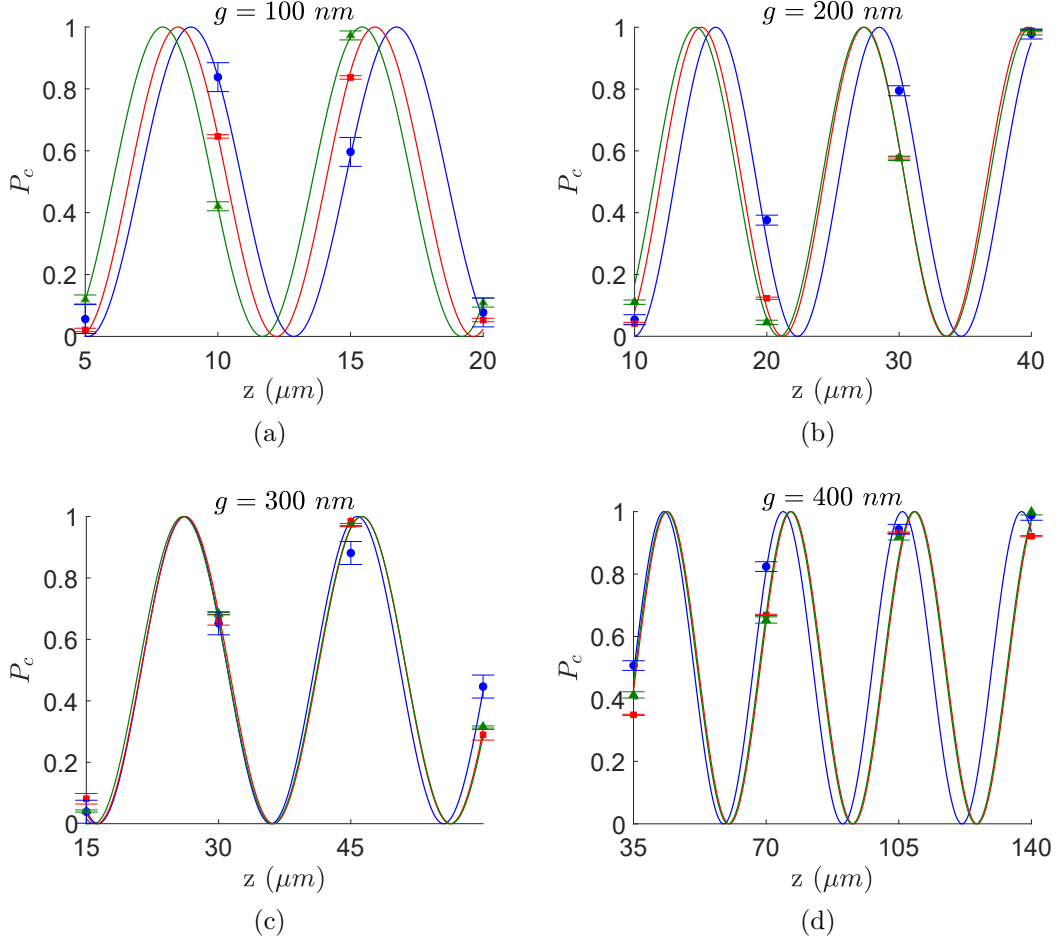
Figure 2.9: Fit curves of measured P_c for TM polarized excitation of couplers with gap of (a) 100 nm, (b) 200 nm, (c) 300 nm and (d) 400 nm. Symbols refer to measured data, lines to best fitting curves. Blue refer to corner bends, red to curved bends with 10 μm curvature radius, green to curved bends with 15 μm curvature radius.
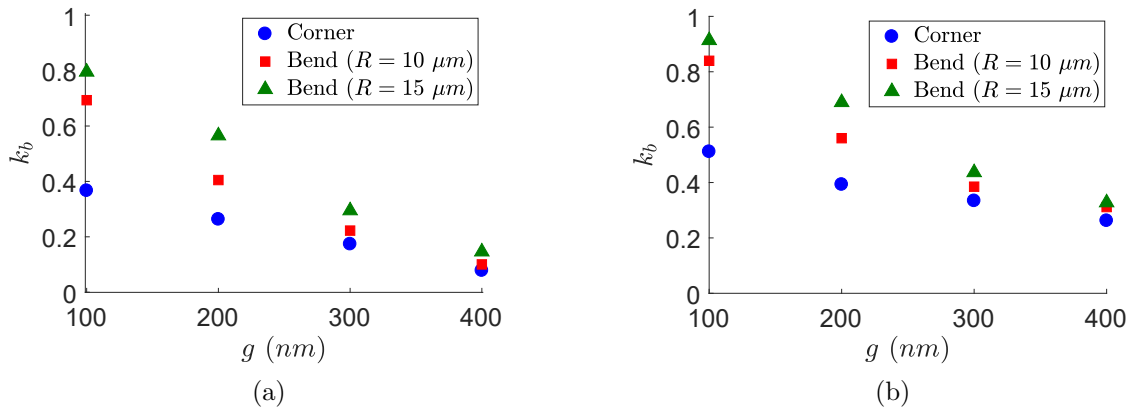
Figure 2.10: Relative contribution of bend coupling of TE (a) and TM (b) input polarization at $\lambda = 1550 \ nm$.

To figure out the difference in expected and obtained results of the two polarizations, one can notice that the height of the waveguides is fixed with a good precision, since it depends on the layer thickness, which is assumed to be precisely controlled. Their
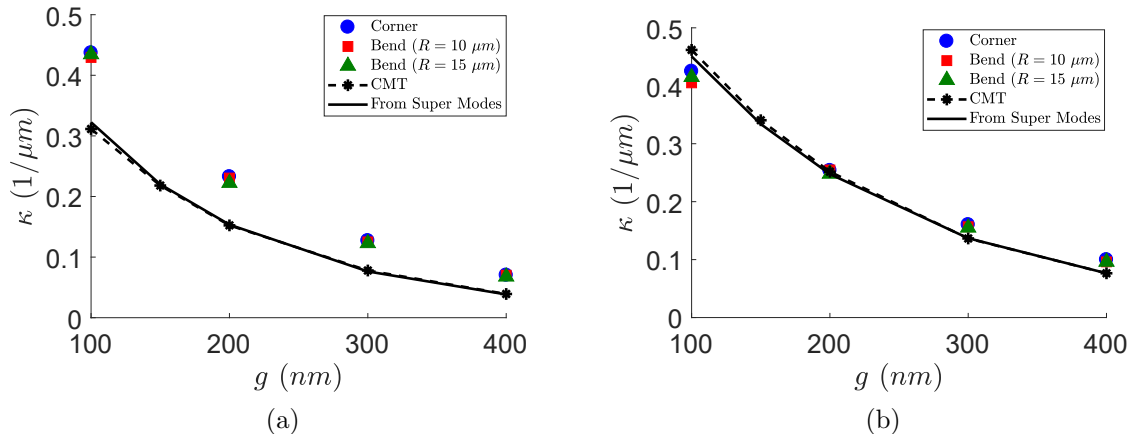
Figure 2.11: Experimental results in comparison to FEM simulations of super-modes and Coupled Mode Theory for (a) TE and (b) TM coupling coefficient at $\lambda = 1550\ nm$.

width, however, critically depends on the tolerances of the lithography process, which affect the lateral dimension, therefore, the gap. The different vertical and horizontal fabrication tolerances have an impact on both the mode shapes and on coupling. As the electric field is mostly horizontally polarized for TE modes and mostly vertically polarized for TM modes, the effect of fabrication errors in waveguide width should then impact more on TE than on TM modes.

A further technological issue to be considered comes from the etching process. Etching may for example induce some roughness in the waveguide sidewalls. This generates some scattering which affects coupling. But a larger effect is expected to come from the etching depth which can be due to the lag effect. Smaller gaps, in fact, reasonably make complete etching down to the required depth more difficult. For example, considering the topology with closest waveguide, the slot between the waveguides should be 300 nm deep and 100 nm wide.

To investigate the effect of all these possibilities (excluding scattering due to lateral surface roughness), we have then simulated different situations. We have changed the widths of the waveguides, the gap size, and added a floor in the slot, simulating a not perfect etching process. Parameter were changed one at a time, to check their relative effect on the final results. Values were chosen realistically, considering the used technology. The waveguide width tolerance was assumed to be $\Delta w = \pm\ 20$ nm, while the footing layer was supposed to be up to 100 nm (irrespective of the gap, which is clearly a highly pessimistic hypothesis).

Fig. 2.12 shows the impact of width and etch depth (or footing layer) variations and results of post FEM simulations. The light blue areas represent the interval of the coupling coefficient for the worst cases of the gap and width combinations, related the E-beam lithography effects alone. Changes of the expected values of the coupling coefficients are small, but anyway explain rather well the discrepancies between the TM theoretical and experimental results. The (dark) grey areas refer on the contrary to the

effect of the footing layer. This issue clearly affects mostly TE theoretical results. The decreasing difference between measured and expected values of the coupling coefficients confirms that the footing layer decreases for increasing gaps. The assumption of 100 nm thick footing layer was then pessimistic, but can be a starting point for a more detailed analysis.
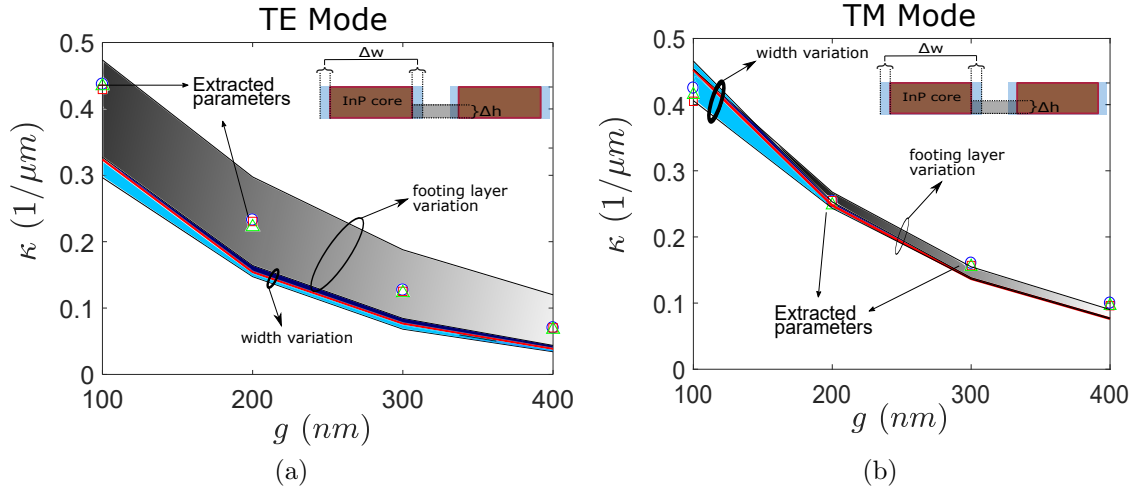
Figure 2.12: The effect of fabrication variation on (a) TE and (b) TM mode coupling coefficient in terms of width ($\Delta w = \pm 20$ nm), light blue domain and etch depth ($\Delta h = 100$ nm), grey domain. Red line represents the ideal case and dark blue parts are the cross section of width and etch depth variations. The cross section of coupler is placed as an inset.

As one can see, the introduction of the incomplete etch depth can reasonably explain the difference between measured and simulated coefficients for the TE polarized modes, suggesting that this is the most critical technological issue. Similarly, as previously reported in [61], TE coupling coefficients of shallow etched waveguides in SOI technology were mostly influenced by slab thickness variations while the effect of width variations were found to be weak. Correspondingly, we found similar results for deep etched waveguides, considering the footing layer a slab in coupling sections. However, we additionally demonstrated that the effect of width variations, albeit limited, becomes dominant when a strong TM polarized coupling is present (see the blue domain between 100 and 200 nm of g in Fig. 2.12(b)).

These results also allow to conclude that devices based on the TM polarized modes have the advantage of being more tolerant to fabrication issues as their performance depends more on the membrane thickness, if it is precisely controlled. However, since the TE modes are more confined in the guide, bends with smaller radius for TE mode are allowed and provide lower bend losses. Based on the provided PDKs of the INPHOTEC fab, the SOI ring resonators presented in this thesis were designed, by considering only for the TE polarization.

2.3 Conclusions

In this chapter we first introduced the SOI and IMOS waveguide layer stacks and related technology parameters such as effective indices of TE mode and group index. A theoretical comparison of bend losses with respect to curvature radius was provided. Transmission measurements of straight waveguides of both types of waveguides were presented. 3-dB bandwidths of the grating couplers in both technologies were greater than 50 nm, with the maxima at different wavelengths of 1510 and 1542 for IMOS and SOI, respectively.

Next, we have presented a theoretical and experimental analysis of directional couplers with both curved and corner bend connectors, fabricated by the IMOS technology aiming both at experimentally assessing the CMT and defining design criteria to set up design kits for this recent and promising technology. Key design parameters have been presented.

It has been first confirmed that corner sections have reduced coupling contributions and footprint compared to curved couplers. However, even if the waveguides are far from each other, there is always a non negligible coupling imposed by the corner sections.

We have then compared the TE and TM mode results in terms of coupling coefficient obtained by fitting the coupling ratio measurements. Neglecting the side-wall roughness effects, TM mode couplers anyway exhibited a good agreement between theoretical and experimental results, confirming the successful possibility of using the CMT theory also for high index contrast waveguides.

Larger discrepancies between theoretical and experimental results for the TE case have also suggested that a critical issue in device fabrication comes from the etching process, which does not allow complete etching for narrow trenches.

Finally, TM coupling coefficients were found to be more tolerant to fabrication variations than TE ones under the same deviations of waveguide width and etch depth in the coupling section. On the other side, the circuits that require small radius can benefit from highly confined TE polarization.

Chapter 3

Design and modelling of micro ring resonators

This chapter presents Transfer Matrix Method (TMM) based analytical models of MRR structures. Modelling and static transmission characterization results of single micro ring resonators are first provided. Then, an analytical model of directly coupled ring resonators (Eye-like) is developed. Finally, the critical design aspects and working regimes of indirectly coupled resonators are introduced. The theoretical transfer functions of devices based on this configuration are obtained and discussed. The transfer functions developed in this chapter will be used in the next chapters when comparisons of the experimental results are discussed.

3.1   Modelling of single micro ring resonator

Single MRRs coupled to waveguides in different configurations have been introduced in Chapter 1. In this section we develop a TMM based modelling, considering the so called cross-grid configuration [62], to study its transmission characteristics. An example of wavelength routing of a MRR in the cross-grid configuration is illustrated in Fig. 3.1, using FDTD simulations [63]. At the resonance wavelength of the ring, near $\lambda = 1540$ nm, the incoming light is routed toward the drop port (*left*). This process is called channel dropping in Wavelength Division Multiplexing (WDM) communication systems. Instead, in the off resonance case, the light is transferred to the through port (*right*). The resonance condition induced by the geometry of the device and propagation mode satisfies:

$$m\lambda_{res} = n_{eff}L \tag{3.1}$$

where m is an integer number ($m = 1, 2, 3, ...$), λ_{res} is the resonant wavelength and $n_{eff}L$ is the optical path of the ring, being n_{eff} the effective index of the propagating mode and $L = 2\pi R$ the ring geometric length.

In order to attain the best dropping performance, the coupling between the bus
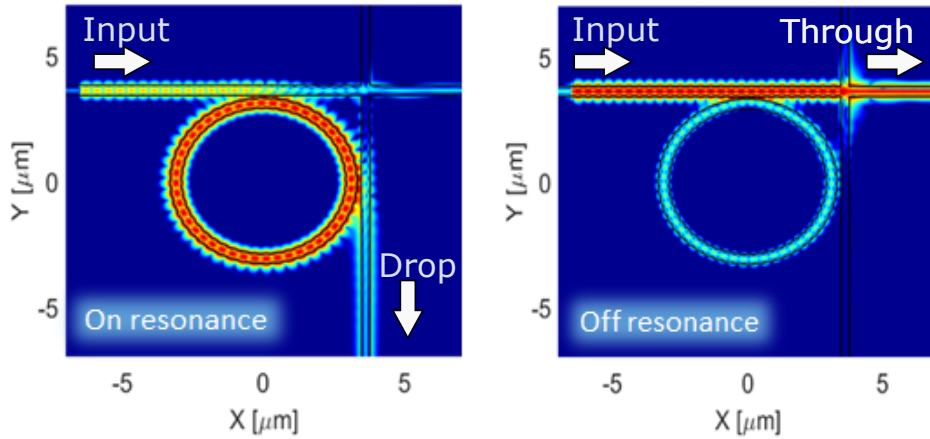
Figure 3.1: An example of wavelength routing process of MRR in cross-grid configuration. The electric field intensity on resonance at 1540 nm (left) and off resonance at 1500 nm (right).

waveguides and cavity should be optimized. Placing the cavity too close to the bus waveguides can cause an over coupling condition which can degrade the channel rejection and introduce more insertion loss to the through port. On the other hand, very weak coupling, called also under coupling, can cause insufficient channel dropping. The optimum feasible performance depends on the relationship between the coupling and the cavity losses. Anyway, the best performing wavelength routing devices require the critical coupling condition, which will be discussed in detail later in this chapter. Simulating realistic resonators (the minimum value of radius among the fabricated rings was 12 μm) requires quite big computational resources. Therefore, analysing such devices via analytical models gives a flexible and fast design approach. This is ture, in particular, if one is interested in having an idea of the geometrical parameters in order to implement a network, where many rings are involved. For this reason, an approach based on BBs and PDKs should be preferred when a device involving more than a single ring is investigated.

Analytical model of single MRR

The schematic of a MRR in cross-grid configuration is depicted in Fig. 3.2. A ring cavity with radius R is vertically and horizontally coupled to straight waveguides by the directional couplers labelled as (DC_1) and (DC_2), respectively. The input (E_{in}), drop (E_d), through (E_{th}) and add (E_{add}) are the normalized complex mode amplitudes such that their squared magnitudes are proportional to the modal power. The inset of the figure represents the coupling matrix where k and t are the cross and through coupling coefficients and * denotes the conjugated complex value. In case of lossless coupling, $|k|^2 + |t^2| = 1$ holds. In the previous section, it has been shown that the DC coupling powers can be presented as a cosine or sine function coupled by the field

coupling coefficients. Here, for simplicity, we denote t and k as the square root of (2.5) and (2.6).
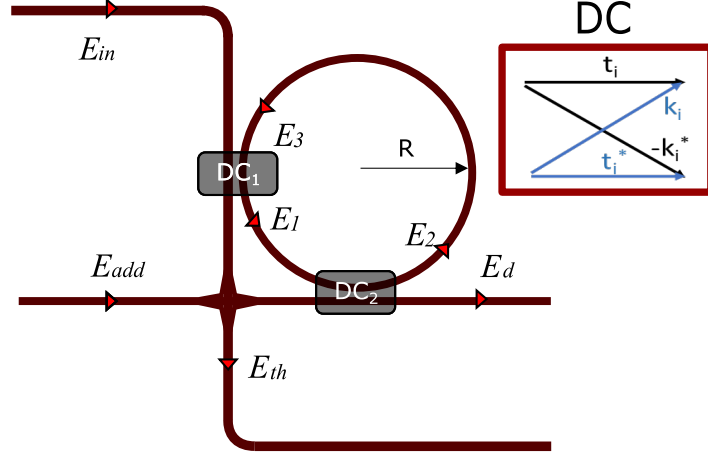
Figure 3.2: Schematic of the micro ring resonator in cross-grid configuration.

The fields at the output ports can be related to the input fields at the in and add ports as follows [64]:

$$E_{th} = t_1 E_{in} + k_1 E_3 \tag{3.2}$$

$$E_d = t_2 E_{add} + k_2 E_1 \alpha^{1/4} e^{i\theta/4} \tag{3.3}$$

$$E_1 = t_1^* E_3 - k_1^* E_{in} \tag{3.4}$$

$$E_2 = t_2^* E_1 \alpha^{1/4} e^{i\theta/4} - k_2^* E_{add} \tag{3.5}$$

$$E_3 = E_2 \alpha^{3/4} e^{i3\theta/4} \tag{3.6}$$

where α is the round-trip loss coefficient of the ring and is the ratio of coupled field intensity into the ring and the feedback field (round-trip travelled) intensity. This coefficient includes all possible loss sources in the cavity, e.g. radiation and scattering losses. The crossing and waveguides, on the contrary, have been considered lossless. The phase shift θ is defined as $\theta = \beta * L$ where the propagation constant $\beta = 2\pi n_{eff}/\lambda$ and L is the circumference of the cavity. For simplicity, we can remove $E_{add} = 0$ from the calculation and assume that $E_{in} = 1$.

Solving the equation system one gets the final expressions of E_d and E_{th} as

$$E_{th} = \frac{t_1 - t_2^* \alpha e^{i\theta}}{1 - t_1^* t_2 \alpha e^{i\theta}} \tag{3.7}$$

$$E_d = \frac{-k_1^* k_2 \alpha^{1/4} \theta^{1/4}}{1 - t_1^* t_2 \alpha e^{i\theta}} \tag{3.8}$$

and the corresponding power expressions for the through port

$$P_{th} = |E_{th}|^2 = \frac{|t_1|^2 - 2t_1 t_2 \alpha e^{i\theta} + |t_2|^2 \alpha^2 e^{i2\theta}}{1 - 2t_1 t_2 \alpha e^{i\theta} + |t_1|^2 |t_2|^2 \alpha^2 e^{i2\theta}} \qquad (3.9)$$

and drop port function

$$P_{dr} = |E_d|^2 = \frac{|k_1|^2 |k_2|^2 \alpha^{1/2} e^{i\theta/2}}{1 - 2t_1 t_2 \alpha e^{i\theta} + |t_1|^2 |t_2|^2 \alpha^2 e^{i2\theta}}. \qquad (3.10)$$

When the ring is on resonance ($\theta = 2\pi$m, m is integer number), P_{th} reduces to

$$P_{th} = \frac{|t_1 - t_2 \alpha|^2}{1 - 2t_1 t_2 \alpha + t_1^2 t_2^2 \alpha^2}. \qquad (3.11)$$

The critical coupling is then required to achieve the highest extinction ratio (ER: the difference between maximum and minimum transmitted powers expressed in dB) of the through port (E_{th}) transmission [65]. As a consequence, the dropped wavelength power maximizes. In other words, the transmitted power to the through port can be theoretically zero when the following relationship between coupling and loss of the ring holds:

$$\alpha = \left| \frac{t_1}{t_2} \right|. \qquad (3.12)$$

The critical coupling condition in lossless case ($\alpha = 1$) can be only achieved with identical couplers. For real applications, possible sources of loss factor, e.g., bend or surface roughness induced scattering, should be taken into account. This adds another difficulty to design high performance resonators. However, a careful estimation of the possible losses for a given radius can help to optimize the transmissions by redesigning the gaps of the waveguide to ring coupler, i.e. by tailoring the coupling coefficients of the couplers. In this way, the critical condition can be still achieved.

Transmission profiles and resonator parameters

As an example, Fig. 3.3 shows the through (P_{th}) and drop port (P_{dr}) transmissions obtained by the presented model calculated with, $k_1 = k_2 = 0.3$, $\alpha = 0.99$, R= 20 μm. Power of the resonant peaks maximizes periodically (FSR = 4.64 nm) at certain wavelengths (defined by (3.1)) where the through port exhibits transmission dips with an extinction ratio of about 20 dB. Except FSR, which depends on ring radius and mode effective index, all the other resonator metrics relate to the coupling coefficient. Considering a given loss factor, it is possible to adjust k according to the critical coupling condition (3.12).

The functional characteristics of a ring resonator can be described by some figures of merit (FOM) such as the frequency separation of consecutive resonance peaks, representing the Free Spectral Range (FSR), the Q-factor corresponding to a measure of
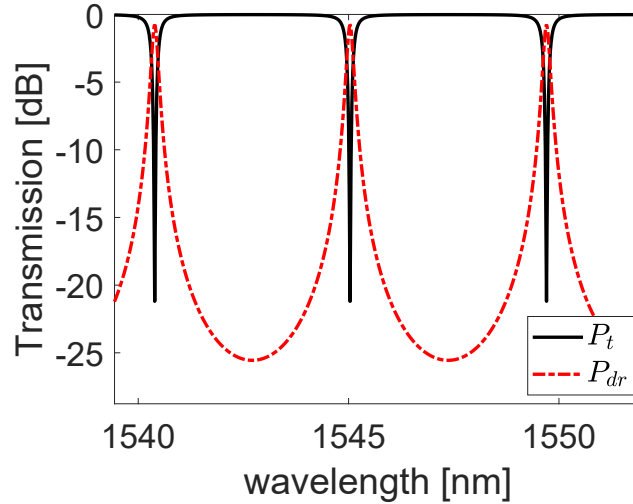
Figure 3.3: Transmission of the through (solid) and drop (dash) ports ($k_1 = k_2 = 0.3$, $\alpha = 0.99$, R = 20 μm).

sharpness of the resonances and the 3-dB bandwidth, also called Full width Half Maximum (FWHM). Assuming weak coupling ($k \ll 1$) and $\lambda \gg$ FWHM) [66], expressions of FOM of MRRs and the related formulas can be summarized in Table 3.1. As stated earlier, the main topological design parameters are the length of the cavity and gap (as it is responsible of coupling coefficient k).

The analysis of MRRs in this chapter is made by considering silicon devices and therefore, their simulated technology parameters reported in Table 2.1.

Just as an example of how the design process can be implemented, one can start investigating the effects of coupling strength on bandwidth and sharpness. Figure 3.4 shows the through and drop port signals behaviour for different coupling coefficients, varying from 0.1 to 0.7. Parameters of the radius and loss coefficient are the same as before. As shown in Fig. 3.4(a), the sharpness of the transmission dip near resonance increases by decreasing the coupling coefficient. However, strong coupling also introduces insertion loss after a certain value, such as, at $k = 0.70$. It can also be seen in Fig. 3.4(b) that the drop port exhibits smooth transmission in the wavelength span and does not efficiently perform wavelength selectivity. On the other hand, if the coupling is weak ($k = 0.10$), the ER of the through port dips reduces by a factor of four compared to the case when $k = 0.30$ and the dropped wavelength experiences higher insertion loss, which is 6 dB in this example. As a result, there is a trade-off between sharpness, which concerns of Q-factor and insertion loss of resonant peaks.

In order to choose a proper waveguide spacing of coupler for the design of the desired resonator, one should consider also the minimum value of radius realizable without increasing too much bend losses. The Film Mode Matching (FMM) method based [43] simulation results of the bend-to-straight waveguide couplings according to the radius of the curvature and gap are shown in Fig. 3.5. As the curvature radius increases, the coupling strength enhances. However, the gap must be taken into account

FOM	Description
$FSR = \Delta\lambda = \dfrac{\lambda^2}{n_g L}$	Free spectral range
$FWHM = \dfrac{\lambda^2 k^2}{\pi n_{eff} L}$	Full width half maximum
$F = \dfrac{FSR}{FWHM}$	Finesse
$Q = \dfrac{\lambda}{FWHM} = \dfrac{n_{eff} L}{\lambda} F$	Quality factor

Table 3.1: Figure of merit of optical micro ring resonators (assuming weak coupling ($k \ll 1$) and $\lambda \gg$ FWHM).
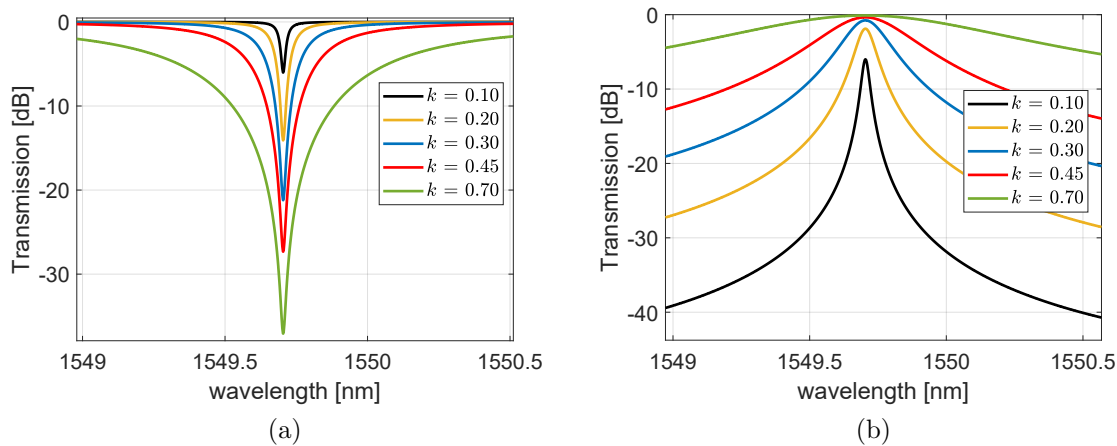
Figure 3.4: Transmission profiles of the through (a) and drop ports as a function coupling coefficients.

to prevent over coupling as well as possible low Q- factors. Therefore we have decided to fix the gap at 150 nm and radii between 12 and 25 μm for fabrication, including the indirectly coupled resonators. Decision of gap is made considering the coupling effects on the transmission profiles. Power reduction of the dropped peak can be kept below 3 dB, with k between 0.2 and 0.3. So, 150 nm of gap ensures, according to the simulations, all bend couplings, from a radius ranging from 12 to 25 μm.

3.1.1 Transmission measurements of single Silicon MRRs

The measured transfer functions of a ring with the cavity of R = 20 μm is shown in Fig. 3.6. The FSR of the measured resonator is 4.67 nm. Due to the SOI grating
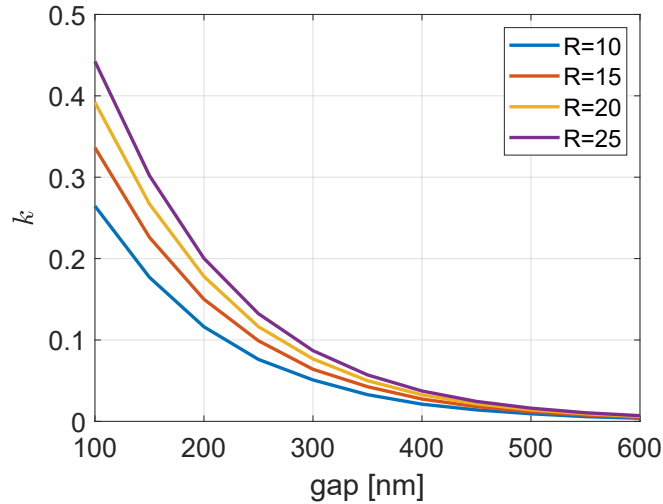
Figure 3.5: Bend to straight waveguide coupling at $\lambda = 1550$ nm of different radii of curvatures as a function of gap.

coupler response, the spectrum centred at about 1550 nm shown in Fig. 2.5 presents the central region of the spectrum. The ER of transmission dips is about 9 dB, while the dropped peaks have about 25 dB of ER (also called as WDM channel rejection). The Q-factor of the resonance peak near 1554 nm, shown in Fig. 3.6(b), is ~16,500 (corresponding 0.095 nm of FWHM). By using the equation of FWHM reported in Table 3.1, we found the coupling coefficient to be $k = 0.19$ (the simulated one was 0.26) at 1550 nm.
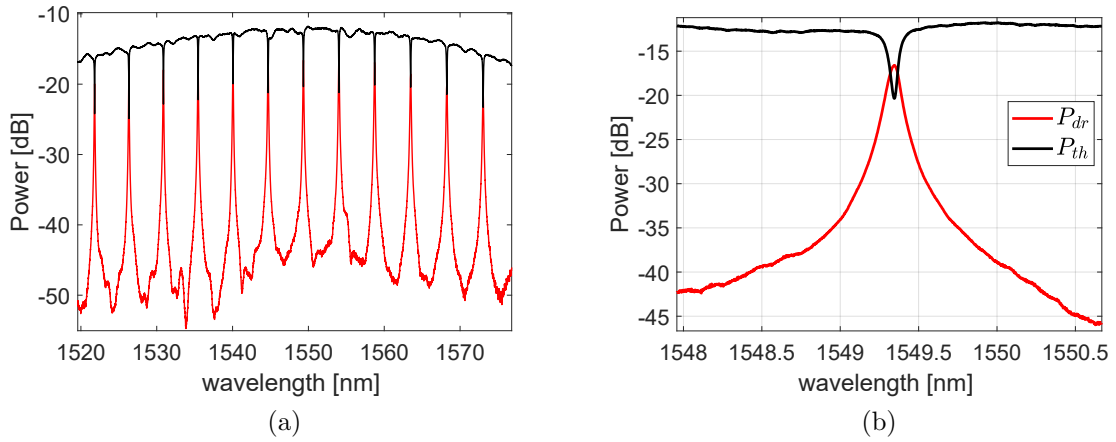
Figure 3.6: Measured transmissions of through (black) and drop (red) ports of a ring (R= 20 μm) (a), and a zoom view near λ =1549 nm.

Measurements of the fabricated SOI resonators with different radii are now reported. The results are shown in Fig. 3.7. The model outcomes, with the inserted parameters reported in Table 2.1, are in good agreement with the obtained results. The smallest radius (R = 12 μm) results in the largest FSR (around 8 nm), while the ring with the radius of 25 μm has a FSR below 4 nm. The corresponding measured Q factors range from ~9500 up to ~20000. Figure 3.7(b) shows the values of the Q factor vs.

radius. As we mentioned in the previous chapter, directional couplers are wavelength dependent and therefore each resonance wavelength is associated to a different value of k. This can affect the FWHM and may cause variation in Q values in the measured wavelength span. The bars in the Figure refer to the lowest and the highest values measured in the C-band. The mean values of the measured Q factors remain between 16×10^3 and 18×10^3, except a lower Q when R = 12 μm. The difference comes from the fact that bend to waveguide coupling depends also on the radius, as effective coupling length increases as radius gets bigger. This results in different coupling coefficients and, in most cases, the larger R, the larger coupling power. Furthermore, attenuation in different lengths is also variable, even though the bend induced losses are neglected. However, scattering losses in bends appear to be dominant when the radius is 12 μm.

(a)

(b)
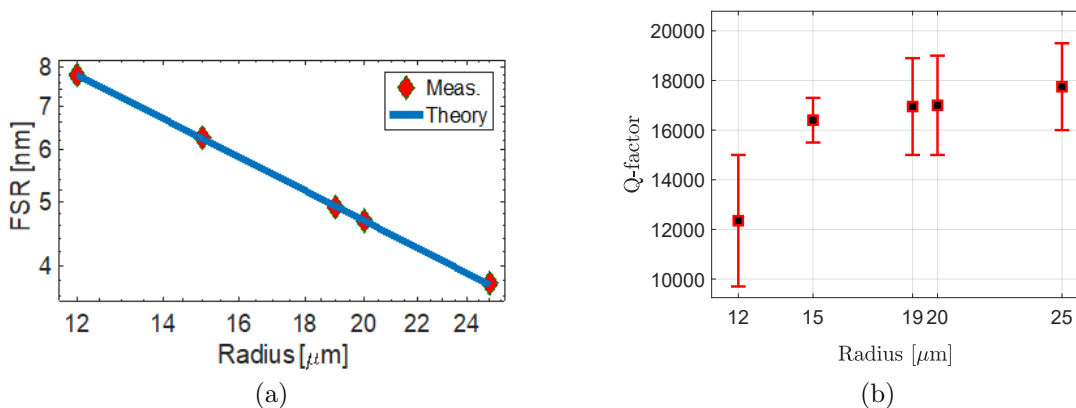
Figure 3.7: Measured Free Spectral Range (a) and Q-factor (b) vs. radius.

So far, we have presented the transmission results when the temperature of the devices remains constant during the measurements. In the next subsection, we investigate resonant wavelength manipulation based on thermo-optic effects.

Thermal tuning

Resonance wavelengths of a fabricated ring can differ from the expected ones, since ring resonators are sensitive to fabrication variations and thermal conditions. In order to ease calibration, the device should be tunable. This can be done by inducing a temperature variation in the device cavity. Increasing temperature will result in a red-shift of resonance wavelengths. Two different methods, known as off-chip and on-chip, can be considered to configure the device to operate at the desired wavelengths. In off-chip method, a thermoelectric cooler (TEC) cell can provide a temperature control of the whole chip via a surface which is attached to the bottom of the metallic chip holder. Since the resonators are sensitive to room temperature, this device is used to stabilize the chip temperature during the measurements. On the other hand, integrated heaters allow more precise wavelength shift control of each single ring by applying a voltage to heaters via electrodes. Figure 3.8 shows an example of how device tuning is oper-

ated. Figure 3.8(a) is a view of the aluminium holder with input and output coupling with fibers and electrodes. Figure 3.8(b) shows the microscope image highlighting the coupling sections for fibers and electrodes on the metallic pads. While the electrical connections are made of Gold, the resistor placed on a 1 μm thick SiO_2 cladding, shown in Fig. 3.8(c), is of Titanium. The width of the heaters is fixed as 3 μm, their lengths depend on the ring radius that have resistance in order of a few tens of Ω.
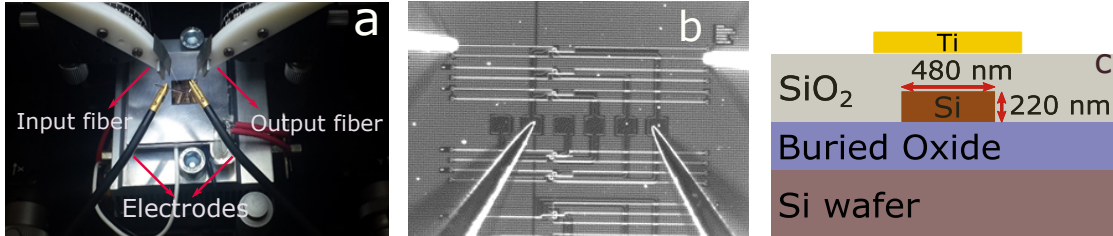
Figure 3.8: Implementing thermal tuning: an image of a part of the measurement setup (a). The temperature of the chip is controlled by a thermoelectric cooler (TEC) cell placed under the aluminium chip holder. The electrodes connected (bottom) to the metal pads to drive the integrated heaters and the fibers aligned (upper) on the grating couplers (b). The cross section schematic of the waveguide with a metallization layer of Titanium (c).

Thermally tuned resonances of off-chip and on-chip approaches are shown in Fig. 3.9. The first results are obtained by setting TEC at different temperatures by an offset of 4 °C. In this way, the whole chip either heats up or cools down. This causes all the device refractive indices change according to the temperature variation ΔT. When the temperature increases, the wavelengths experience a red-shift in the spectrum due to the increased effective refractive index of the resonance modes. Resonance wavelength shifts in the through port spectrum are shown in Fig. 3.9(a). The measured thermal tuning coefficient is about 95 pm/°C.
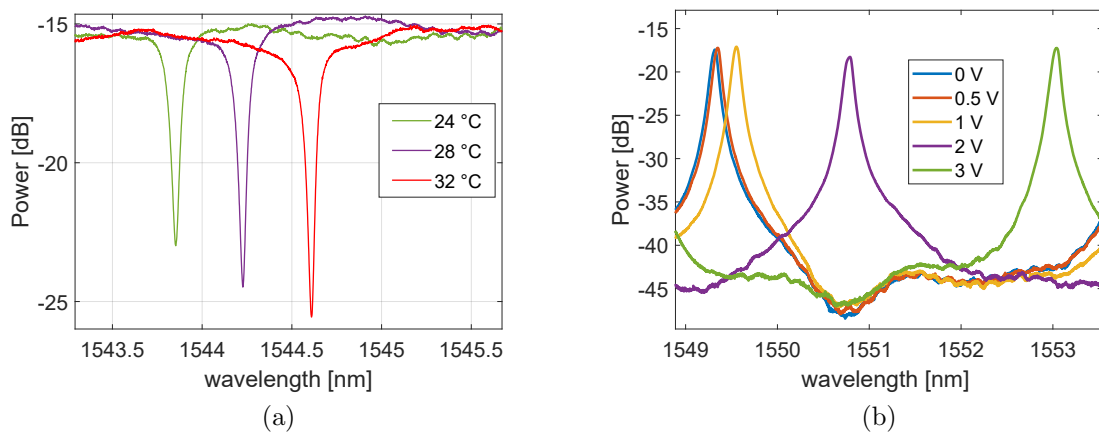
Figure 3.9: Resonance wavelength shifts according to temperature variation controlled by TEC (a) and to the applied voltage on the integrated heaters (b).

The use of TEC can tune only roughly the device temperature. To have more precise and stable control on wavelength tuning and in particular to tune a single ring,

electrically driven integrated heaters can be used to heat up locally the parts of the device where the heaters are placed. Resonance shifts induced by an applied voltage are shown in Fig. 3.9(b). These measurements are obtained from the same device whose transmission spectra are shown in Fig. 3.6. A linear fit of the amount of the measured wavelength shifts $\delta\lambda$ compared to applied power is shown in Fig. 3.10. The tuning efficiency obtained from the slope of fit is 110 pm/mW. This value can slightly differ from device to device, because the length of the resistor is proportional to the radius of the resonator. In the presented example, the radius was 20 μm.
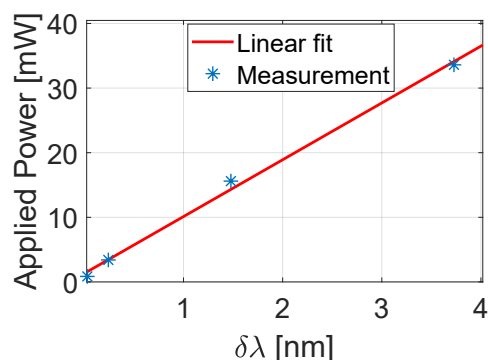
Figure 3.10: Resonance wavelength shift compared to applied power.

Table 3.2 summarizes the characterization results of single MRRs fabricated with the SOI technology.

R [μm]	Q factor	FWHM [nm]	FSR [nm]	$\dfrac{\Delta\lambda}{\Delta T}$	$\dfrac{\Delta\lambda}{\Delta P}$	$\dfrac{\Delta T}{\Delta P}$
[12 - 25]	[9700 - 19500]	[0.08 - 0.16]	[3.75 - 7.85]	95 $\dfrac{\text{pm}}{°\text{C}}$	110 $\dfrac{\text{pm}}{\text{mW}}$	1.15 $\dfrac{°\text{C}}{\text{mW}}$

Table 3.2: Characterisation results of single MRRs fabricated in SOI.

In dense WDM (DWDM) network applications, the FSR of a ring is recommended to be greater than the spectral extent of the C-band to by-pass other wavelengths in off state. However, large FSRs can be obtained only with small radii, but at a cost of increasing the bending loss. The maximum FSR reported for silicon MRRs is 93 nm with bending loss 0.009 dB/90° [67]. Moreover, FWHM and Q-factor are inversely proportional, and the responsible design and technology parameters for achieving high Q-factor are the coupling and loss coefficients [66].

In this section, we have investigated first order MRR in cross-grid configuration. By using the developed analytical model, the critical design parameters, k, and R are investigated for silicon rings. Next, we will introduce directly and indirectly coupled resonators.

3.2 Directly coupled micro ring resonators

Bandwidth variable channel dropping filters are the key components, providing variable bandwidth characteristics to wavelength selective switches, in flexible optical networking. Dynamic reconfiguration of network sources can benefit from multiple sub-carriers that can be aggregated to introduce so called Super channel. Super channels increase spectral efficiency, providing adaptive bandwidth assignments in flexible grids [68]. In this section, we develop an analytical model for a second order coupled MRRs in add/drop configuration. Particularly, the type called Eye-like ring resonators where an embedded (or loaded) second ring is coupled to another ring. We first review electromagnetically induced transparency (EIT)-like effects. Later, we extend our analysis to investigate possible applications of embedded rings in terms of bandwidth variable add/drop filtering applications in the context of Super channels.

Modelling of second order embedded ring resonators

Horizontally embedded ring resonators are shown in Fig.3.11. The device consists of four couplers as shown in the schematic. The transfer function of the device can be derived using coupled mode theory [69]. The t_i and k_i (i= 1, 2, 3, 4) represent the coupling coefficients of the i-th coupler. E_{in}, E_{th}, E_d and E_{add} are the normalized complex mode amplitudes at the input, through, drop and add ports, respectively.
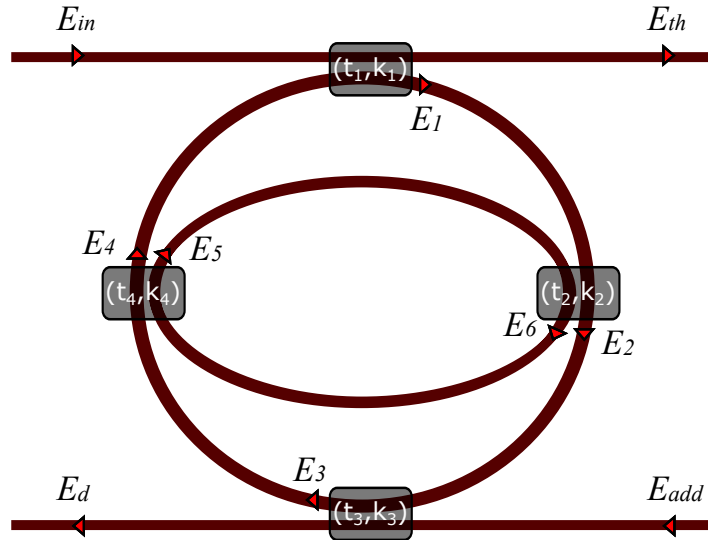
Figure 3.11: Schematic of embedded ring resonators.

The constitutive equations of the structure can be described by following equations:

$$E_d = k_3 E_2 \psi_{1,4} + k_3 E_{add} \tag{3.13}$$

$$E_{th} = t_1 E_{in} + k_1 E_4 \psi_{1,4} \tag{3.14}$$

$$E_1 = -k_1^* E_{in} + t1^* E_4 \psi_{1,4} \tag{3.15}$$

$$E_2 = t_2 E_1 \psi_{1,4} + k_2 E_5 \psi_{2,2} \tag{3.16}$$

$$E_3 = t_3^* E_2 \psi_{1,4} - k_3^* E_{add} \tag{3.17}$$

$$E_4 = t_4 E_3 \psi_{1,4} + k_4 E_6 \psi_{2,2} \tag{3.18}$$

$$E_5 = t_4^* E_6 \psi_{2,2} - k_4^* E_3 \psi_{1,4} \tag{3.19}$$

$$E_6 = t_2^* E_5 \psi_{2,2} - k_2^* E_1 \psi_{1,4} \tag{3.20}$$

where

$$\psi_{a,b} = \sqrt[b]{\alpha_a} e^{i\frac{\theta_a}{b}}. \tag{3.21}$$

Parameters α_a and θ_a, (a = 1, 2) are the loss coefficient and phase shift a-th ring resonators. Therefore, for instance, $\frac{\theta_1}{4}$ and $\frac{\theta_2}{2}$ indicate the quarter round-trip phase shift of the outer ring and half round-trip phase shift of the inner ring, respectively.

Derivation of the transfer function

For simplicity, one can assume that the couplers are lossless and neglect the phase shifts in the input and output waveguides. We can also remove $E_{add} = 0$ from the calculation and set $E_1 =1$. Thus we can insert (3.17) and substitute in (3.18) and (3.19). Then E_4 and E_5 become

$$E_4 = t_3^* t_4 E_2 \psi_{1,2} + k_4 E_6 \psi_{2,2} \tag{3.22}$$

and

$$E_5 = t_4^* E_6 \psi_{2,2} - t_3^* k_4^* E_2 \psi_{1,2}. \tag{3.23}$$

Next, (3.23) is substituted in (3.20),

$$E_6(1 - t_2^* t_4^* \psi_2) = -t2^* t_3^* k_4^* E_2 \psi_{1,2} \psi_{2,2} - k_2^* E_1 \psi_{1,4}. \tag{3.24}$$

One can write (3.24) by inserting (3.15) and (3.16) as

$$E_6(1 - t_2^* t_4^* \psi_2 + k_2^* k_4 t_1^* \psi_{1,2} \psi_{2,2}) = k_1^* k_2^* \psi_{1,4} - E_2(k_4^* t_2^* t_3^* \psi_{1,2} \psi_{2,2} + k_2^* t_1^* t_3^* t_4 \psi_1) \tag{3.25}$$

and its simplified version,

$$E_6 A = k_1^* k_2^* \psi_{1,4} - E_2 B \tag{3.26}$$

where $A = 1 - t_2^* t_4^* \psi_2 + k_2^* k_4 t_1^* \psi_{1,2} \psi_{2,2}$ and $B = k_4^* t_2^* t_3^* \psi_{1,2} \psi_{2,2} + k_2^* t_1^* t_3^* t_4 \psi_1$. Thus, E_6 can be expressed as

$$E_6 = (k_1^* k_2^* \psi_{1,4} - E_2 B)/A. \tag{3.27}$$

By substituting (3.27) in (3.15), (3.22) and (3.23), E_1, E_4 and E_5 can be expressed in terms of solely E_2 as

$$E_1 = -k_1^* + \frac{k_1^* k_2^* k_4 \psi_{1,4} \psi_{2,2} + E_2 (A t_1^* t_3^* t_4 \psi_{1,2} \psi_{1,4} - B k_4 t_1^* \psi_{2,2} * \psi_{1,4})}{A} \tag{3.28}$$

$$E_4 = \frac{k_1^* k_2^* k_4 \psi_{1,4} \psi_{2,2} + E_2 (A t_3^* t_4 \psi_{1,2} - B k_4 \psi_{2,2})}{A} \tag{3.29}$$

$$E_5 = \frac{k_1^* k_2^* t_4^* \psi_{1,4} \psi_{2,2} + E_2 (A t_3^* k_4^* \psi_{1,2} - B t_4^* \psi_{2,2})}{A} \tag{3.30}$$

Together with (3.28) and (3.30) allow us to extract E_2 using (3.16),

$$E_2 = \frac{Y + Z - A k_1^* t_2 \psi_{1,4}}{A + \sigma - X} \tag{3.31}$$

where
$X = A t_1^* t_2 t_3^* t_4 \psi_1 - B t_1^* t_2 k_4 \psi_{1,2} \psi_{2,2}$,
$Y = k_1^* k_2^* k_4 t_1^* t_2 \psi_{1,2} \psi_{2,2} \psi_{1,4}$,
$Z = k_1^* |k_2|^2 t_4^* \psi_{1,4} \psi_2$ and
$\sigma = A k_2 k_4 t_3^* \psi_{1,2} \psi_{2,2} + B k_2 t_4^* \psi_2$.
Finally, E_d at the drop port can be calculated by substituting (3.31) in (3.13) obtaining

$$E_d = k_3 \psi_{1,4} \left(\frac{Y + Z - A k_1^* t_2 \psi_{1,4}}{A + \sigma - X} \right) \tag{3.32}$$

as well as its explicit expression,

$$E_d = \frac{k_1^* k_3 t_4 \sqrt{\alpha_1} \alpha_2 e^{\frac{i\theta_1}{2}} e^{i\theta_2} - k_1^* k_3 t_2 \sqrt{\alpha_1} e^{\frac{i\theta_1}{2}}}{1 - t_2^* t_4^* \alpha_2 e^{i\theta_2} + t_1^* t_3 \alpha_1 \alpha_2 e^{i\theta_1} e^{i\theta_2} + k_2 k_4 (t_3^* + t_1^*) \sqrt{\alpha_1} \sqrt{\alpha_2} e^{\frac{i\theta_1}{2}} e^{\frac{i\theta_2}{2}} - t_1^* t_2 t_3^* t_4 \alpha_1 e^{i\theta_1}}. \tag{3.33}$$

In order to find the through port transfer function, it is needed to first substitute (3.31) in (3.29) then substitute the resulting E_4 in (3.14) which gives the through port (E_{th}) function as follows

$$E_{th} = t_1 + \left[\left(\frac{A k_1 t_3^* t_4 \psi_{1,2} \psi_{1,4} - B k_1 k_4 \psi_{1,4} \psi_{2,2}}{A} \right) \left(\frac{Y + Z - A k_1^* t_2 \psi_{1,4}}{A + \sigma - X} \right) + \frac{k_1^2 k_2^* k_4 \psi_{1,2} \psi_{2,2}}{A} \right]. \tag{3.34}$$

In agreement with power conservation, it can be verified that the lossless case requires $|E_{th}|^2 + |E_d|^2 = 1$. θ_1 and θ_2 are the round trip phase shifts of the outer and the inner ring, respectively. Since the two rings have different perimeters, their resonance wavelengths λ_1 and λ_2 can be found by $n_{eff} L_1 = m_1 \lambda_1$ and $n_{eff} L_2 = m_2 \lambda_2$ for the outer

and the inner ring. Phase shifts can be defined as $\theta_i = 2m_i\pi$ (i = 1 or 2), where m_i are integer numbers and L_1 and L_2 are the circumferences of the outer ring and the inner ring, respectively. It can be noticed from (3.33) that the phase shifts of the rings are combined in the ways of $e^{i2\pi(m_1+m_2)}$ or $e^{i2\pi(m_1+m_2)/2}$ for $e^{i\theta_1/2}e^{i\theta_2/2}$. Since m_1 and m_2 are integer numbers, the first term is always equal to 1. The second term can be either -1 or 1 depending on whether $(m_1 + m_2)$ is even or odd. Therefore, the through port or the drop port characteristics can change very rapidly according to the sign of the second term. If λ_1 and λ_2 are set to be equal, the device has two operation regimes according to whether $(m_1 - m_2)$ (representing phase difference) is an even or an odd number [37, 70].

We will investigate dual-ring coupled system for SOI structures. The situation refers to Case I when $(m_1 - m_2)$ is an even number, while Case II refers to $(m_1 - m_2)$ is an odd number. The SOI technology parameters (n_g and n_{eff}) are used in the analysis. Since we want to study the effects of coupling on the transmission behaviour of the device, we use coupling ratios (K) for ring-to-ring (K_2, K_4) and ring-to-bus waveguide (K_1, K_3) couplings, defined as $t_i = \sqrt{(1 - K_i)}$ and $k_i = \sqrt{(1 - |t_i|^2)}$. We first set symmetrical coupling ratios as $K_1 = K_3 = 0.4$ and $K_2 = K_4 = 0.2$ and assume lossless case ($\alpha = 1$). As shown in Fig. 3.12(a), the transmission profiles of the through port exhibit distinct results according to the phase difference of the coupled rings. The EIT-like effect can be observed when $m_1 - m_2 = $ odd number. A very narrow peak appears at $\lambda = 1547.1$ as a prominence with an enhanced power of 7 dB. In Case I, the profile switches to a flat pass-band transmission. It seems clearly from Fig. 3.12(b) that the phase profiles change dramatically depending on the phase difference of the two resonators that determines two distinct transmission profiles. Maximum effective phase change in a short wavelength range are about π and and 2π, for even and odd number, respectively.
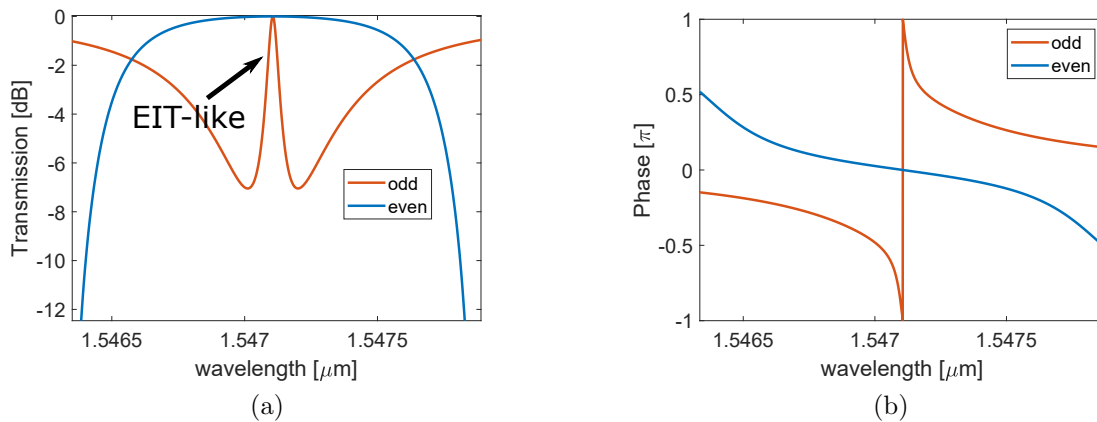
Figure 3.12: Through port transmission (a) and phase response (b) in Case I (even number) and Case II (odd number) when $K_1 = K_3 = 0.4$, $K_2 = K_4 = 0.2$ and $\alpha = 1$ (lossless).

On the other hand, the drop port spectra has transmission dips in both cases, as

shown Fig. 3.13. The notch in the Case II relates to the EIT-like peak of the through port spectrum, while in Case I, the transmission profile of the drop port splits into two and its stopband coincides with the flat-top passband in through port transmission. Maximum effective phase changes in the same range exhibit 2π and and π, for Case I and Case II, respectively.
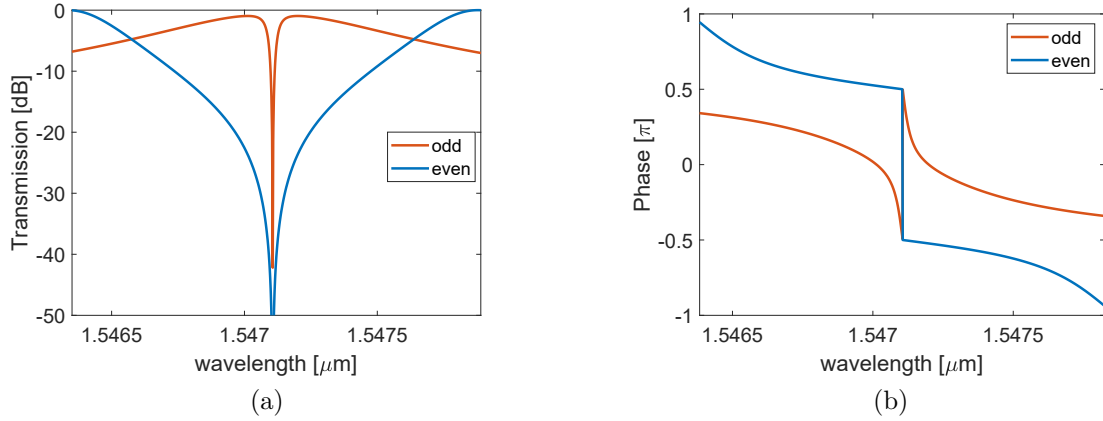
Figure 3.13: Drop port transmission (a) and phase response (b) in Case I (even number) and Case II (odd number) when $K_1 = K_3 = 0.4$, $K_2 = K_4 = 0.2$ and $\alpha = 1$ (lossless).

We can now study the effects of changes in the values of K_i in the device performance. In this analysis, we will study asymmetric coupling strengths of the inner ring, by changing value of K_4. The reason for this relies on the fact that considered embedded ring resonator provides versatile transmission characteristics because of the presence of the inner ring. According to the model, asymmetric coupling of the inner ring can strongly affect the transmission profiles that we have shown so far. As before, we will show the effects of asymmetric coupling in two separated cases as Case I and Case II.

Case I: $m_1 - m_2$ = even number

In Case I, we study passband evolution according to the coupling. In this case, we assume the loss is fixed as $\alpha = 0.99$ and ring-to-bus couplings are constant ($K_1 = K_3 = 0.4$). The tested values of K_4 ranges from 0.2 to 0.01, while K_2 remains equal to 0.2. The outer ring radius is selected as 20 μm and its phase shift according to inner ring is set as an even number. Note that, interchanging the values of K_2 and K_4 will result in the same transmission profiles, since we assume K_1 and K_3 are equal. Figure 3.14 shows the through port responses with different values of K_4, which induce asymmetric ring-to-ring coupling. Wavelength spacing between two consecutive transmission dips shown in Figure 3.14(b) decreased by 0.6 nm when a 20 times smaller coupling of K_4 with respect to K_2.

Furthermore, the asymmetric coupling has an impact on the transmission notches of the drop port spectrum. As shown in Figure 3.15 periodic doublet peaks with 45
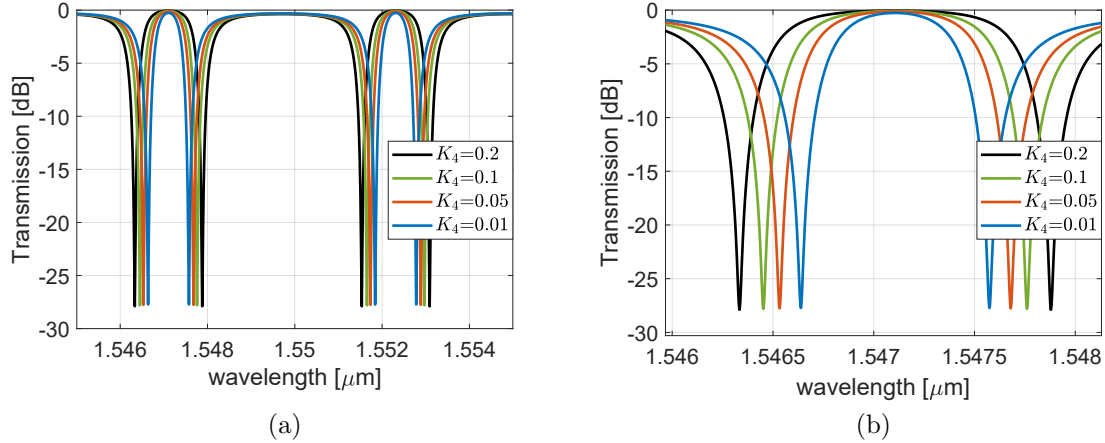
Figure 3.14: Through port transmission according to K_4 variation ($K_1=K_3=0.4$, $K_2=0.2$) (a) and zoom view (b).

dB of ER in the middle with the symmetric coupling experience a reduced ER in the notch for a smaller and asymmetric coupling. The ER reduction in this case is near 27.5 dB. The valley at 1.55 μm between two split consecutive resonances shown in Figure 3.15(a) can be further reduced by increasing ring-to-bus coupling of the outer ring as we will later show when we will compare single and embedded rings transmissions.
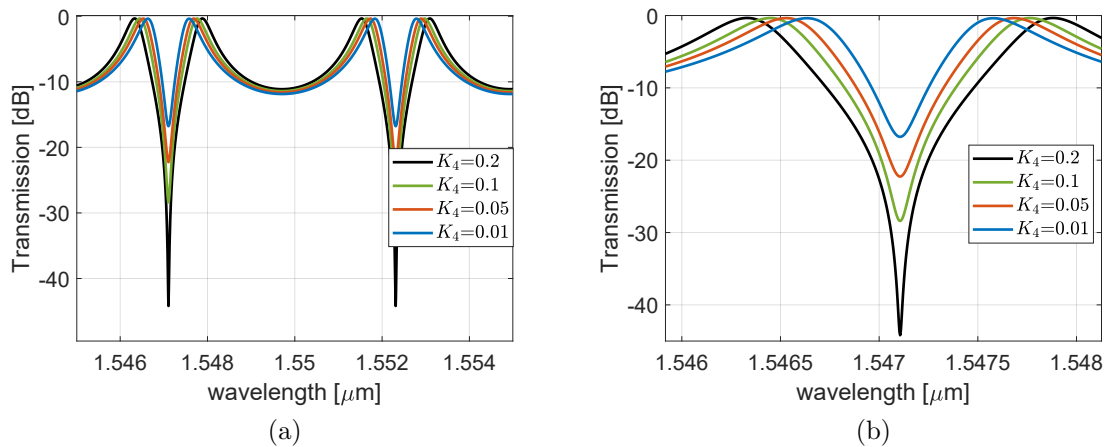
Figure 3.15: Drop port transmission according to K_4 variation ($K_1=K_3=0.4$, $K_2=0.2$) (a) and zoom view (b).

Case II: $m_1 - m_2$ = odd number

Now we can repeat the same analysis when the phase difference is set to be an odd number, keeping all other parameters equal to those used in Case I. As shown in Fig. 3.12, the through port can provide a narrow EIT-like effect when the ring-to-ring coupling is symmetric. This effect can be manipulated varying coupling coefficients. Figure 3.16 shows how the EIT-like effect is effected by decreasing K_4. In particular, there is transition from the EIT-like effect ($K_4 = 0.2$) to two split notches for small

coupling change (K_4 = 0.1). The bandwidth of the induced passband by decreasing coupling and its maximum are inversely proportional.
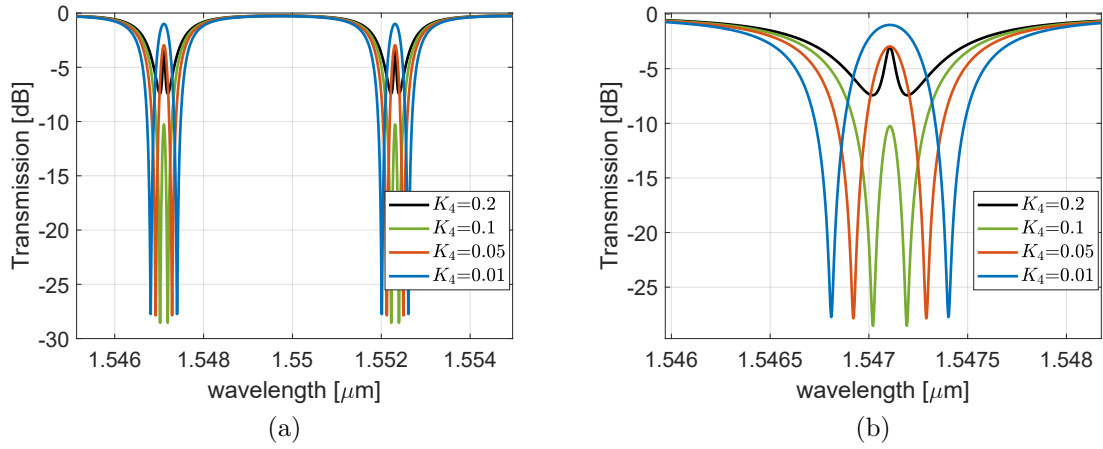
Figure 3.16: Through port transmission according to K_4 variation (K_1=K_3=0.4, K_2=0.2) (a) and zoom view (b).

Similarly to what happens in the through port transfer function, double peaks in the drop port separate from each other as well as decrease their ER at K_4 = 0.1. However, reducing the coupling coefficient will eventually increase the ER until it reaches the same value of the dip in the initial condition.
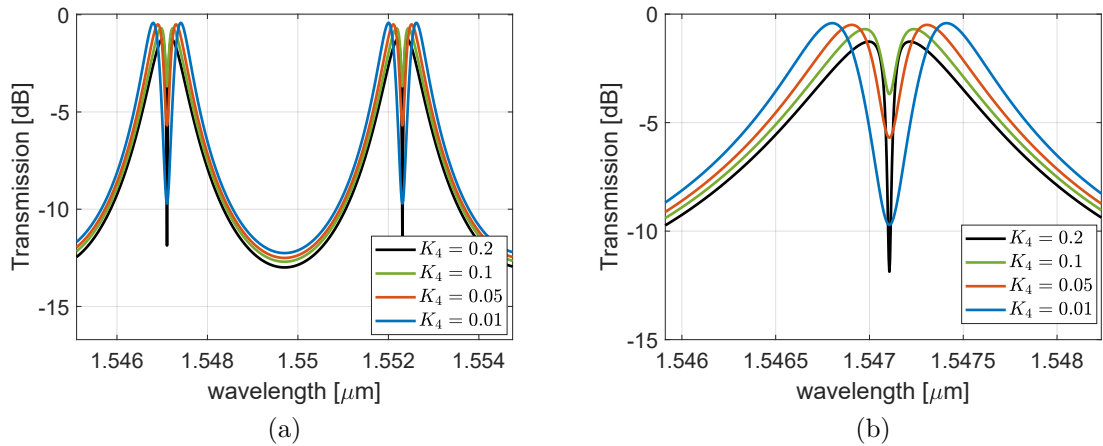
Figure 3.17: Drop port transmission according to K_4 variation (K_1=K_3=0.4, K_2=0.2) (a) and zoom view (b).

So far, we have considered the effects of asymmetric coupling between inner and outer ring coupling, by keeping the coupling of the outer ring and the bus waveguide as constant. The analysis developed until now reviewed embedded ring resonators characteristics and will be compared when we will present transfer function measurements of the SOI devices. Next, we will compare the resonance characteristics of the single and embedded ring resonators with the same parameters.

Comparison of single ring and embedded rings resonators

Letting the ring-to-ring coefficient K_2 and K_4 equal to 0, the embedded rings structure is converted into a single ring resonator with the radius of 20 μm. The transmission curves of both structures reported in Fig. 3.18 show that the FSR range of the single ring is divided into two parts so that the EIT-like effect and mode splitting occur in the embedded case corresponding to the resonance wavelengths of the single ring resonator when the phase difference $\Delta\theta$ is odd and even number, respectively. The FSR of the single ring in this example is 5.2 nm and narrower passbands of the embedded rings that centred single ring resonances have the notches separated by 1.6 nm.
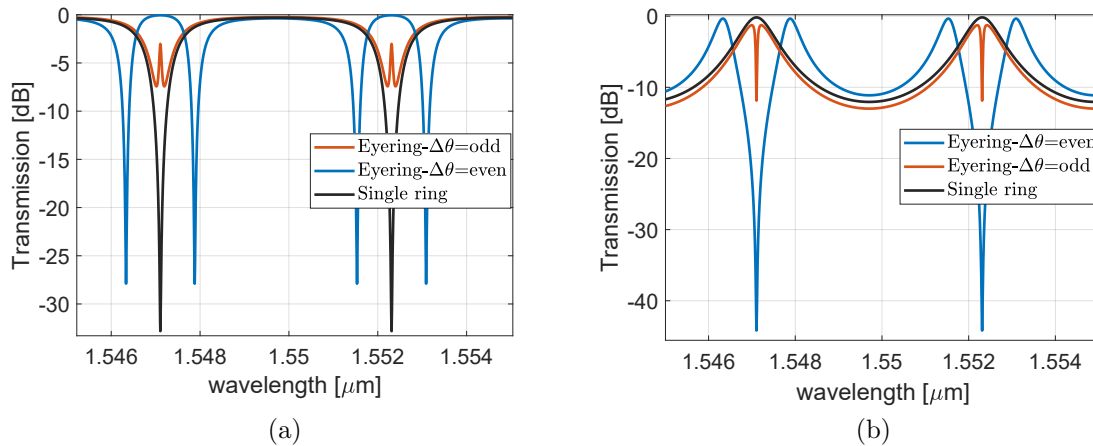
Figure 3.18: Comparison of the single and embedded rings transmissions in the through (a) and drop (b) ports according to even and odd phase difference conditions.

On the other side, similar behaviour of the drop port spectra of both structures can be seen in Fig. 3.18(b) in Case II. The transmission dips appear where the single ring resonant maximizes. This phenomenon can be seen in phase responses, as shown Fig. 3.19(b). While the Lorentzian curve of single ring resonance has a smooth transmission (similar to the through port of embedded rings in Case II), the effective phase changes of the embedded exhibit sharp transitions.

As previously mentioned, it is possible to enhance flatness of the bandwidth between two consecutive transmission dips at the drop port transmission, when the embedded is in Case I (see the referred band with the central wavelength of 1.55 μm in Fig. 3.18(b)). In this case, drop port passbands get wider and provide flat-top wide bandwidths that can be considered for super channel applications. We will investigate this proper as a next step of the analysis.

Obtaining flat-top wide passbands requires strong coupling between both rings and bus waveguides. In this time, we set larger ratios, $K_1 = K_3 = 0.9$ $K_2 = K_4 = 0.6$. Figure 3.20(a) shows the transmission spectra obtained with these parameters. The flat-top resonance wavelength (see the inset) have 3.25 nm of FWHM (equivalent to ~ 400 GHz) with 0.25 dB of fluctuation and 45 dB of ER in Case I. As opposed to single
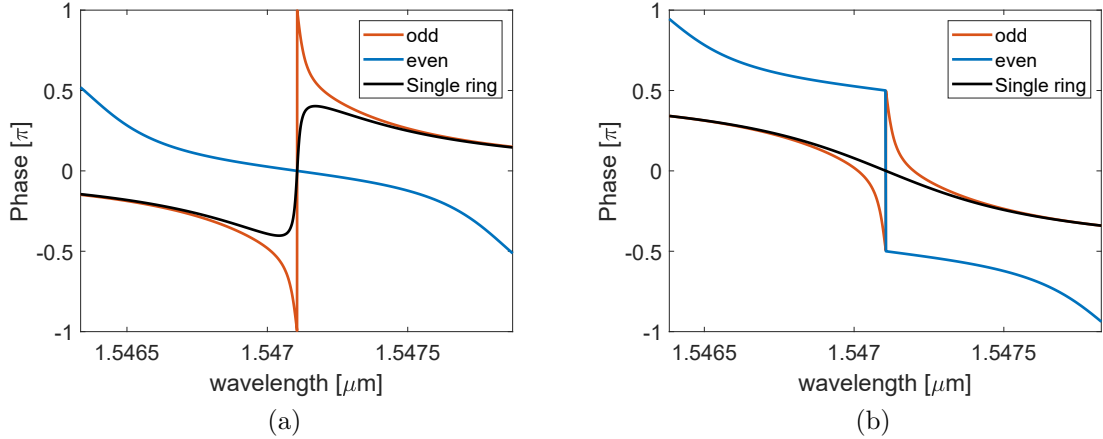
Figure 3.19: Phase change comparison of the single and embedded rings at the through (a) and drop (b) ports.

ring case, flatness and the bandwidth of drop port resonances of embedded rings can be greatly improved by a suitable tailoring of coupling coefficients. In the single ring case, as shown in Fig. 3.4(b), dropped signals loose their wavelength selectivity due to over coupling situation. In embedded case flattened resonances are the results of overcoupling. However, thanks to the presence of the second ring, it can still provide spaced transmission spectra with high channel rejection, when $m_1 - m_2$ is an even number.

Figure 3.20(b) shows the drop port bandwidth evolution between Case I and Case II. Letting $(m_1 - (m_2 + \Delta m))$, where $m_1 = 3$, $m_2 = 1$ and $\Delta m = [0\ 1]$, $m_1 - m_2$ becomes no longer integer number for $\Delta = 0.25$, 0.5 and 0.75 with 0.25 step of Δm. This allows to analyse the transition from Case I to Case II. Passband bandwidth in Case I decreases by increasing Δ. For example Yellow curve (see inset) has 2.4 nm of FWHM, which corresponds to ~300 GHz. In this case the reduction of bandwidth is 100 GHz with 0.75 dB of IL. When $m_1 - m_2$ becomes an odd number, bandwidth maximizes to ~ 600 GHz, with an IL around 4 dB. Therefore, by keeping the phase difference of the two resonators around even number it is possible to modify passband and in practice it can be carried out by thermal tuning of the inner ring.

Overall, distinct spectral characteristics of the embedded ring resonator can be achieved depending coupling and phase shifts treatments. According to this theoretical model, EIT-like effect and resonance splitting can interchangeably manipulate transmission of the through and drop ports. On the one side, symmetric ring-to-ring weak coupling takes advantage from sharp power enhancements. On the other side, strong coupling can enhance 3-dB bandwidth and passband flatness of the dropped resonances when the device is configured in Case I and such flat-top resonances can further be configured to wider passband setting the phase difference as Case II. Viability of bandwidth manipulation operations will be discussed in the next chapter with some measurement results on the SOI embedded rings.

(a)　　　　　　　　　　　　(b)
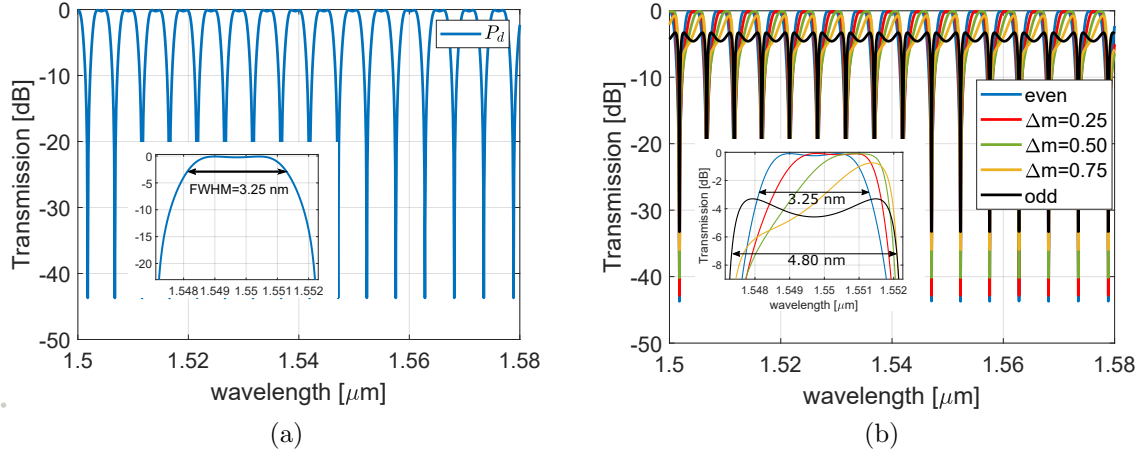
Figure 3.20: Flat-top passband of the drop port (a) in Case I and bandwidth evolution from $m_1 - m_2$=even to $m_1 - m_2$=odd number in four steps of Δm (b) ($K_1 = K_3 = 0.9$, $K_2 = K_4 = 0.6$, $\alpha = 0.99$).

3.3 Indirectly coupled micro ring resonators

Previous sections presented analytical models and principal transmission characteristics of existing devices. In this section, analytical modelling of the proposed device, indirectly coupled resonators (ICR), is presented. The working regimes such as wavelength routing and reflection and their related conditions are addressed.

Analytical modelling of indirectly coupled resonators

The schematic of the device, as well as the quantities necessary to describe how it works, are illustrated in Fig. 3.21. The incident (E_{in}), routing and outgoing (E_{p2}, E_{p3}, E_{p4}) complex mode amplitudes are grouped according to their propagation direction. The couplers with two waveguides (DC_1 and DC_2) are in vertical direction, while the three waveguide coupler (DC_3) is placed horizontally. In the schematic, the propagation direction of the positive superscript sign amplitudes is represented with red arrows, while the negative ones are green coloured.

Table 3.3 lists the design parameters that are used in the model. Starting by setting $E_{in} = 1$, the power transmissions at the output ports are normalized. The straight waveguides are assumed to be lossless ($\alpha_{wg}= 1$). This does not limit the validity of the results, since waveguide propagation loss contributes only to the overall insertion loss of the device. In the vertical direction, E_{p2} and E_{p4} are the field amplitudes at the drop ports connected by the crossing and E_{p3} is the field amplitude at the drop port. The distance between them, L_y, which is also the distance between the two vertical couplers, depends on the radius of the rings. The fields at one of the ports of the vertical couplers DC_1 and DC_2 can be defined as $E_{11}^{\pm} = E_{10}^{\pm} = e^{i\theta_y}= e^{i\beta_{wg}L_y}$, where the propagation constant $\beta_{wg} = 2\pi n_{eff}/\lambda$. Similarly, the central input (E_1^+) of DC_3 can be written as $E_1^+ = e^{i\theta_x}E_{in}$, where the phase shift between the input port and DC_3 is
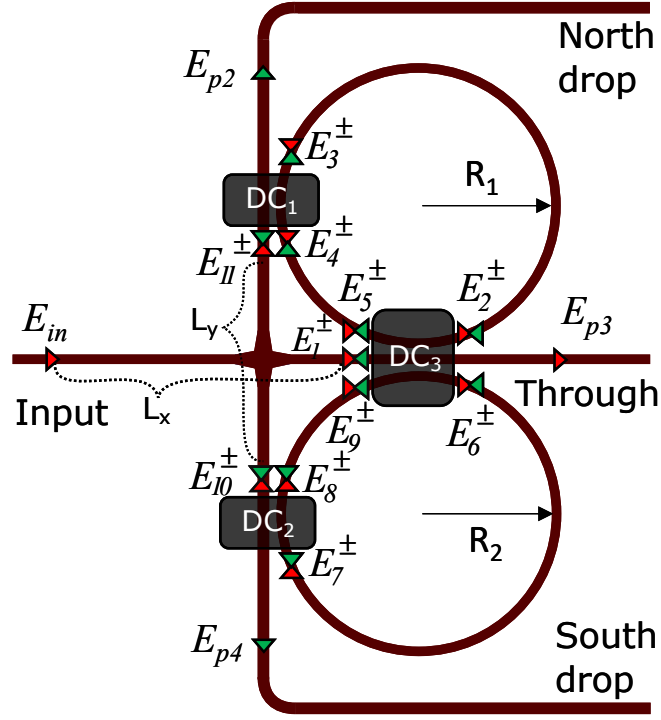
Figure 3.21: Schematic of the indirectly coupled resonators with indication of the mode amplitudes. Red coloured arrows represent the positive sign mode amplitudes while the green ones depict those of negative signs.

defined as $e^{i\theta_x} = e^{i\beta_{wg}L_x}$, and L_x is the length of the input waveguide measured from the excitation port.

Parameter	North ring	South ring	Waveguides
Radius	R_1	R_2	–
Loss coefficient	α_1	α_2	α_{wg}
Propagation constant	β_1	β_2	β_{wg}
Phase shift per round trip	θ_1	θ_2	–
Phase shift in horizontal wg section	–	–	θ_x
Phase shift in vertical wg section	–	–	θ_y
Coupler length of DC1	L_{c_1}	–	–
Coupler length of DC2	–	L_{c_2}	–
Coupler length of DC3	–	–	L_{c_3}
Coupling coefficient of DC1	κ_1	–	–
Coupling coefficient of DC2	–	κ_2	–
Coupling coefficient of DC3	–	–	κ_3

Table 3.3: Design parameters.

The coupling matrices of the two-waveguide coupling in DC_1 and DC_2 can be therefore defined as [49, 53, 69]

$$\begin{bmatrix} E_{p2} \\ E_3^- \end{bmatrix} = \begin{bmatrix} \cos(\kappa_1 L_{c_1}) & -i \cdot \sin(\kappa_1 L_{c_1}) \\ -i \cdot \sin(\kappa_1 L_{c_1}) & \cos(\kappa_1 L_{c_1}) \end{bmatrix} \begin{bmatrix} E_{11}^+ \\ E_4^- \end{bmatrix} \tag{3.35}$$

$$
\begin{bmatrix} E_{p4} \\ E_7^- \end{bmatrix} = \begin{bmatrix} \cos(\kappa_2 L_{c_2}) & -i \cdot \sin(\kappa_2 L_{c_2}) \\ -i \cdot \sin(\kappa_2 L_{c_2}) & \cos(\kappa_2 L_{c_2}) \end{bmatrix} \begin{bmatrix} E_{10}^- \\ E_8^- \end{bmatrix} \tag{3.36}
$$

and

$$
\begin{bmatrix} E_{11}^- \\ E_4^+ \end{bmatrix} = \begin{bmatrix} \cos(\kappa_1 L_{c_1}) & -i \cdot \sin(\kappa_1 L_{c_1}) \\ -i \cdot \sin(\kappa_1 L_{c_1}) & \cos(\kappa_1 L_{c_1}) \end{bmatrix} \begin{bmatrix} 0 \\ E_3^+ \end{bmatrix} \tag{3.37}
$$

$$
\begin{bmatrix} E_{10}^+ \\ E_8^+ \end{bmatrix} = \begin{bmatrix} \cos(\kappa_2 L_{c_2}) & -i \cdot \sin(\kappa_2 L_{c_2}) \\ -i \cdot \sin(\kappa_2 L_{c_2}) & \cos(\kappa_2 L_{c_2}) \end{bmatrix} \begin{bmatrix} 0 \\ E_7^+ \end{bmatrix}. \tag{3.38}
$$

Furthermore, the coupling matrices of the three-waveguide coupling in DC_3 can be defined as [71]

$$
\begin{bmatrix} E_2^+ \\ E_{p3} \\ E_6^+ \end{bmatrix} = \begin{bmatrix} c_1 + 0.5 & c_2 & c_1 - 0.5 \\ c_2 & 2c_1 & c_2 \\ c_1 - 0.5 & c_2 & c_1 + 0.5 \end{bmatrix} \begin{bmatrix} E_5^+ \\ E_1^+ \\ E_9^+ \end{bmatrix} \tag{3.39}
$$

$$
\begin{bmatrix} E_5^- \\ E_1^- \\ E_9^- \end{bmatrix} = \begin{bmatrix} c_1 + 0.5 & c_2 & c_1 - 0.5 \\ c_2 & 2c_1 & c_2 \\ c_1 - 0.5 & c_2 & c_1 + 0.5 \end{bmatrix} \begin{bmatrix} E_2^- \\ 0 \\ E_6^- \end{bmatrix} \tag{3.40}
$$

where $c_1 = \dfrac{1}{2}\cos(\sqrt{2}\kappa_3 L_{c_3})$ and $c_2 = \dfrac{-i}{\sqrt{2}}\sin(\sqrt{2}\kappa_3 L_{c_3})$. Since only the forward propagation excited from the input port is considered, the zeros in right hand side matrices have the meaning of non existing propagation from the output ports to the input one.

By solving above coupling matrices, the final explicit expressions of the drop ports (E_{p2}, E_{p4}), the through port (E_{p3}) and the reflection (E_1^-) can be derived as follows;

It can be seen from the Fig. 3.21 that $E_2^\pm$, $E_3^\pm$ and $E_6^\pm$, $E_7^\pm$ have phase differences of $e^{i3\theta_1/4}$ and $e^{i3\theta_2/4}$, respectively. Similarly, $E_4^\pm$, $E_5^\pm$ and $E_8^\pm$, $E_9^\pm$ have one quarter of total round-trip phase shift defined as $e^{i\theta_1/4}$ and $e^{i\theta_2/4}$. The constituting equations can be written from the coupling matrices for the $(+)$ signed amplitudes as

$$
E_2^+ = (c_1 + 0.5)E_5^+ + c_2 E_1^+ + (c_1 - 0.5)E_9^+ \tag{3.41}
$$

$$
E_3^+ = E_2^+ e^{i\frac{3\theta_1}{4}} \alpha_1^{\frac{3}{4}} \tag{3.42}
$$

$$
E_4^+ = E_3^+ \cos(k_1 L_{c1}) \tag{3.43}
$$

$$
E_5^+ = E_4^+ e^{i\frac{\theta_1}{4}} \alpha_1^{\frac{1}{4}} \tag{3.44}
$$

$$E_6^+ = (c_1 - 0.5)E_5^+ + c_2 E_1^+ + (c_1 + 0.5)E_9^+ \tag{3.45}$$

$$E_7^+ = E_6^+ e^{i\frac{3\theta_2}{4}} \alpha_2^{\frac{3}{4}} \tag{3.46}$$

$$E_8^+ = E_7^+ \cos(k_2 L_{c2}), \tag{3.47}$$

$$E_9^+ = E_8^+ e^{i\frac{\theta_2}{4}} \alpha_2^{\frac{1}{4}} \tag{3.48}$$

$$E_{10}^+ = -i * E_7^+ \sin(k_2 L_{c2}) \tag{3.49}$$

$$E_{11}^+ = E_{10}^+ e^{i\theta_{Ly}} \alpha_{Ly} \tag{3.50}$$

and the $(-)$ signed mode amplitudes,

$$E_1^- = c_2(E_2^- + E_6^-) \tag{3.51}$$

$$E_2^- = E_3^- e^{i\frac{3\theta_1}{4}} \alpha_1^{\frac{3}{4}} \tag{3.52}$$

$$E_3^- = E_4^- \cos(k_1 L_{c1}) - i * \sin(k_1 L_{c1})E_{11}^+ \tag{3.53}$$

$$E_4^- = E_5^- e^{i\frac{\theta_1}{4}} \alpha_1^{\frac{1}{4}} \tag{3.54}$$

$$E_5^- = (c_1 - 0.5)E_6^- + (c_1 + 0.5)E_2^- \tag{3.55}$$

$$E_6^- = E_7^- e^{i\frac{3\theta_2}{4}} \alpha_2^{\frac{3}{4}} \tag{3.56}$$

$$E_7^- = E_8^- \cos(k_2 L_{c2}) - i * \sin(k_2 L_{c2})E_{10}^- \tag{3.57}$$

$$E_8^- = E_9^- e^{i\frac{\theta_2}{4}} \alpha_2^{\frac{1}{4}} \tag{3.58}$$

$$E_9^- = (c_1 - 0.5)E_2^- + (c_1 + 0.5)E_6^- \tag{3.59}$$

$$E_{10}^- = E_{11}^- e^{i\theta_{Ly}}\alpha_{Ly} \tag{3.60}$$

$$E_{11}^- = -i * \sin(k_1 L_{c1})E_3^+. \tag{3.61}$$

According to the matrices (3.35),(3.36) and (3.39), the through port E_{p3}, north drop port E_{p2} and south drop port E_{p4} can be defined as

$$E_{p2} = E_{11}^+ \cos(k_1 L_{c1}) - i * \sin(k_1 L_{c1})E_4^- \tag{3.62}$$

$$E_{p3} = c_2(E_5^+ + E_9^+) + 2c_1 E_1^+ \tag{3.63}$$

$$E_{p4} = E_{10}^- \cos(k_2 L_{c2}) - i * \sin(k_2 L_{c2})E_8^-. \tag{3.64}$$

Starting from equation (3.41), by substituting the redefined E_5^+ and E_9^+ obtained from the equations (3.42), (3.43) and (3.46), (3.47), E_2^+ can be found as

$$E_2^+ = \frac{c_2 E_1^+ + M_2^- E_6^+}{1 - M_1^+} \tag{3.65}$$

and by substituting the same equations in equation (3.45), one can get,

$$E_6^+ = \frac{c_2 E_1^+ + M_1^- E_2^+}{1 - M_2^+} \tag{3.66}$$

where $M_{(1,2)}^\pm = (c_{(1,2)} \pm 0.5)\cos(k_{(1,2)}L_{c_{(1,2)}})e^{i\theta_{(1,2)}}\alpha_{(1,2)}$.

Finally, E_2^+ and E_6^+ can be written in terms of input port:

$$E_2^+ = \frac{E_{in}e^{i\theta_{Lx}}\alpha_{Lx}B_2 c_2}{A} \tag{3.67}$$

and

$$E_6^+ = \frac{E_{in}e^{i\theta_{Lx}}\alpha_{Lx}B_1 c_2}{A} \tag{3.68}$$

where $B_{(1,2)} = 1 - M_{(1,2)}^+ + M_{(1,2)}^-$ and $A = (1 - M_1^+)(1 - M_2^+) - M_1^- M_2^-$.

Using (3.67) and (3.68), all the other positive sign equations can be defined according to the input. Similarly negative signed E_2^- can be derived by substituting the equations (3.53), (3.54) and (3.55) (3.59), as follows

$$E_2^- = \frac{E_6^- M_1^- - i * \sin(k_1 L_{c1})e^{i3\theta_1/4}E_{11}^+}{1 - M_1^+} \tag{3.69}$$

whereas E_6^- can be redefined, by substituting the equations (3.57) , (3.58) and (3.59)

in (3.56), as follows

$$E_6^- = \frac{E_2^- M_2^- - i * \sin(k_2 L_{c2}) e^{i3\theta_2/4} E_{10}^-}{1 - M_2^+}.$$ (3.70)

Next, by substituting (3.70) in (3.69) one can get

$$E_2^- = \frac{-iE_{10}^- M_1^- \sin(k_2 L_{c2}) e^{i3\theta_2/4} - i(1 - M_2^+) \sin(k_1 L_{c1}) e^{i3\theta_1/4} E_{11}^+}{A}.$$ (3.71)

Since the E_{10}^- and E_{11}^+ are known from the previous calculations, the overall equation system can be solved with having explicit descriptions of $E_2^\pm$ and $E_6^\pm$. Therefore, the final explicit expressions of (3.62), (3.63) and (3.64) normalised to $E_{in} = 1$ can be found as

$$E_{p2} = \frac{-i \cdot \sin(\kappa_2 L_{c_2}) e^{i3\theta_2/4} \alpha_2^{3/4} e^{i\theta_x} e^{i\theta_y} [Ac_2(B_1 + B_2 M_1^- \sin(k_1 L_{c_1}) \sin(\kappa_2 L_{c_2})) + B_1 c_2 M_2^+]}{A \cos(\kappa_1 L_{c_1})}$$ (3.72)

$$E_{p4} = \frac{-i \cdot \sin(\kappa_1 L_{c_1}) e^{i3\theta_1/4} \alpha_1^{3/4} e^{i\theta_x} e^{i\theta_y} [Ac_2(B_1 + B_2 M_1^- \sin(\kappa_1 L_{c_1}) \sin(\kappa_2 L_{c_1})) + B_1 c_2 M_2^+]}{A \cos(\kappa_2 L_{c_2})}$$ (3.73)

along with the through port (E_{p3})

$$E_{p3} = \frac{2c_1 A + c_2^2 [B_2 \cos(\kappa_1 L_{c_1}) e^{i\theta_1} \alpha_1 + B_1 \cos(\kappa_2 L_{c_2}) e^{i\theta_2} \alpha_2]}{A}$$ (3.74)

and finally the reflection (E_1^-)

$$E_1^- = \frac{-c_2^2 \sin(\kappa_1 L_{c_1}) \sin(\kappa_2 L_{c_2}) e^{i3\theta_1/4} e^{i3\theta_2/4} e^{i\theta_x} e^{i\theta_y} B_1 B_2 (\alpha_1^{3/4} + \alpha_2^{3/4})}{A^2}$$ (3.75)

To better highlight the behaviour of the device, lossless rings with different radii have been initially considered. Depending on the phase condition at the resonance, two different transmission schemes are possible, as shown in Fig. 3.22 and Fig. 3.23. The former refers to the situation in which there are no common resonances for the rings (asynchronous case), while the latter is for the synchronous case, where at least a common resonance exists. This condition is used for routing applications of the device.

In the asynchronous case, all the resonances of the two rings are different, and the power reflected back to the input port is negligible. As seen from the Fig. 3.22(b), the reflected powers at the resonances are determined by the drop port (ER). In fact, for each resonance the only contribution to the reflection comes from the power re-routed toward the input port by the off resonant ring, and it is proportional to the ratio between the power at the through port and the power at the drop. This power re-routing toward the input port is also responsible for the transmission dips observed in the drop spectra.
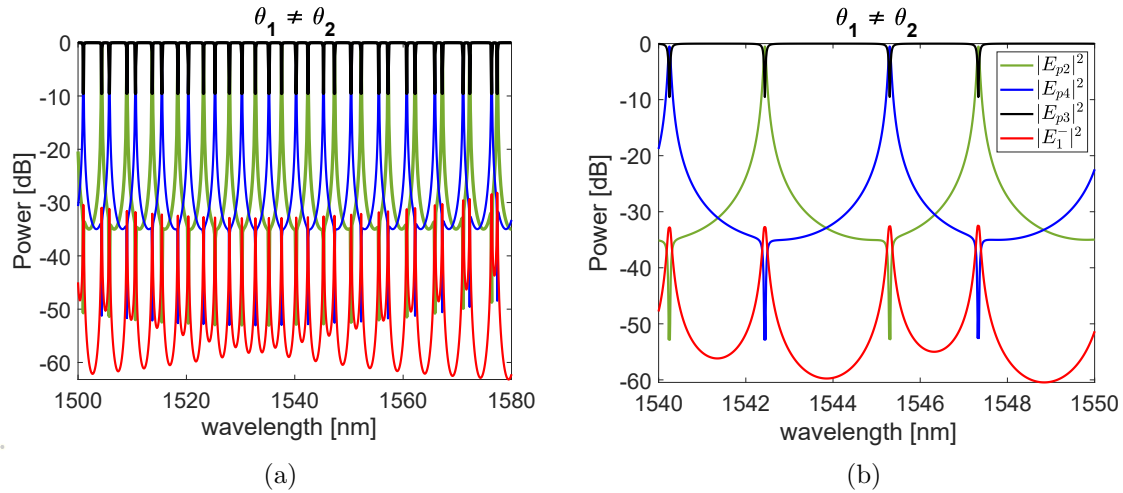
Figure 3.22: (a) Theoretical transmission spectra of reflection (Red), through (Black), North drop (Green) and South drop (Blue) ports, when all the resonances in the spectrum are in the asynchronous case ($\theta_1 \neq \theta_2$); (b) enlarged view in the central region of the spectrum.

When the two rings resonate at the same wavelength ($\lambda \simeq 1547$ nm in Fig. 3.23), i.e. in the synchronous case, the reflection reaches its maximum value. As one can notice, this is observed only for the wavelength corresponding to degenerate resonance modes. For non-degenerate resonant modes, i.e. for asynchronous resonances, the same behaviour previously described can be observed. Close resonances show reflection peaks too, but not as high as the one observed when the resonances of the two rings are synchronous. The side mode reflections, i.e. the reflections at non-degenerate resonances, have double peak profiles due to the proximity of the two different resonances with suppression (defined as the difference between the maximum intensity of the main peak and the maximum intensity of the strongest minor peak) below -15 dB.

The presence of a high reflection for the synchronous resonance has a direct impact also on the through and drop port transmissions, as it can be observed in the top inset of Fig. 3.23(b). Indeed, both through and drop ports have high transmission rejection in a very narrow band. The depth of these dips is related to the critical coupling condition. If the critical coupling condition is fulfilled, in fact, the device acts as an optical isolator with respect to the output ports and totally reflects the incoming light back to the input, as it will be discussed next.
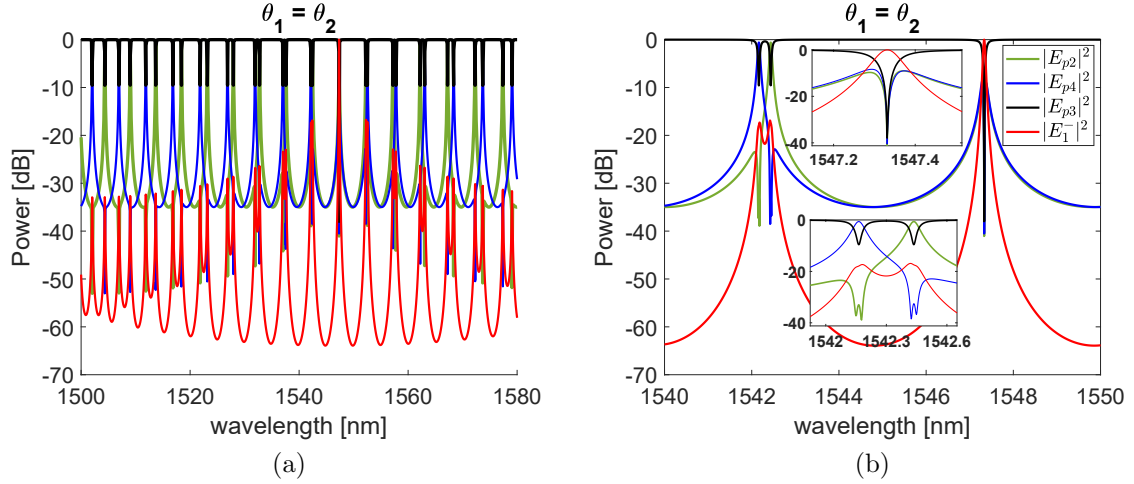
Figure 3.23: (a) Theoretical transmission spectra of reflection (Red), through (Black), North drop (Green) and South drop (Blue) ports, when a synchronous resonance exists ($\theta_1 = \theta_2$ for $\lambda \simeq 1547$ nm); (b) enlarged view with insets of the transmission curves for this resonance (top plot) and (bottom plot) for two asynchronous resonances.

Critical Coupling

As previously stated, in the single MRR, the critical coupling condition is present at the resonance when the propagation losses in the ring are compensated by the power coupled into it, if the coupler is assumed to be lossless [64]. In the ICR, if the rings have the same radii and the same coupling with the waveguides, they are synchronized in terms of round trip phase shift and new parameters can be replaced as it follows

$$
\begin{aligned}
\alpha_1 &= \alpha_2 = \alpha \\
\theta_1 &= \theta_2 = \theta \\
\kappa_1 &= \kappa_2 = \kappa_v \\
\kappa_3 &= \kappa_h.
\end{aligned}
\tag{3.76}
$$

Here, we describe new coefficients κ_v and κ_h as the vertical and horizontal coupling coefficients and the analysis mainly investigates their ratio. To make coupling strengths more significant in the solutions, they can be redefined as $\kappa'_h = \kappa_3 L_{c_3}$ and $\kappa'_v = \kappa_v L_{c_1} = \kappa_v L_{c_2}$. By substituting the new parameters from (3.76) into (3.74), one can get the through port function

$$
E_{p3} = \frac{2c_1 A + 2B c_2^2 \cos(\kappa'_v) e^{i\theta} \alpha}{A}.
\tag{3.77}
$$

Since the cavities are identical, A and B can be written as $A = (1 - M^+)(1 - M^+) - (M^-)^2 = (1 - M^+ - M^-)(1 - M^+ + M^-)$ and $B_{1,2} = (1 - M^+ + M^-)$ where $M_1^\pm = M_2^\pm = M^\pm$.

Finally, the simplified expression of the through port can be obtained as

$$E_{p3} = \frac{\cos(\sqrt{2}\kappa'_h) - \cos(\kappa'_v)e^{i\theta}\alpha}{1 - \cos(\sqrt{2}\kappa'_h)\cos(\kappa'_v)ei\theta\alpha}. \tag{3.78}$$

and the corresponding power can be written in the form

$$P_{p3} = |E_{p3}|^2 = \left| \frac{\cos(\sqrt{2}\kappa'_h) - \cos(\kappa'_v)e^{i\theta}\alpha}{1 - \cos(\sqrt{2}\kappa'_h)\cos(\kappa'_v)e^{i\theta}\alpha} \right|^2. \tag{3.79}$$

When the rings are on resonance, $\theta = 2\pi m$ and $m = 1, 2, 3...$, the critical coupling condition is found to be

$$\alpha = \frac{\cos(\sqrt{2}\kappa'_h)}{\cos(\kappa'_v)}. \tag{3.80}$$

As Eq. (3.80) shows, the critical condition holds when the internal cavity loss is equal to the power coupling ratio of the horizontal and vertical couplers. If the rings are lossless ($\alpha = 1$), the critical coupling ratio becomes $\kappa'_v = \sqrt{2}\kappa'_h$, which allows to define the ratio between the power coefficients in the form $K_h = K_v/2$. As a result of this condition, critical coupling is achieved when the horizontal power coupling is half of the vertical one. It must be pointed out that this condition reduces to the well known $K_h = K_v$ for the case of single micro ring resonator [65]. On the other side, in lossy cases ($\alpha < 1$) the critical coupling condition is met by specific values of κ'_h and κ'_v. From the design point of view, this means a need of optimization of either horizontal or vertical couplers according to the value of α, since the relationship between α and the ratio κ'_h/κ'_v defines the device performance in terms of ER of the through port and of IL of the drop port transmissions at the resonance.

Loss and coupling ratio analysis for the device performance

In this section, we investigate how the cavity radiation losses and the coupling coefficients of the horizontal and vertical couplers affect the transmission and the reflection characteristics of the ICR. The critical coupling condition for the double ring resonator is defined by Eq. (3.80). When this condition is verified, and rings are synchronous, the transmission is minimized and the reflection is maximized. However, examining how the device performs when this condition is not fulfilled can be useful to understand the role of the different parameters on the device behaviour.

The effects of the cavity radiation losses and of the power coupling ratio K_h/K_v on the reflection and on the transmission at the through and drop ports are illustrated in Fig. 3.24. In this analysis, K_h/K_v varies from 0.1 up to 2. The figure has two rows: the top line shows the results of the synchronous case ($\theta_1 = \theta_2$), for the wavelength of the peak of Fig. 3.23(b) near $\lambda = 1547$ nm. The figures on the bottom lines, on the contrary, refer to the asynchronous case ($\theta_1 \neq \theta_2$) and results for the resonant peak near

$\lambda = 1545$ nm of Fig. 3.22(b) are reported. Transmissions and reflections are all plotted in dB.

From the left side column plots it can be noticed that, regardless the phase shift conditions, there are certain cases where the ER reaches -45dB. On the other hand, the drop port transmission reduces by around -9 dB when the two rings are in phase at the common resonant wavelength. As shown in the right column plots, the highest value of the reflection, which is theoretically 0 dB, can only be achieved for the synchronous case (top row of Fig. 3.24) when the rings are lossless ($\alpha = 1$) and the horizontal coupling is half of the vertical coupling ($K_h/K_v = 0.5$). In the asynchronous case (bottom row of Fig. 3.24), the reflected light intensity at the resonance does not exceed -15 dB. For both cases, the reflection is very sensitive to ring losses, as it rapidly decreases when raising the attenuation inside the resonators.
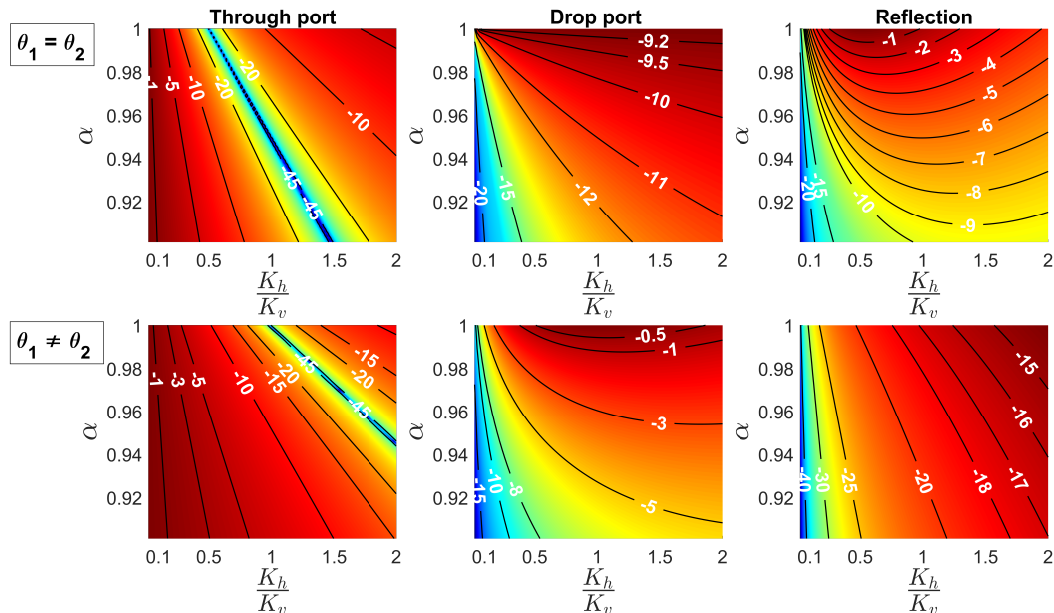
Figure 3.24: Relationships between the loss coefficient (α) and the power coupling ratio K_h/K_v of the horizontal and vertical couplers on the transmissions of the Through port (left column), Drop ports (middle column) and Reflection (right column). The upper row plots are for the synchronous case ($\theta_1 = \theta_2$) and refer to the common resonant wavelength $\lambda \simeq 1547$ nm, while the bottom row charts show the results for the asynchronous case ($\theta_1 \neq \theta_2$) when $\lambda \simeq 1545$ nm.

These results demonstrate that the device can be configured to exhibit, at a synchronous resonance, optical isolation at the transmission ports. In this case, in fact, the only outgoing field is the reflected one. Once the loss coefficient of the resonators is known, the coupling coefficients of DC_1, DC_2, and DC_3 can be designed accordingly. For instance, if $\alpha = 0.995$, in order to achieve a reflection > -1 dB (equivalent to a reflectivity of 0.794), the ratio K_h/K_v must lie between 0.4 and 0.75. To switch the operating regime from router to mirror, the two rings should resonate at the same wavelength simultaneously. Retrieving the routing operation will then require cancellation of simultaneous resonance. In this case, the overall phase difference is responsible for

wavelength separation of the two disjointed resonances.

These two distinct behaviours will be exploited in the next chapters to use ICR for wavelength routing (chapter 4), reflection (chapter 5) and sensing (chapter 6) applications.

3.4 Conclusions

In this chapter, the analytical models of single, embedded and indirectly coupled ring resonators have been developed by using the TMM approach. Key points for a successful design of performing devices, considering silicon-on-insulator technology parameters, have been discussed. The results of the static transmission characterization of the single micro ring resonators have been presented. The FSR of the measured single MRRs range from 7.85 to 3.75 nm for the radii of 12 to 25 μm. Moreover, the measured FWHMs were between 0.08 and 0.16 nm with the corresponding Q-factors of 9700 and 19500. The obtained thermal tuning parameters were 95 pm/°C of temperature variation and 110 pm/mW of applying power.

An analytical model of the horizontally embedded ring resonators has been provided. The transmission characteristics of the device have been reviewed. Transformation of the electromagnetically induced transparency (EIT) effect into the resonance splitting effect was illustrated by manipulating ring-to-ring coupling and phase shift difference of the coupled resonators. Next, the device has been studied under a strong coupling condition. Very wide flat-top resonances with 400 GHz of bandwidth, 0.25 dB of IL and 45 dB of ER were demonstrated. Bandwidth reconfiguration has been illustrated by the transition from the even number to odd number phase difference. The obtained bandwidth range of the drop port transmission was 100 GHz to 600 GHz, with 0.75 and 4 dB of IL, respectively.

Finally, an analytical model of the Type-I indirectly coupled resonators (ICR) was presented. Possible operational regimes and their conditions were discussed. Depending on round-trip phase shift differences of the two resonators, the device can exhibit wavelength routing and reflection. The conditions for maximizing single wavelength reflection and dual wavelength routing operation were studied by investigating coupling ratios of the horizontal and vertical couplers and loss coefficient.

Chapter 4

Wavelength routing properties of indirectly coupled resonators

4.1 Introduction

Due to bandwidth limitations at high speed data transmission in electronic interconnection, photonic interconnect technologies provide the most viable solutions to intra and inter chip wavelength division multiplexing (WDM) communication at higher datarate with lower latency and lower power consumption, e.g. in traffic routing in data centers [72] and even inside many core computing systems in form of optical Networks-on-Chip (NoC) [73]. The need for MRRs appears in WDM technology as their spectral filtering characteristics allow performing de/multiplexing processes of optical signals. Wavelength routing in NoCs can be implemented with cascaded MRRs [19, 21–23, 74] and for many aspects, ring resonator based switching architectures may differ in footprint, number of routing wavelengths or scalability [75].

In response to ever increasing IP traffic demand in fiber-optic communication, optical links with fixed granularity wavelength spectrum in the C-band face spectrum efficiency problems since the frequency grid permits transmissions of only a certain number of wavelengths. As an alternative, the flexible or elastic optical networks can successfully address several issues in the dynamic management of transmission bandwidth and wavelength routing algorithms for the next generation optical networking [76–78]. In this framework, a reconfigurable optical add-drop multiplexer (ROADM) in an optical node should have some properties such as colourless, directionless and contentionless (CDC) [79]. Colourless represents the ability of the switch to handle all the wavelengths available in the WDM link. On the other hand, contentionless is a property according to which two channels with the same wavelength can be processed simultaneously, while directionless interconnects WDM channels regardless of incoming or outgoing direction. As presented in [80], three main design architectures, broadcast-and-select, route-and-select, and wavelength-selective can implement ROADM following different approaches. Due to topological constraints, broadcast-and-select and route-and-select

architectures suffer from contention and they need modifications to become contention
free [80].

On the other hand, wavelength selective architectures, where add/drop operations
are carried by wavelength selective switches (WSS), are of special interest because
of their degree of configurability. WSSs can in fact act as transponder aggregators
to realize multi degree CDC ROADM nodes [81, 82]. Ring based switching matrices
can be fully reconfigurable as long as the resonant wavelength of each ring switching
element in the network is controlled by electronics. In order to avoid interference,
each ring is responsible of routing a single WDM signal. Thus, its FSR should be wide
enough to by-pass other wavelengths when the ring is in off state, i.e. not configured to a
spcific wavelength. The main drawback of ring topologies is scalability. Interferometric
crosstalk in routing paths can be significant when number of rings increases in the
switch fabric. Implementing inter connectivity between a certain number of the input
and output ports depends on the switch topology. Therefore, number of the rings
required in the switch fabric for a given number of interconnection is an important
scalability parameter to deal with the power consumption and crosstalk.

4.2 Concept of wavelength routing in micro ring resonators

In this section we introduce wavelength routing approaches in MRR topologies. An
example of cross-grid single MRR is illustrated in Fig.4.1. In this configuration, the
input wavelengths λ_1, λ_2 and λ_3, highlighted with different colors, represent individual
WDM channels and it is assumed that the resonance wavelength of the ring is λ_1.
When port number 1 is set as the input port (see Fig.4.1 (a)), λ_1 is routed to port 3,
while the other wavelengths are by-passed toward to through port indicated number
4. If port 2 is selected as an input, then the drop and through ports are switched as
shown in Fig. 4.1(b). In this case as opposed to the first one, λ_1 is retrieved at port 4.
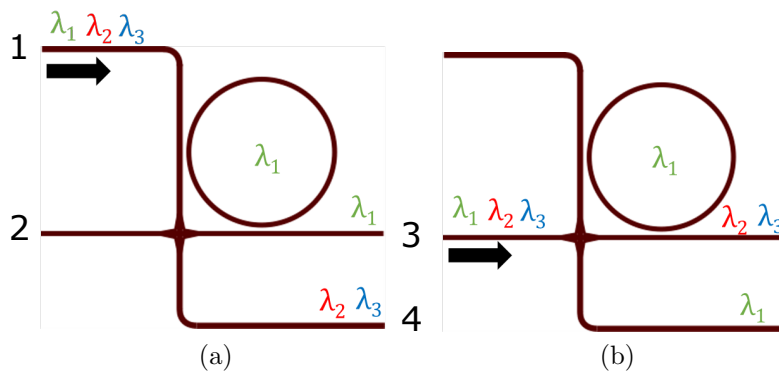
Figure 4.1: Wavelength routing operation of single cross-grid MRR.

Next, wavelength routing of dual cross rings in cross-grid configuration is illustrated

in Fig. 4.2. This configuration deals with two wavelengths that can be routed simultaneously by setting up the rings to resonate at the same wavelength. It is known as the basic photonic switching element (PSE) in scalable NoC architectures [83, 84]. As depicted in Fig. 4.2(a), among the incoming wavelengths at port 1, λ_1 is received at port 3. In the other case (b), drop port becomes number 4, as shown in the single ring case (see Fig.4.1(b)). Thanks to the its topology based on twin rings, PSEs allow to process multi wavelengths routing and are one of the most common devices in NoCs.
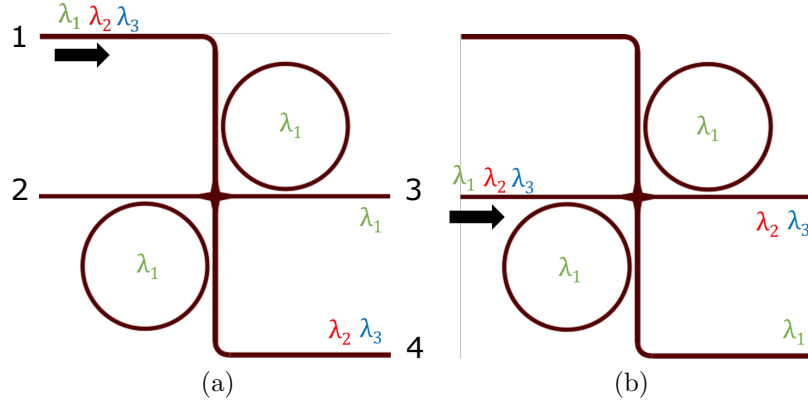
Figure 4.2: Wavelength routing operation of dual rings in cross-grid configuration (known as basic switching element (PSE)).

In the following, the new switching element ICR, previously decribed in chapter 3, will be illustrated. This switch looks interesting since it is a reconfigurable structure, able to act both as a router and a mirror. In both cases tunability can be driven by integrated heaters. In the rest of this chapter the router functionality will be illustrated. In chapter 5, its operation as a mirror will be shown .

Wavelength routing operations of the indirectly coupled resonators is illustrated in Fig. 4.3. In this configuration, the device can handle two sets of wavelengths simultaneously. In the first case, shown in Fig. 4.3 (a), the upper ring routes λ_1 to the port 4, while λ_2 propagates to port 2, which is dropped by the lower ring. In these operations, each ring routes the wavelengths in opposite direction and the two wavelengths get separated in two drop ports. If the port 3 is set as input, Fig. 4.3 (b), the routed wavelengths exchange the drop ports. Wavelength routing directions in ICR alter according to the incident one. In both configurations, two sets of wavelengths are routed at each time. Therefore the device exhibits non-reciprocal behaviour in terms of wavelength routing characteristics. This phenomenon is the core property of the presented device. Note that the term non-reciprocal in our case refers to wavelength routing directions according to excitation port of the bus waveguide. Illustrations presented in Fig. 4.3 will be referred to as Type-I (a) and Type-II (b) to emphasize the different routing paths. By doing so, it is similar to those shown in Fig. 1.5.

By benefiting from the non-reciprocal property of ICRs, it is possible to introduce novel switching topology since it gives the ability of bidirectional operations as well as it extracts two sets of wavelengths from the bus instead of one. Dropping two
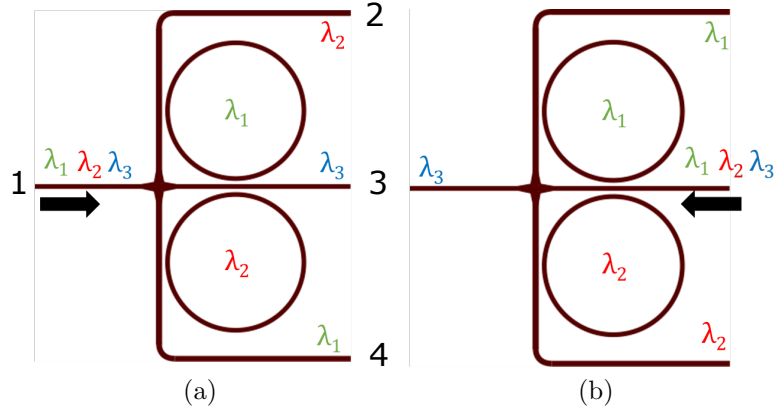
Figure 4.3: Wavelength routing operation of the Type-I (a) and Type-II (b) ICR.

wavelengths at the time allows to reduce the overall footprint of the circuit: one stage with only two rings allows to do so instead of two stages with 4 rings, with the first clear advantage of a reduction of 50% of the necessary tuning switching elements in the overall system. Next sections investigate two case studies. The first introduces a switch fabric based on ICRs to reveal bidirectional communication in a transponder aggregator of CDC-ROADM systems. The second compares the PSE and ICR by means of scalable interconnectivity in NoC applications to generalize N×N (N input and N output) contention-free wavelength routing matrices.

4.3 ICR based bidirectional add/drop transponder aggregator architecture

A four directional CDC ROADM architecture for access network is illustrated in Fig. 4.4. The wavelength selective switches (WSS) in the Optical Line Switch (OLS) distribute the desired WDM wavelengths to the add /drop sections where the Transponder Aggregators (TPAs) interconnect the receivers (RXs) and transmitters (TXs). The advantage of the use of TPAs relies on the fact that the connectivity between the transponders and OLS can be reconfigured in all-optical way without manual intervention [85]. In the concept of flexible optical networks, the integrated MRRs can be densely integrated as a switch fabric in TPA architectures. For instance, in [86], thermally tunable MRRs based ROADM in Si_3N_4/SiO_2 technology have been demonstrated for access networks. In [20], a 4 channel ring based CDC ROADM architecture has been implemented in SOI technology. In both ROADM architectures, the switch matrices were constructed by MRRs in the cross-grid configuration, as illustrated in Fig. 4.1.

The preliminary research on the proposed scheme in this thesis is carried out by considering previously reported architectures and photonic devices used in those schemes such as interleavers and Multiplexers (MUXs). The main difference is the switching
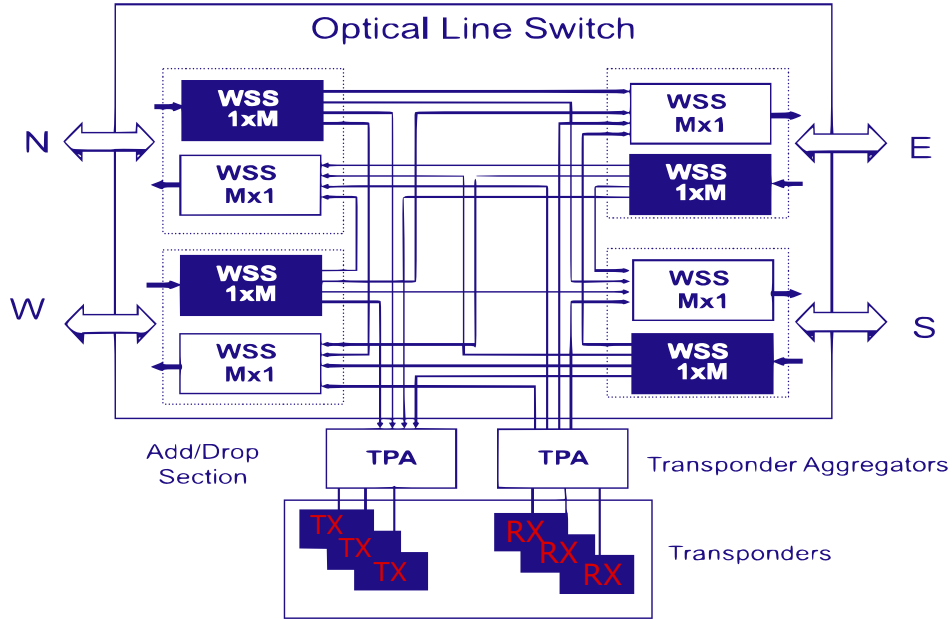
Figure 4.4: Colourless/Directionless/Contentionless (CDC) ROADM architecture (reproduced from [85]).

matrix where, in our architecture, we used Type-I and Type-II ICR that are combined in a single matrix and we profited from the non-reciprocal routing property to introduce bidirectional communication in the TPA.

The schematic of the proposed 2-direction 4-channel ICR based TPA architecture is depicted in Fig. 4.5. The scheme consists of four 1×4 MUXs (orange colored), 8 interleavers, 8 ICRs, two circulators and two TX/RX units. Each MUX is responsible either for drop or add functions and multiplexes four different wavelengths in such a way that the wavelengths are labelled according to the output configuration. In the Add MUX, wavelengths should be connected to each output in a given sequential order (the related wavelengths are labelled as $\lambda_1, \lambda_2, \lambda_3, \lambda_4$) and this process can be implemented by arrayed waveguide gratings (AWGs). However, the wavelength order, in fact, is not necessary for the Drop MUX, since each MUX processes only one wavelength, thus as an alternative to AWG, wavelength combiners could also provide this function. The interleaver (INT) separates wavelengths regarding of either odd or even number of the wavelength, which has been also used in the architecture presented in [20]. INT filters provide channel spacing to group odd and even number WDM signals and can be realized by cascading integrated Mach-Zehnder interferometers [87]. Finally, the circulators divert the dropped signals to the RX and the TX signals to the Add MUXs. The circulators presented in the architecture are the devices that facilitate bidirectional operations. They do not strictly have to be integrated since the process can be implemented by fiber-optic circulators. The integrated part of the scheme consists of AWGs, INTs, the switching matrix and their waveguide connections. Considering further integration possibilities of circulators, an integrated optical circulator on silicon is demonstrated in [88].
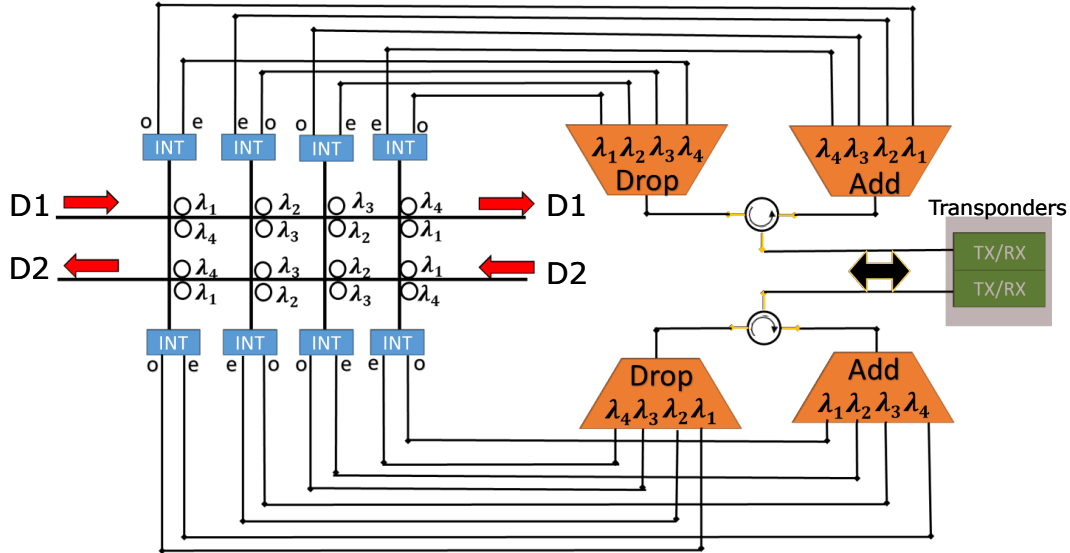
Figure 4.5: Proposed 2-direction 4-channel Bidirectional CDC TPA architecture.

In this architecture, WDM channels arrive in the switching matrix from the two different directions, D1 and D2 represented by the red arrows, are either added or dropped by the cascaded ICRs in each row. Since each ring operates at a fixed resonance wavelength, the scheme can handle four WDM channels simultaneously. Wavelength ID assignments in the matrix follows a specific configuration rule: the North rings wavelength IDs in the upper part of the first row (D1) follow an ascending order, while the South ones follow descending order. When the second direction (D2) is introduced, the previous order configuration is reversed. This method ensures that each INT in the same column receives identical drop wavelengths regardless of direction and routes the dropped wavelengths to the Drop MUX. For instance, the first upper INT in left hand side receives only λ_4 from each row and can be used only for λ_1 for add function. Since λ_4 has an even number id, the even number (e) output of the INT is connected to the Drop MUX, while its odd number port (o) is connected to the Add MUX. The described design rule is developed based on non-reciprocal routing property, such that D1 and D2 wavelengths are handled by the Type-I and Type-II ICRs, respectively. By applying the same approach to the other columns, switching matrix can be configured to meet colourless, directionless and contentionless properties and utilized for both Add/Drop functions. When a ring should not add or drop any wavelength, it is then driven in off state by the control voltage on heaters.

For the sake of simplicity, the illustrated scheme supports 2 directions, 2 add/-drop functions for 4 wavelengths, named $2 \times 2 \times 4$ ROADM, however it can have more directions by adding more rows and columns in switching matrix.

An example of Add/Drop functions of a WDM signal (λ_4 of the last column of D1) is illustrated in Fig. 4.6. The WDM channel in direction D1 is previously selected by the WSSs from the ROADM ports (N, W, E, S) to be dropped for transponders. The switch fabric made by ICRs accommodates the desired WDM channel to the

transponders unit. In the Drop function, the routed wavelength λ_4 (Blue colour path) at the fourth stage transmits to the even number output port of the INT, and then it is received by the transponder via the lower Drop MUX and circulator. As the first three stages (columns) can handle the other WDM channels simultaneously, the system can be considered as colourless. When the input direction is flipped, the dropped signals are then processed by the upper branch of the circuit.
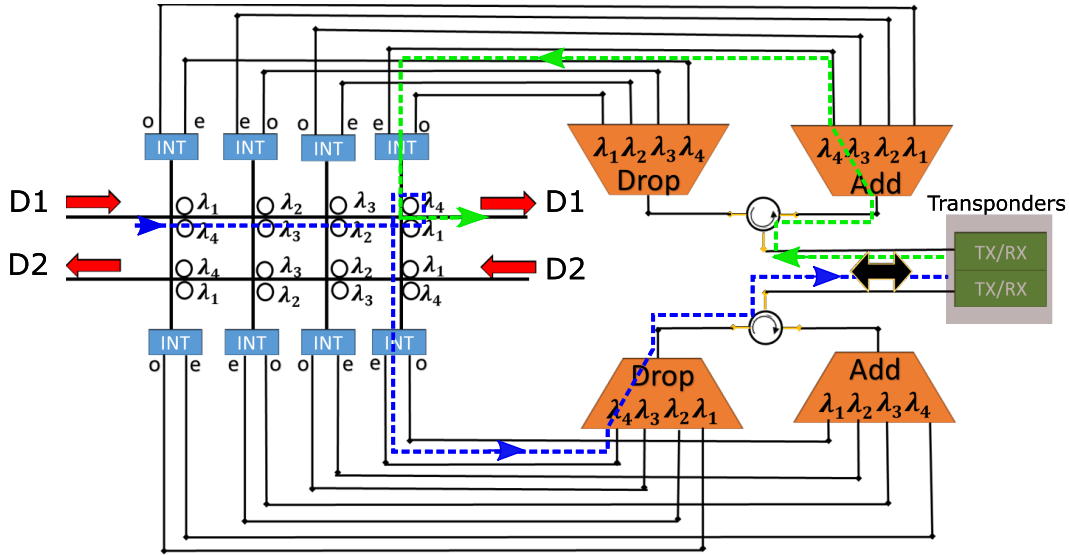
Figure 4.6: An example of Add/Drop functions in bidirectional CDC TPA.

When λ_4 should be added to D1, the signal coming from the transponder unit is sent to the input of the Add MUX by the circulator (Green colour path) and then arrives to the same ring that was previously assigned. So, both add and drop channels are processed by the same ring resonator to implement connectivity to D1. Therefore, the proposed structure can perform bidirectional communication between the aggregation section and the transponder unit.

As shown in Fig. 4.4, ROADM architecture performs add and drop operations in two separated blocks. Nevertheless the previously reported architectures based on MRRs brought innovative solutions to improve conventional non-CDC ROADMs, they still use two individual switching matrices for each add/drop block. According to [89], combining add/drop wavelengths bidirectionally in the same switching matrix can reduce the cost of Add/drop function in ROADM by 40-50%, even though it may require the use of additional circulators. To the knowledge of the author, a MRR based bidirectional CDC-TPA has not been proposed yet. A complete realization of the proposed TPA architecture with a validated performance in real applications might open new possibilities to reduce the cost of add/drop implementations in the flexible optical networking.

Until now, wavelength routing features of ICRs have been exploited for a specific utilisation for inter-node connectivity in the flexible optical networking. In the next section, we elaborate scalability capabilities of ICR based Network-on-Chip in a more

generalised manner, including also applications of intra-chip such as core-to-core communication on-chip applications.

4.4 Topology investigation of ICR based wavelength routing matrices in Network-on-Chip

In this section, we elaborate scalability properties of ICR based wavelength router topology for optical NoCs applications. NoCs are becoming more and more attractive for inter and intra-chip communication [90]. However, one of the main issues in the NoC systems is crosstalk due to the inter-channel crosstalk in WDM channels that limits the implementation of reliable communication systems [91,92]. This problem can be limited by using high Q-factor rings, but cannot fully eliminated. Therefore, reducing the number of rings in switching matrices without compromising switch capacity is an important issue for large scale wavelength routers. As previously mentioned and shown in Fig. 4.2, the standard photonic switch element (PSE) uses two sets of rings as the first stage routing element. Cascading multi switching element allows to implement higher connectivity on-chip networks. The way of cascading basic structures determines topology. One of the main criteria of photonic switching fabrics to realize compact and energy efficient NoCs is scalability. Number of switching element in NoCs is proportional to number of connectivity and every topology has its own scalable characteristics.

It is worthy to underline that NoC routing matrices do not necessarily have to be directionless, which was a must for flexible ROADM systems, since core-to-core connectivities in an optical layer of an chip can be fixed in a given switching matrix. Instead, contentionless (or non-blocking) property is the main criterion in NoC applications, because each core in IC layer must be able to communicate to all the other cores with a certain number of wavelengths.

The simplest version of PSE and ICR are, in fact, first stage 2×2 wavelength routers and both of them are composed of two rings. The comparison of PSE and ICR based topologies will be made in terms of number of rings required to implement N×N networks. To do so, we first investigate how an ICR based routing fabric scales up by cascading multiple elements. Schematics of 4×4 and 6×6 ICR routers are depicted in Fig 4.7. Here the input and output ports are labelled as Ii and Ti (i=1,2,3,...), respectively. Red and Blue arrows represent the direction of the incoming and outgoing wavelengths. In these schemes, the number of available WDM wavelengths is equal to the number of connections (N). As shown in Fig. 4.7(a), each row has two stages where the resonance wavelengths of each ICR are set to be odd number for upper rings, and even number for the lower rings. The type of ICR in each row differs according to the direction of incoming signals. For example, the rings in the first row exhibit routing profile of Type-I ICR to the direction I1, which it turns into Type-II according

to direction of I3. Therefore, regardless of the direction, two blocks in the row handle four different wavelengths.
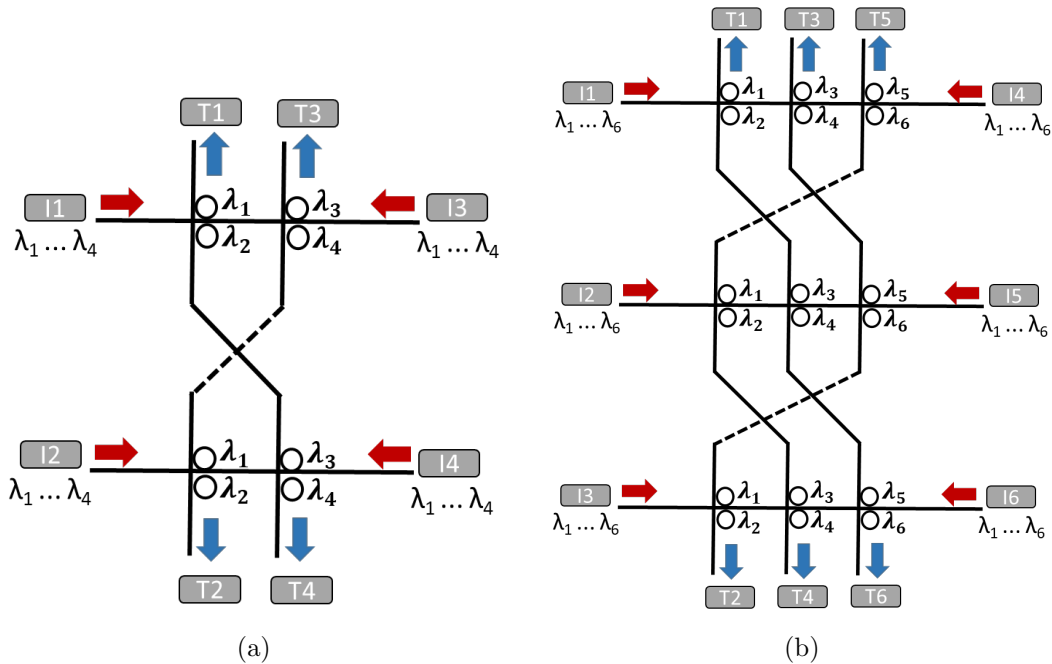
Figure 4.7: ICR router topology: 4×4 (a) and 6×6 (b) non-blocking routers.

In order to accommodate full connectivity available to every output, two rows must be inversely connected to each other, i.e. each vertical waveguide must be connected to all the other rings with both even and odd number resonances. These are the design criteria to avoid contention, considering each input port must be assigned to only one wavelength but in case it should be able to reconfigure to other wavelengths. The router is reconfigurable, but once all the connections are established, the matrix remains unchanged until the next reconfiguration. We can check contention-free channel assignments as it follows: T1 can be assigned to λ_1 and λ_2 through the first stage ICR of the upper row. In this case, I1 and I3 ports use λ_2 and λ_1, respectively. Similarly, other WDM channels such as λ_3 and λ_4 can be available via the second stage ICRs in the lower row. Thereby, a complete set of wavelengths is available to establish communication links between T1 and all the other input ports.

The presented non-blocking 4×4 wavelength router has 4 ICRs with total 8 rings. By introducing a new set of row and column, the matrix becomes 6×6. Similarly, row connections starting from the upper side are made by joining to a successive stage in each row. Following this way, 6×6 non-blocking router requires 18 rings in total. Now we can calculate number of rings needed for N^2 connectivity. As said before, the number of WDM channels is determined by N number ports. ICRs in the routing fabric deals with N (channel number) × N (connectivity) for a non-blocking scheme. Since each ICR handles two sets of wavelengths, generalized expression for determining required number of rings to built N×N routing fabric can be defined as $\dfrac{N^2}{2}$, as well as,

$\dfrac{N^2}{4}$ number of routing elements if we count each ICR as an individual routing element.

We now can compare the scalability of an ICR with the conventional PSE based router called λ-router [93]. As reported in [94], λ-routers can provide non-blocking scalable routing matrices that need to use $\dfrac{N(N-1)}{2}$ number of PSE to construct N×N network. Since, similarly a PSE has two rings, total number of the required rings can be defined as $N^2 - N$.

The scalability evolution of λ-router and ICR topologies in terms of the required number of the rings is illustrated in Fig. 4.8. The difference between them rapidly increases as the matrix scales and eventually reaches ~ %50 when $N = 16$. This result shows that having the abilities of non-reciprocal behaviour and handling routing of two wavelengths in each element can significantly reduce the number of the ring used in the router. Taking into account that rings in the systems should be tunable, ICR based configurations can reduce power consumption of NoCs in the sense of large scale intra-connections.
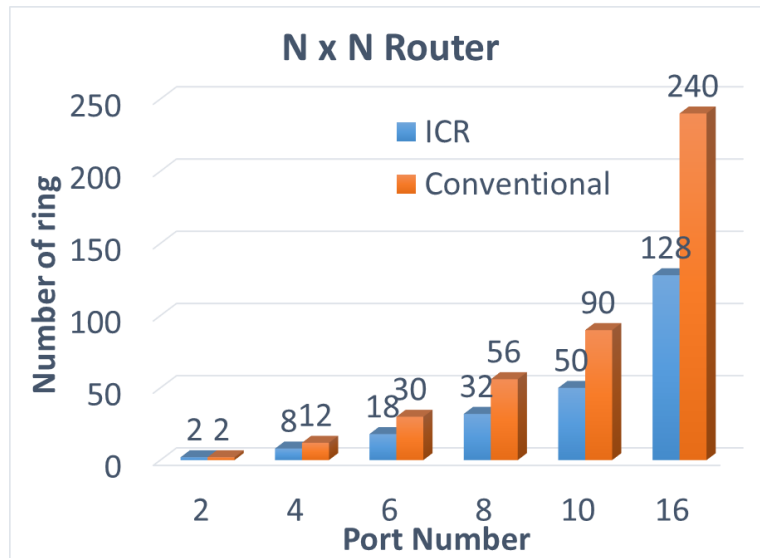
Figure 4.8: Scalability of ICR and conventional λ-router.

Next, we make a global comparison of ICR based topology with the existing topologies in the literature, including also non-ring based topologies. There are various routing fabric implementations presented so far. For instance, Mach–Zehnder interferometer based topology [95], also some other topologies called Beneš [96] and Clos [23]. Recently, a silicon PSE based 8×8 network called Omega is experimentally demonstrated in [24]. A recent survey presents a comprehensive comparison of silicon based switch topologies and their scalability formulations [97]. According to the provided formulas in that paper Beneš topology is commented as the best choice, because it has the minimum number of switching elements to construct a non-blocking network. The total number of switching elements of Beneš topology was reported $\dfrac{N}{2}(2log_2N - 1)$. In comparisons to Beneš, ICR based networks still have fewer number of elements up to 16×16. On the other hand, for larger networks, Beneš still has an advantage over

ICRs based routers in terms of scalability. However, the Beneš topology is a rearrangeably non-blocking architecture. Therefore, it needs a specific routing algorithm to provide non-blocking routing, which is theoretically implemented only on a MZI based switching fabric [97].

It is important to underline that when the ICR based networks grow, the number of waveguide crossings increase by introducing new columns and rows in the system. For instance, in the 6×6 router illustrated in Fig. 4.7(b), the last stage vertical couplers must be connected to those of the first stage. To do that, the waveguides must traverse the two vertical connections of the first and second stage. Therefore, waveguide crossings in the circuit should be optimized in terms of crosstalk and insertion loss to provide feasible NoCs.

So far, ICRs have been theoretically illustrated. In the next section, we evaluate networking performances of individual Type-I and Type-II ICRs and PSE as well as single ring devices by means of Bit Error Rate measurements.

4.5 Networking analysis of micro ring resonators

4.5.1 Description of the BER setup

To evaluate the performance of the investigated devices in terms of their capabilities to provide digital transmissions, a setup for the measurement of the Bit Error rate (BER) has been implemented. For the devices investigated in this thesis, the main interest was in evaluating communications performances of the switching elements. For this purpose, a simple and low-cost system based on commercial on-the shelf components has been implemented. The setup for BER evaluation, in fact, is based on a FINISAR FTLX6824MCC Tunable XFP Optical Transceiver and on a Silicon Labs Si5040 10 Gbps XFP Transceiver (see the photograph in Fig. 4.9).
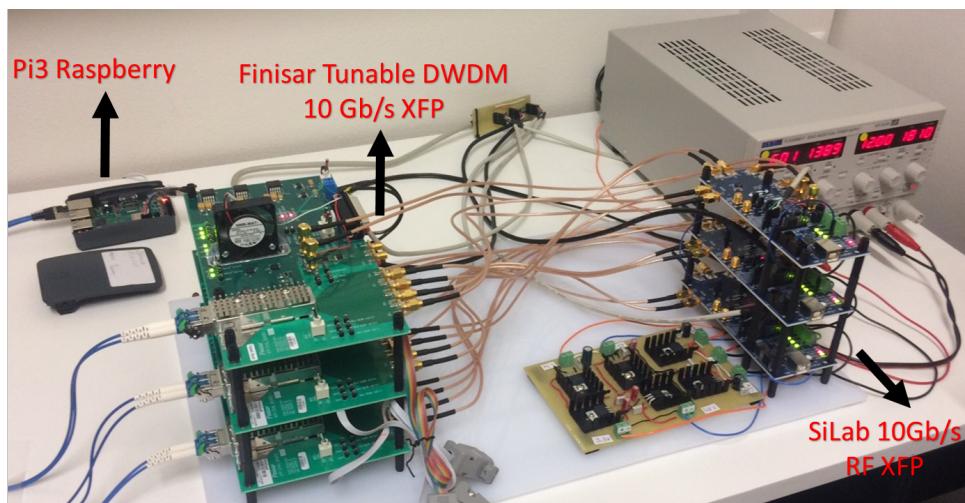
Figure 4.9: The equipment for BER measurements.

The FINISAR FTLX6824MCC is a 10Gbit/s Multi-Protocol Tunable DWDM Op-

tical Transceiver used for up to 80 km links. It supports from 8.5 Gb/s up to 11.35 Gb/s on a 50 GHz ITU-based channel spacing (C-Band). This device is used for DWDM 10 Gb/s SONET/SDH, DWDM 10 Gb/s Ethernet and DWDM 10 Gb/s Fibre Channel applications. The FTLX6824MCC is installed on a FINISAR FDB-1044 Evaluation Board, which ease the connection of the Transceiver with the required Power Supply, with the Input/Output RF signals and with the I2C bus used for its control, initialization and interrogation during the working procedures.

The Silicon Labs Si5040 is a complete, low-power, XFP transceiver suitable for multiple XFP module types, from short-reach datacom to long-reach telecom applications. The Si5040 can be programmed for Line loopback, pattern generation, and pattern check tests through a serial micro controller interface available through an I2C bus. The use of its Evaluation Board eases, also in this case, programming and managing of all the operations. In this section, for the application of interest, the fundamental block is the TX Pattern Generator, which is programmed to provide the modulating RF signal for the FTLX6824MCC Laser. The signal received from the FTLX6824MCC Integrated Photodetector is driven to the RX port and, once processed to optimize the detection process, driven to the RX Pattern Check block, which is used for BER evaluation.

The two cards are managed via their I2C bus. Commands are sent through a Raspberry Pi 3 Model B+ card controlled with Matlab using a remote Personal Computer connected to the Raspberry PI with a TCP-IP network. In this way, a single computer is used to handle all the measurement procedures through devices coordinated via the Matlab Instrument Control Toolbox. A Matlab script managing signal generation/recognition and BER evaluation, laser and photodetector setup, amplifier and attenuation control has been suitably developed in the IOPLab (University of Ferrara), where I and other undergraduate students have contributed to realize the setup. Fig. 4.10 illustrates a sketch of the basic setup used for BER measurements. The Si5040 and the FTLX6824MCC are controlled on their I2C bus by using a Raspebrry Pi 3. The setup includes also an Erbium Doped Fiber Amplifier (EDFA) and a programmable attenuator, which are connected to the computer via a GPIB interface. The Optical Amplifier is needed to compensate the losses introduced by the Device Under Test (DUT) and by the connections of the different components of the setup. The use of the fixed attenuator is mandatory as the available EDFA does not allow a minimum gain below 23 dB and the minimum accepted power at the input of EDFA is -6 dBm. The pass-band optical filter positioned before the photodetector reduces the optical noise generated by the amplifier. The variable attenuator allows measurements of the BER as a function of the received power. In this setup, the input power at the EDFA is maintained fixed and, during the measurements, the optical power at the receiver is reduced progressively to allow BER evaluation. If the DUT has a too high attenuation, as it happens for butt-coupled devices, a second amplifier after the DUT could

be introduced. In this setup, a single laser source is considered. With this setup, Back to Back (B2B) and single channel measurements are allowed. For B2B, the DUT is replaced with an attenuator having the same attenuation of the insertion loss of the DUT. Alternatively, a direct connection of the output to input fiber through a straight waveguide or via the through port of the DUT can be used. When WDM measurements are desired, two other lasers are added to reproduce the existence of two interfering channels acting on the central channel under test. The three channels are coupled with a 4×1 optical coupler realized by using three 2×2 optical couplers suitably cascaded. The overall attenuation of this input coupler is of about 9 dB in the whole extension of the C-band.
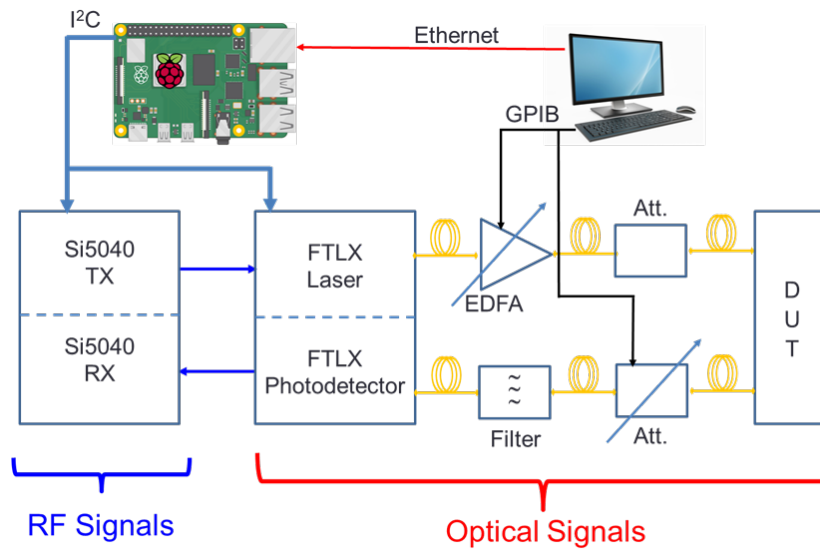
Figure 4.10: Sketch of the measurement setup, which includes the Si5040 and the FTLX6824MCC cards, a filter, a fixed attenuator, an Erbium Doped Fiber Amplifier and a Programmable Attenuator.

The measurement procedure is managed through a Matlab script, which controls all the instruments of the implemented setup. The script initializes the laser sources (by selecting the desired channels, in the case of a WDM evaluation, or by selecting the single wavelength of the source when a B2B or a single channel BER evaluation is requested by the user) and the attenuation needed at the first step of the measure. Then the laser and the EDFA are turned on and once the EDFA provides sufficient power, the Si5040 is initialized to perform the BER evaluation. BER measurements are performed by varying the attenuation until the power level on the Photodetector reaches the lower limit. In this way, BER vs the Received Power is evaluated. The Si5040 is usually configured to generate and check a pseudo-number PRBS31 10Gbps bit sequence with a pattern length of of $2^{40} - 1024$. User defined bit sequences are possible too, and considered when the system is tested, to allow visualization on an oscilloscope.

The Si5040 is used in the implemented setup to modulate the FTLX6824MCC XFP transceiver. The Laser of the transceiver can be modulated with 10Gbps NRZ

signals. The carrier, corresponding to the central frequency of the channel, can be configured via the I2C bus to emit on standard DWDM channels in the C-Band. This transceiver supports 50GHz ITU-based channel spacing (C-Band) and when a DWDM BER measurement is required, three adjacent channels are initialized. Each channel is allocated at a different wavelengths and modulated with a signal coming from a dedicated Si5040 card. The optical signal collected at the output of the DUT can be amplified again, depending on its intensity, and then sent to the receiver section of the XFP transceiver to be demodulated. A second amplification can be required if the insertion loss of the DUT is too high. In fact, it is not possible to strongly amplify the optical signal with the first amplifier, to avoid damages in the optical components (polarizer, optical circulator, etc.) before the DUT, and on the DUT. The RF signal at the output of the Photodetector contained in the FTLX6824MCC XFP transceiver is then returned to the receiver section of the Si5040, for BER evaluation. During the measurements, the system is kept under control through different monitors managed by the Matlab script. In particular, transmitted and received powers, amplifier gain and the attenuation introduced by the variable attenuator are initialized at each step of the process. Moreover, both the interrupt warnings and alarms (such as Los of Signal, Loss of Lock, Received Power under the threshold limit, etc.) of the XFP transceiver and of the Si5040 are continuously checked, to exclude anomalous behaviour of these devices. For each step of the measurement, the attenuation of the variable attenuator is increased, in order to reduce the received power at the photodetector. The measurement is terminated when the attenuation reaches its maximum assigned value. If, during the measurement, the received power drops below the threshold (- 35 dBm), the measurement is stopped as the BER reaches, in this case, its maximum.

Before presenting the obtained results from BER evaluations, it is needed to mention some stabilization issues of the described setup. During measurements processes, we often faced unexpected laser signal power reductions. We observed transmitting, and then receiving, power oscillations occurring in the FINISAR modules. We think that the problem of unexpected oscillations (tens of dBs) is related to software synchronizations of the laser sources and their master SiLabs modulator. These sharp and repetitive power reductions resulted in abnormal BER values, which were quite unrelated to previously obtained ones. We noticed that in case of this problem, both laser and modulation modules need to be restarted a couple of times. Also, in some steps of during the measurement process, due to the lack of software synchronization, systems interrupted, resulting zero BER values. To overcome this problem, each measurement step for with the same values of attenuation is repeated two times, the ones interrupted in the BER calculations were later removed from the results and rest of values were used to obtain final BER vs. Received Power curves.

4.5.2 Results of BER measurements

Prior to BER measurements, the resonance wavelength of the DUT is thermally tuned to 1550.50 nm, which is the central communication channel. The other two interfering channels at 1550.10 and 1550.90 nm were introduced, when needed, to simulate multi wavelength communication. Resonance wavelength alignment is checked by the OSA and when the maximum transmission of the communication wavelength at 1550.50 nm is achieved, BER evaluation process is initiated.

Figure 4.11 shows the BER measurements as a function of the received power of the single ring resonator with a radius of 19 μm. Ports are labelled as shown in the inset. All B2B curves presented in this section have been obtained from through port transmissions of the measured devices. Since the resonances were shifted away from the communication wavelength during B2B evaluation, this approach is similar to that of replacing the DUT with a variable attenuator in the setup. Propagation of the resonance modes from port 1 to port 3 and port 2 to port 4 can have, in fact, different paths. While the former can by-pass waveguide crossing, in the latter, signal passes through the waveguide crossing twice. However, determining the crossing induced crosstalk and its possible power penalty is a difficult task simply by testing a single or a few cascaded rings crossings. It is also possible that errors in BER calculation can be more significant than a single crossing induced power penalty. In fact, T1$\rightarrow$ R3 and T2$\rightarrow$ R4 communications do not show any significant penalties. Additionally, the normalized static transfer functions shown Fig. 4.11(b) confirm that the transmission difference of the resonances that travel in different paths can be negligible. We assume that the insertion loss and crosstalk of the waveguide crossing are low and perform similarly (0.04 dB of insertion loss and -45 dB of crosstalk) as reported in [98].

Static transmission measurements, i.e. evaluation of the transmitted power as a function of the wavelength when using a non-modulated signal, of the DUT shown together with the BER results have been previously obtained by using the setup illustrated in Fig. 2.4 in chapter 2. The reason of this is due to the fact that the polarization of the introduced WDM signals in BER evaluations is different from that of the tunable laser. Therefore, polarization control on the resonance wavelengths of the DUT must be re-adjusted according to the fixed WDM signal of the laser source. This avoids to obtain true static transmissions over a wavelength span because of the polarization mismatch of the TLS and fixed communication signals, since only one polarization controller for the input fiber was available. In addition, the bandwidth variable filter placed therefore, photodetector of RX was fixed for a narrow band (~ 3 nm) to limit the EDFA induced noises. However, thanks to the OSA that receives a portion of output signal via 90:10 splitter, the control of tuned resonance wavelength of the DUT to 1550.50 nm was possible before the BER measurements were initiated.

The results of the PSE resonator are shown in Fig. 4.12. The measured device has two rings with radii $R_1 = 20$ μm and $R_2 = 19$ μm. The experiments are implemented
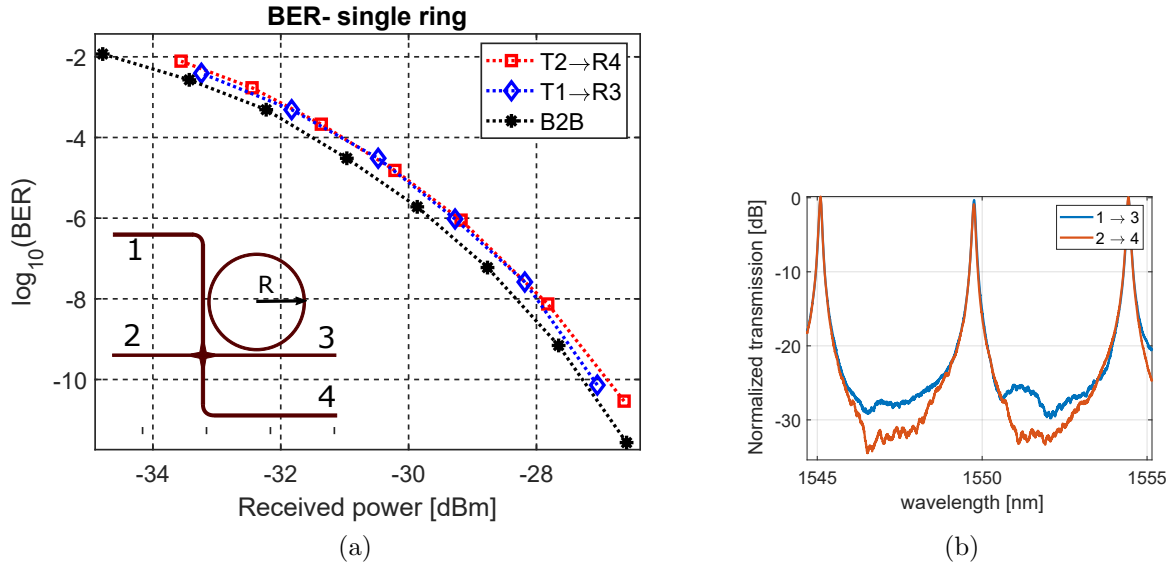
Figure 4.11: BER measurement of single ring resonator (a) and static transmission (b) without applied voltage.

by tuning both rings to the central wavelength. Once the T1→R3 curve is obtained, the fibers are set on the port 2 and port 4 without altering the present resonance. Similar to the results obtained on the single ring resonator, T1→R3 and T2→R4 show minimal penalties. As it can be noticed from the figure, the BER curves stop at different received power levels. This is due to two main issues, the first one is related to the power stabilization issues of the setup itself as explained before. The second one is due to fact that small variations in applied voltage (order of mV) can cause slight resonance shifts, so the received powers varies depending on thermal stabilization of the DUT. As a result, each measurement has its own average received power.

To investigate networking performance of PSE under the condition shown in Fig. 4.2, where the two rings should resonate at the same wavelength, we removed the bandwidth variable filter from the setup to obtain the static transmissions of the PSE shown in Fig. 4.12(b). In fact, each drop port of the PSE contains the two resonances of individual rings, because of its topology. It can be seen that the Red curve obtained from the transmission from port 2 to port 4 has two resonances labelled as λ_N and λ_S, representing the resonances of the upper and lower rings. Once the rings are tuned at the same wavelength (yellow curve) near 1549.7 nm, the WDM signal is set accordingly and the bandwidth filter reintroduced in the setup. Then the BER evaluation is implemented. In this case T2→R4 communication performance is compromised. The measured power penalty at BER = 10^{-9} is found to be 0.8 dB. The worsened networking performance, which is albeit limited in our measurement, shows that PSE based switching fabrics might suffer from interferometric crosstalk when a switching element in the fabric must route two identical wavelengths simultaneously in order to avoid contention.

Next, we investigated networking performances of Type-I and Type-II ICRs. We

(a)   (b)
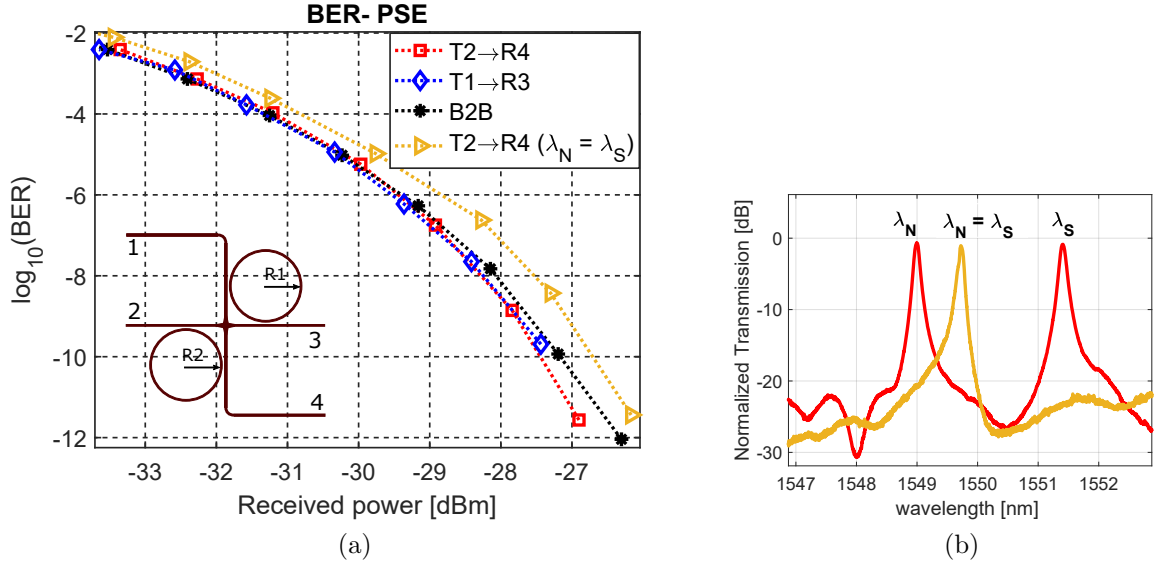
Figure 4.12: BER vs. Received power of PSE (R_1 =20 μm and R_2=19 μm) (a) and static transmissions from port 2 to port 4(b), when $\lambda_N = \lambda_S$ (Yellow) and $\lambda_N \neq \lambda_S$ (Red).

have designed both Type-I and Type-II devices with different radii. A microscope image of the fabricated samples is shown in Fig. 4.13. The measurements have been carried out on the devices that have either 18 or 19 μm of radii, positioned inversely in the circuit. Therefore, the comparison could be possible to made by measuring only one port. As stated earlier, the two devices can be converted into another depending on whether left or right hand sides focusing gratings are used as an input. Another way to do similar work is designing the rings in such a way that their drop port transfer functions can coincide.
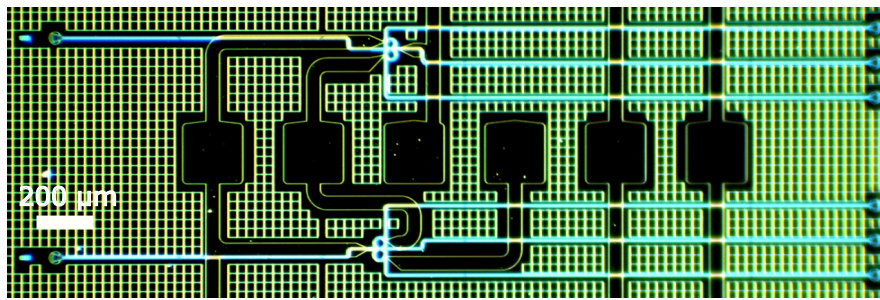
Figure 4.13: Examples of the fabricated SOI Type-I (upper) and Type-II (lower) ICRs.

As shown in Fig. 4.14(a), T1→R2 channel is measured for both devices. They show very similar performance. We have observed that even though the devices are separately measured, B2B results remained the same. Therefore, the presented plot has only one B2B measurement, which is of Type-I, but is also valid Type-II. In the measurements the communication channel is routed by the lower ring R_2 for Type-I and R_1 for Type-II. However, as said before, wavelength dropping paths of ICRs share a common path, which is the vertical waveguide section with a crossing. Therefore, back scatterings induced by the sidewall roughness of the waveguides and bend curvatures

produce resonance modes which can appear at drop port transmission. Figure 4.14(b) shows the normalized static transmissions of drop ports number 2 (blue curve) and 4 (red curve). Some of the dropped resonance peaks have secondary peaks induced by the other ring backscattering.
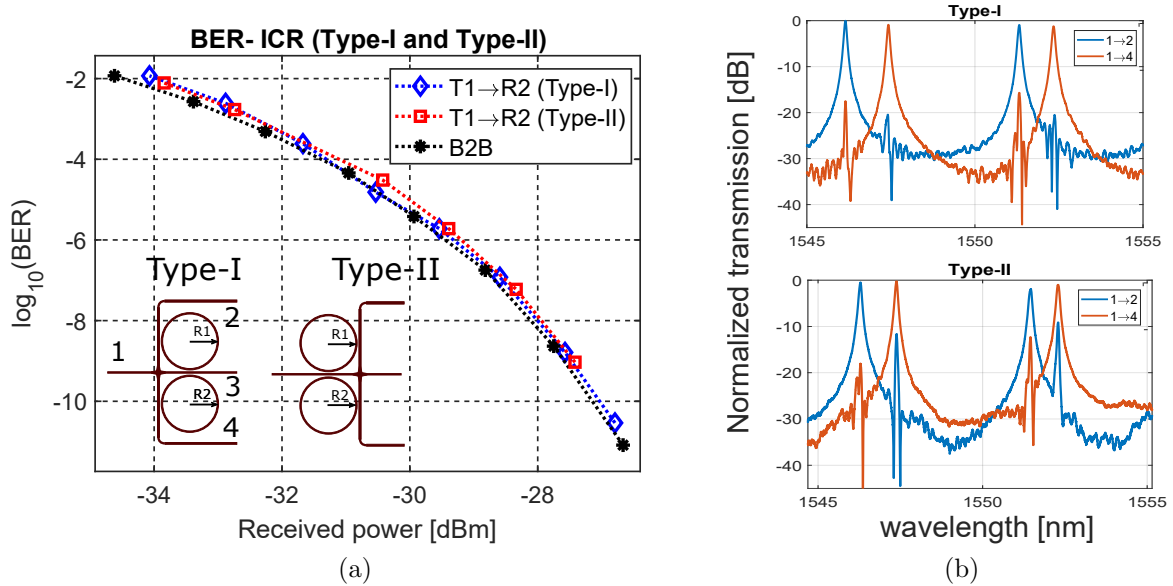
Figure 4.14: BER vs. Received power of Type-I and Type-II ICRs. Type-I ($R_1 = 18$, $R_2 = 19 \ \mu$m) and Type-II ($R_1 = 19$, $R_2 = 18 \ \mu$m) (a) and normalized transmissions of Type-I (upper) and Type-II (lower) (b).

We noticed that power of these spurious resonances can have transmission power just a few dB less than primary peaks. In the presented transmissions spectra, the highest interferometric crosstalk is measured as to be -8 dB near 1552 nm in the Type-II ICR. Regardless of the type of ICR, the backscattering induced resonances appear in the drop ports transmissions due to their topology. Differently, such spurious resonances propagate back to the input port in single ring and PSE resonators. Therefore, from a scalable switching matrix point of view, inter-channel crosstalk in ICRs must be carefully engineered since due to its topology, unexpected resonance modes can limit to construct higher number of nodes in the network.

To evaluate the scalability of the ICR topology, we measured the communication performance of a two-stage 1×4 router that has been designed with Type-I ICRs, as shown in Fig. 4.15. The device, in fact, can implement 2×4 network if the through port is also considered as an input. This configuration allows us to compare the first and the second stage BER results that are relative to each each other. The rings have been designed to have North and South rings with radii of 18 and 19 μm for the first stage and 21 and 20 μm for the second stage of the router. In each measurement rings independently tuned to the communication wavelength.

The characterization results are shown in Fig. 4.16(a). The same color configuration is used to show corresponding transmissions in (b). As in the previous cases, the first stage WDM links T1→R2 and T1→R6 have small penalties together with T1→R3
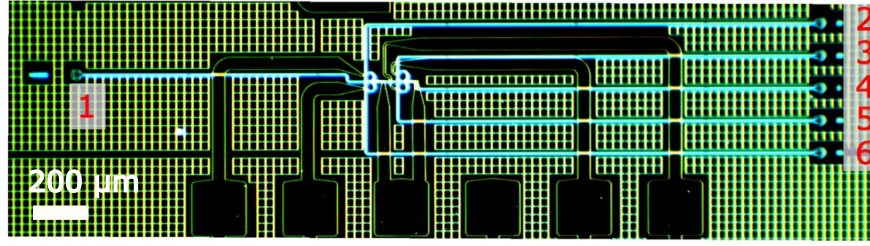
Figure 4.15: A microscope image of the fabricated SOI 1×4 router based on Type-I. Output ports are labelled as 2 and 6 for the first stage drop ports, while 3 and 5 for the second stage drop ports.

communication link, which was performed through the second stage. On the other side, T1→R5 performed a slightly degraded communication such that its penalty at BER $= 10^{-9}$ is measured as 0.4 dB, which can still be neglected compared to measurement errors.
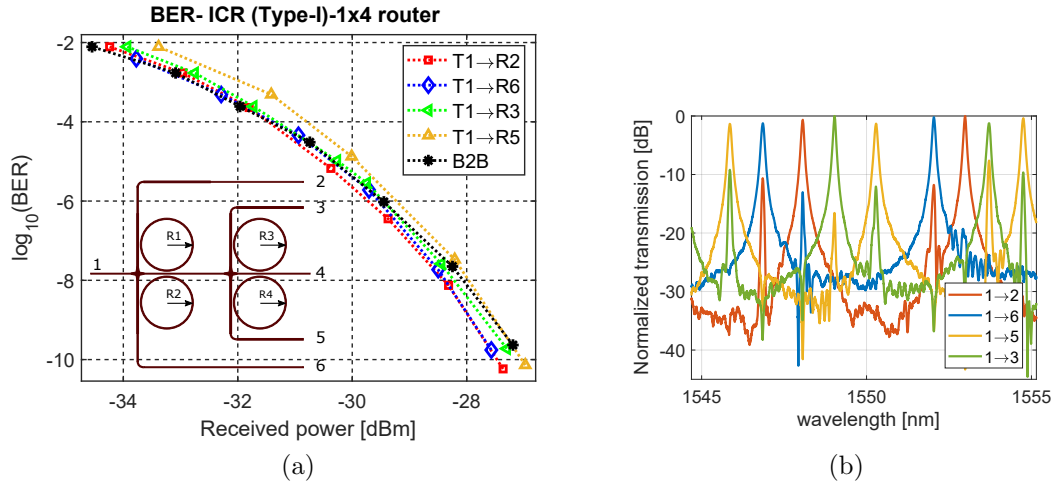
Figure 4.16: BER vs. Received power of 1×4 Type-I ICR router (a) and static transmission of drop ports (b). Rings radii are $R_1 = 18 \ \mu$m, $R_2 = 19 \ \mu$m, $R_3 = 21 \ \mu$m and $R_4 = 20 \ \mu$m.

Before we conclude this section, it is important to emphasize that the devices have been investigated in terms of possible interferometric crosstalk components. The presented BER evaluations depends on the bandwidth of the resonances, since we have introduced three WDM signals modulated at 10 Gbps for measurements in which, two of them were considered as interfering channels set in closest frequency slots to the central wavelength in the DWDM grid (0.4 nm separation). The suppression of the two interfering channels was below -20 dB. Therefore, the system can be considered as a single channel communication by considering possible interferometric crosstalk sources related to Q-factor of the devices. It has been shown that all type of devices perform similarly with minimal power penalties that are comparable to measurement errors, except the PSE performed slightly lower when it needed to process same wavelengths simultaneously. The measured power penalty was 0.8 dB at BER $= 10^{-9}$.

4.6 Experiments on SOI embedded ring resonators for investigation of add/drop filtering processes

In 3.2, an analytical model of a horizontally embedded coupled ring resonators was developed to study the possible use of such resonators to obtained passband profiles by driving the phase difference of the two coupled resonators. According to the model outcomes, the phase difference in the two resonators can alter output characteristics of these devices in such a way that its desired transmission window in the spectrum can be obtained. The aim of this section is to investigate the possible use of embedded rings for drop channel filtering applications that can be useful for flexible optical networks.

Due to the design rule check constraints, which forbid metallization trenches in the circuits pass over waveguide sections, the devices with integrated metal heaters had to be designed in racetrack forms. This condition did not allow to realize circular embedded rings, considering overall footprint of the desired devices. The first two embedded rings have mask layouts of the racetrack of embedded rings with horizontally and vertically coupled inner rings, as illustrated in Fig. 4.17. The horizontally coupled inner cavity bends have 12 μm of radius and its straight waveguide sections are 40 and 14 μm. The outer ring bends have 15 μm radius with 35 and 50 μm long straight sections. The vertically coupled configuration has the identical outer cavity while the inner ring circumference is 10 μm shorter than the horizontally embedded one. We used these design parameters to realize the devices with smallest footprint possible in given conditions according to the allowed fabrication rules. Therefore, the devices in Fig.4.17 are not fully optimized.
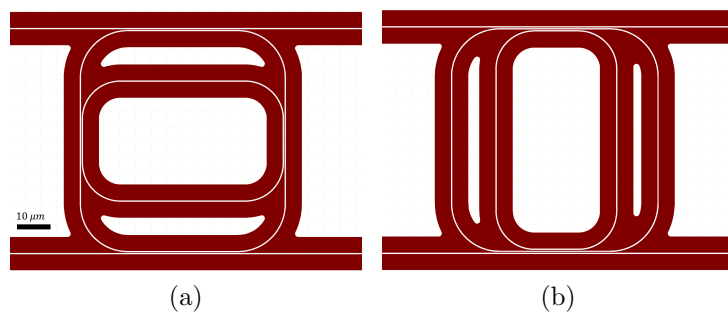
Figure 4.17: Mask layout of the racetrack embedded ring resonators in horizontal (a) and vertical directions (b).

The analytical model was developed for the horizontal configuration. However, the model is valid also for the vertically coupled device. The difference between the two devices is the coupling strength between inner and outer rings. By rotating the inner ring in vertical direction, it is possible to manipulate coupling of outer ring and bus waveguide, but inner ring coupling still exists. Fig. 4.18 shows the measured transfer functions. By these measurements, we tried to stimulate the Case II ($m_1 - m2 =$ odd) number. Phase shifts arrangements are carried out by tuning the inner ring. It can be

seen from (a) that when the applied voltage is 2.1 V, the through port transmission
dips vanish and the device tends to exhibit a transparency window over the C-band.
However, since the measured fluctuation is 7 dB, the device showed poor through port
transmission, without satisfying the expected behaviours as illustrated in Fig. 3.18.
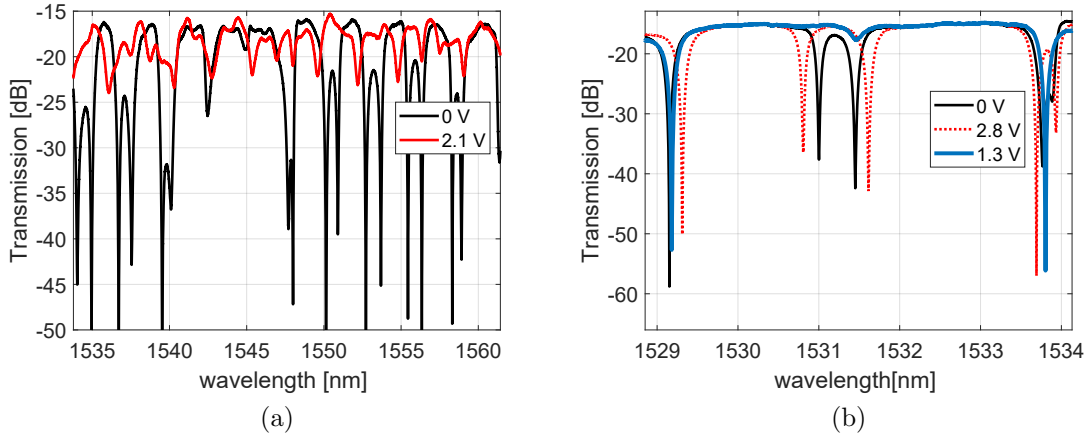
Figure 4.18: Through port transmission spectra of the embedded ring resonators in
horizontal (a) and vertical directions (b).

On the other hand, vertically embedded rings showed better results since they
have different coupling coefficients. Introducing the third waveguide in the horizontal
couplers decreases remaining coupled power in the outer ring. Therefore even though
the both devices are identical in terms of design, vertically coupled embedded rings have
smaller coupling coefficients. When the inner ring is tuned at 1.3 V, the device switches
its operation to Case II. Sharper through port transmission curves also indicate smaller
coupling with respect to horizontally embedded rings. The notches induced by mode
splitting are still observable at 2.8 V. Note that in the theoretical analysis, we analysed
different coupling coefficients to investigate possible transmissions. In practice, we do
not actually change coupling coefficients but tuning resonance wavelength of the inner
ring results in different coupled strength into the outer ring, since the directional coupler
are wavelength dependent. This allow us to manipulate the transmission spectra.
However, we have noticed from these preliminary measurements and outcomes that
embedded ring resonators are difficult to operate the desired function at a desired
wavelength. Therefore, the demonstrated transmissions in (a) was between 1535 to
1560 nm, while the second (b) could be obtained only in the range of 1529 and 1534
nm. Furthermore, as previously shown in the model analysis, very sharp peaks due to
electromagnetically induced transparency (EIT)-like effect can occur when $m_1 - m_2 =$
odd number and the coupling is weak. However, the measured devices did not show
this, since the coupling strengths are higher (the expected power ratios of the bus
waveguides and outer rings were 70% for horizontal and 50% for vertical couplers in
horizontally embedded rings) in the racetrack version of the ring.

Next we investigate two horizontally embedded rings that are cascaded through

the upper bus waveguide, as shown in Figure 4.19. The rings have been designed
to test Case I under a strong coupling condition and to perform bandwidth variable
Add/drop channel filtering, as previously shown in Fig. 3.20. In this configuration,
both devices have the same inner ring circumferences equal to 163 μm. The outer ring
of the second device is 20 μm longer than the first one, which is 221 μm. Bend radii
of both devices are kept the same as 18 and 15 μm for the outer and inner ring bend
sections, respectively. Horizontal and vertical coupling sections are 14 and 16 μm long
respectively. These values were expected to provide strong couplings (> 90%), with 150
nm of gap according to the simulations. Beside the offset length (20 μm) introduced
for the second device, the devices have identical design parameters. The reason of the
use of offset waveguide was to alter FSR of the second devices from the first one. In
this way, drop port spectrums can be compared to each other.
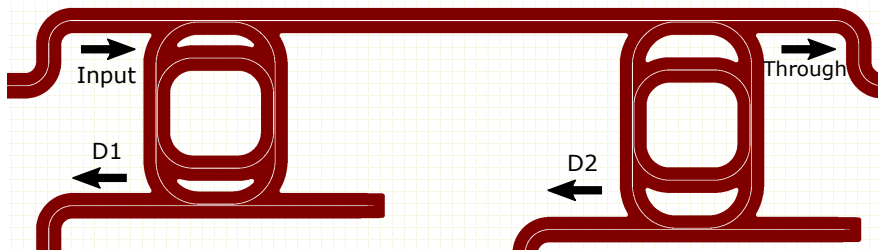
Figure 4.19: Mask layout of two cascaded over-coupled embedded rings.

The transmissions of the output ports are shown in Fig. 4.20(a). Flat-top passbands
of drop ports (P_1 and P_2) spectra confirm strong coupling coefficients. In addition, as
a result of over-coupling, the through port transmission (T) remains below the drop
ports transmission (see Fig. 3.4 for the over-coupling spectra of the single ring). FSR
of P_1 and P_2 3.72 and 3.48 nm, respectively. The measured fluctuations on passbands
between 1540 and 1550 nm are less than 3 dB and FWHM of both curves is ~1.32 nm,
corresponding to ~ 166 GHz. Within the measurement wavelength range the expected
phase shift difference is close to be $m_1 - m_2 =$ even number.

We further investigated possibility of electrically driven thermally induced passband
variations of the first drop port P_1. The obtained shifted resonances by varied applied
voltage which ranges from 0.5 to up to 2.5 V. As shown in Fig. 4.20(b), as the applied
voltage increase, passbands gradually widens and creates also a valley between twin
peaks. This effect can also be seen in the results of the analytical model analysis in Fig.
3.15(a) at 1.55 μm. 3-dB bandwidth of the initial passband is increased from 166 GHz
to 205 GHz, with a insertion loss 2.8 dB of when applied voltage is 2 V and However,
thermal crosstalk between inner and outer rings cause a red shift of the whole band by
0.24 nm.

As mentioned before, even and odd number phase differences can be available only
in a certain wavelength range. Therefore, device can exhibit Case-I and Case-II be-
haviour in a wide range spectrum. It can be said that phase arrangements for a desired
transmission window remain challenging for embedded ring resonators. Limiting ther-
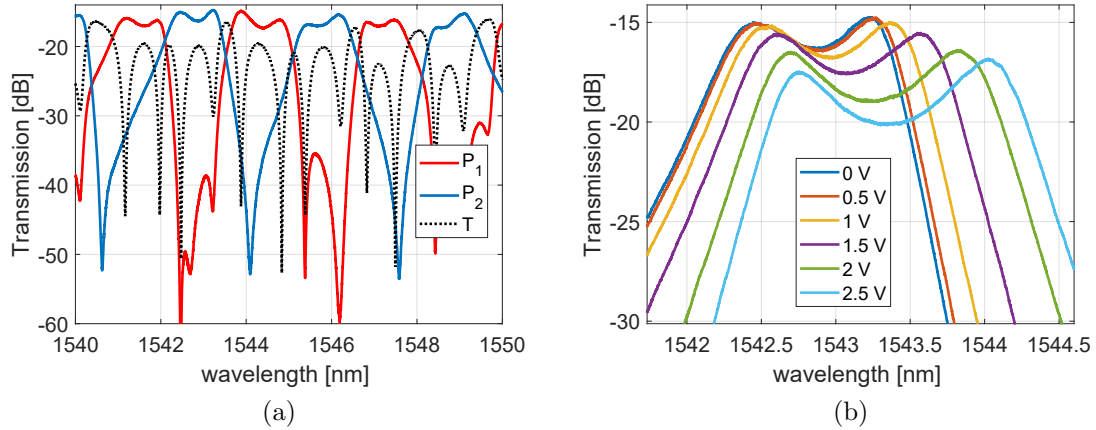
Figure 4.20: Drop port transmissions of the cascaded embedded ring resonators (a) and bandwidth variations according to the applied voltage (b).

mal crosstalk can ease to tune 3-dB Add/drop filtering passbands at the price of an insertion loss.

However, one property of these devices can be beneficial for flexible optical networks. In 4.3, we have proposed the ICR based transponder aggregator architecture. In this architecture, interleavers were used to separate even and odd number of wavelengths at the inputs and outputs of the switching matrix. This process is in fact very critical to implement CDC wavelength operations. Considering the presented results, rings embedded cascaded in such a way that their drop ports transmission share the entire spectrum with wide and flat-top passbands that can be considered as an interleaver.

4.7 Conclusions

In this chapter, we first reviewed the basic switching elements, including single ring and PSE. The routing properties of ICR were introduced. Then, a conceptional bidirectional transponder aggregator based on ICR has been proposed and its working principle was explained. The proposed scheme implements both add and drop functions in a single switch matrix, using the concept of bidirectional communication that can reduce cost of add/drop functions in ROADM systems.

Next, we analysed ICR based wavelength routing matrix in terms of contention free scalable networks for NoC applications. Then we compared the ICR based topology with the conventional PSE based λ-router in terms of number of rings required to construct N×N networks. According to the scalability formulas, ICR can reduce the number of rings in wavelength routing fabrics by a factor of 2 and also can implement 16×16 networks requiring the fewest number of switching element than any other topology reported in the literature.

We characterised networking performances of single, PSE and ICR devices as well as 1×4 ICR router by means of BER evaluation. In general, all types of resonators

performed similarly with minimal power penalties, except the PSE showed slightly degraded performance (0.8 dB penalty) due to the interferometric crosstalk when it was configured to process two wavelengths simultaneously.

Transmission characteristics of horizontally and vertically coupled embedded ring resonators have been reviewed by measurements. According to experiments carried out on the SOI devices, we have found these devices to be challenging to precisely control desired transmission spectra due to non-uniform transmission behaviour in a wide wavelength range. The fabricated resonators performed insufficiently to obtain a proper EIT-like effect in the through port transmission.

However, two over-coupled embedded rings cascaded by a bus waveguide performed wide band (166 GHz) and flat-top drop port transmissions. Bandwidth tuning results implemented by tuning inner ring are presented. The obtained bandwidth enhancement was ~ 40 GHz with 2.8 dB IL. It has been shown that overcoupled embedded rings can be useful for the implementation of an optical interleaver.

Chapter 5

Wavelength selective narrow band optical reflector based on indirectly coupled ring resonators

In the previous chapter, we evaluated functional properties of Type-I and Type-II ICRs for wavelength routing applications where the individual rings are considered to resonate at two different wavelengths. In this chapter, we investigate what happens when the two rings resonate at the same frequency. In particular we will see that phase synchronization, described in section 3.3, makes the device able to reflect the incoming signal with an high Q factor in an highly selective way. Demonstrations of single and multiple wavelengths of the ICR reflectors are provided through the SOI and IMOS devices, respectively.

The work presented in this chapter is largely based on a submitted article: Ali Emre Kaplan, Paolo Bassi and Gaetano Bellanca, "Tunable narrow band optical reflector based on indirectly coupled micro ring resonators," to Optics Express of Optical Society of America (accepted, DOI: 10.1364/OE.389830).

5.1   Introduction

Mirrors realized by MRRs have been previously proposed in the literature for various applications such as laser cavities and sensing, as well as reflective filters in WDM systems [99–111]. Resonator-based reflectors can be implemented by using many different configurations. For example, devices based on two rings [104, 105, 107] or three and even more rings [106] have been proposed. A major drawback of these solutions is that they exhibit multiple reflected wavelengths, spaced according to the device overall FSR. Increasing the FSR to obtain a single working wavelength requires a reduction of the MRR radius, with an immediate fallout in an unacceptable increase of bending loss attenuation. To tackle this issue, cascaded ring resonators have been proposed to enhance the FSR and pass band flatness without suffering from the reduced radius [112–114]

issues (see [30] for more examples). Coupled resonators could benefit of the vernier effect, which increases the wavelength tuning range (e.g. as end mirrors in laser applications [103, 110, 115]). Other approaches for realizing single wavelength reflectors combine a Y-branch splitter with an embedded microring/microdisk [102, 109] or sidewall Bragg grating assisted ring and racetrack resonators [108, 111]. The main problem with these approaches, though interesting results have been recently presented [116], is related to the footprint: indeed, a very high number of periods is needed to guarantee high reflection. Moreover, precise fabrication of these gratings requires a high quality lithography process.

Previously reported double ring based reflectors use directly coupled rings. They exhibit reflections in presence of resonance mode splitting induced by coupling between the clockwise (CW) and counter clockwise (CCW) propagation modes. However, mode splitting for wavelength reflection occurs only in specific coupling conditions, especially when coupling between cavities is weak [105]. This requires an additional design effort to precisely determine the cavity-to-cavity coupling coefficients. Moreover, fabrication issues such as sidewall roughness, which may produce strong reflections that propagate back to input port [117], can harshly influence the performance of the device.

On the other hand, the ICRs can offer a single reflection condition, which depends on the phase shift difference between two resonators. The other design parameters such as coupling strengths, which are in common with the other type of ring reflectors, should be optimized only to enhance the reflected power.

In the following, we will investigate the reflection properties of the device and provide the optimal design parameters to evaluate the reflection performance and experimentally demonstrate that, by a suitable tailoring the resonant wavelength shifts imposed via integrated metal heaters on chip, it is possible to make ICR to exhibit reflection.

5.2   Working principle of ICR reflector

Figure 5.1 illustrates different working regimes supported by the Type-I ICR. As explained in the previous chapter, when the rings resonate at different frequencies, the device acts as a router. and the resonant wavelengths are dropped by the rings and driven to the respective output ports, as shown in Fig. 5.1(a). However, when the rings are synchronized the light is readdressed back to the input port, thus giving rise to reflection (as shown by the dotted-red path in Fig. 5.1(b)). In this case the rings have, at the wavelength corresponding to the shared resonance, the same optical lengths. As shown 3.3, this implies $\theta_1 = \theta_2$, being $\theta_1 = n_{eff1}L_1$ and $\theta_2 = n_{eff2}L_2$, where n_{eff_i} and L_i are the effective refractive index of the mode and the circumference of each ring, respectively.

The phase shift synchronization can be obtained by fabricating rings with the same
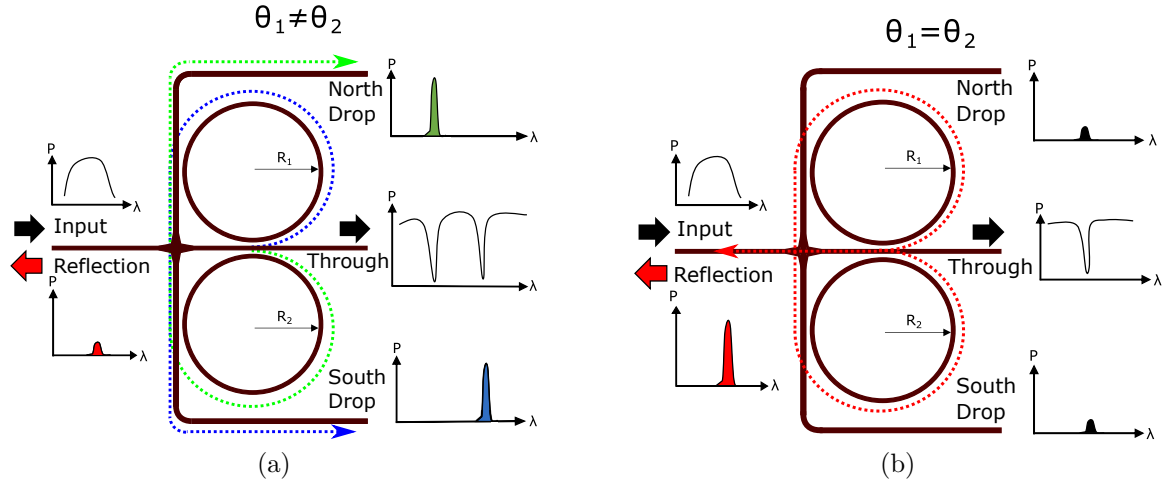
Figure 5.1: Working principle of the ICR when used (a) as a router, in the case of phase shift ($\theta_1 \neq \theta_2$ for all the ring resonances) and as a reflector (b) when $\theta_1 = \theta_2$ at the common resonance of the two rings.

radii or, in case of different rings, through thermo-optical tuning. In the former case, all the resonances are synchronized and a comb-type reflected spectrum, i.e. a spectrum where many peaks are present, results. Reflected wavelengths are spaced depending on the FSR of the rings, with peaks not equally spaced due to effective index dispersion. In the latter case, two close resonances can be superimposed by shifting one to coincide with the other, and a single reflected wavelength is then obtained.

Thermal tuning can also be used to shift the operating wavelength of the device by heating both rings, in order to adjust the reflected wavelength to the desired value, or to reconfigure it as a router avoiding any superimposition of the resonances, as it will be explained in the next section of the chapter.

We first present experimental results of single wavelength reflection on the SOI reflector, which has different rings. Then we will investigate the reflection spectra obtained by the identical rings fabricated with the IMOS technology.

A microscope image of the characterized SOI ICR is shown in Fig. 5.2. Since rings are different, the synchronous resonances at the desired wavelength must be configured by thermal tuning. During this operation, because of the proximity of the rings, thermal crosstalk is possible and an undesired drift of the resonance could be observed. To overcome these effects, approaches such as thermal crosstalk cancellation described in [118] should be applied.

5.3 Experimental results of SOI Ring Reflector

The experimental setup used to characterize the fabricated devices is illustrated in Fig. 5.3. It is similar to the setup described in Fig. 2.4, except the reflection spectrum is retrieved from the input port using a circulator. In this way, the input and reflected signals can be independently measured. The integrated heaters used for resonance
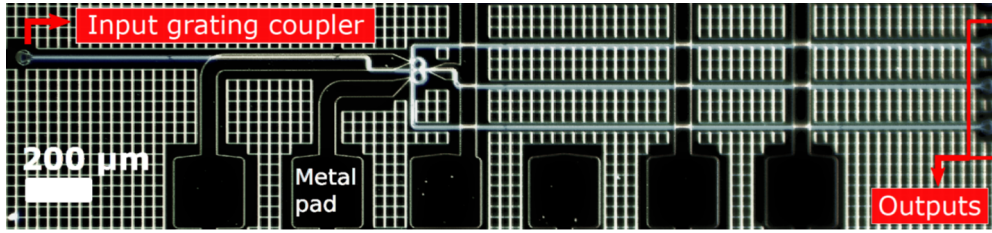
Figure 5.2: Microscope image of the fabricated SOI reflectors with metal deposition for micro heaters and probe pads.

tuning are driven by a suitable power supply. The resistance of each integrated heater is ~14 Ω and depends mainly by the length of the titanium strip covering the ring.
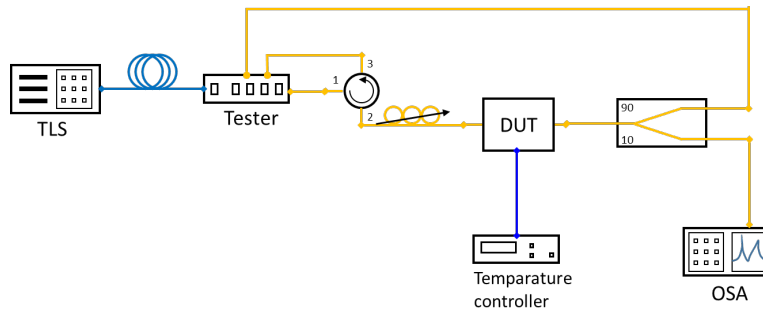
Figure 5.3: Experimental setup for reflection and transmission measurements.

Figure 5.4 shows the wavelength shift according to the power applied to the resistor on the ring. The calculated tuning efficiency obtained from the slope of the linear fit was found to be 115 pm/mW. The resonators have FSR of 5.04 and 4.76 nm for the radii of 18 and 19 μm, respectively. Therefore, the maximum required power to tune the reflected wavelength within the FSR is below 45 mW.
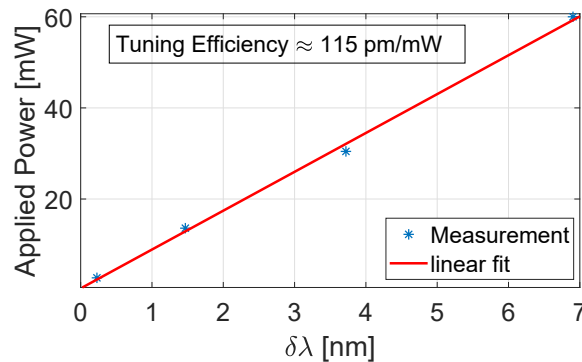
Figure 5.4: Measured resonance wavelength shift in ICR with respect to the applied power.

The experimental results of the drop and through ports when the electrodes are not polarized are shown in Fig. 5.5(b). In the following, we will refer to this configuration as the OFF state. When no voltage is applied to the electrodes, all the resonances are phase-unmatched and separated in the considered wavelength range. As shown in Fig. 5.5(b), the two dropped wavelengths near 1540 and 1542 nm have $Q = 17,500$ and

10 GHz of bandwidth. The North and South drop ports both show weaker secondary resonance wavelength peaks driven by the other ring. This is caused by back scattered signals induced by the sidewall roughness of the waveguides, which are not considered in the analytical model. These signals, in fact, induce counter propagating modes which appear in the spectrum of each drop.

Such resonances occur at the wavelengths where the model predicts coupling effects between the rings. Without backscattering, such effects would be a further decrease of the signal at the drop output. With backscattering, on the contrary, some undesired signal is present in the channel. It however adds in spectral positions where the signal level is much lower, being then less harmful for the device performance. As said before, differently from the previously reported configurations based on side-by-side coupled double rings, the coupling of these modes is not required for the reflection condition. The ICR in fact, thanks to its topology, performs reflections using mutually shared light paths for re-routing the dropped wavelengths back to the input port.
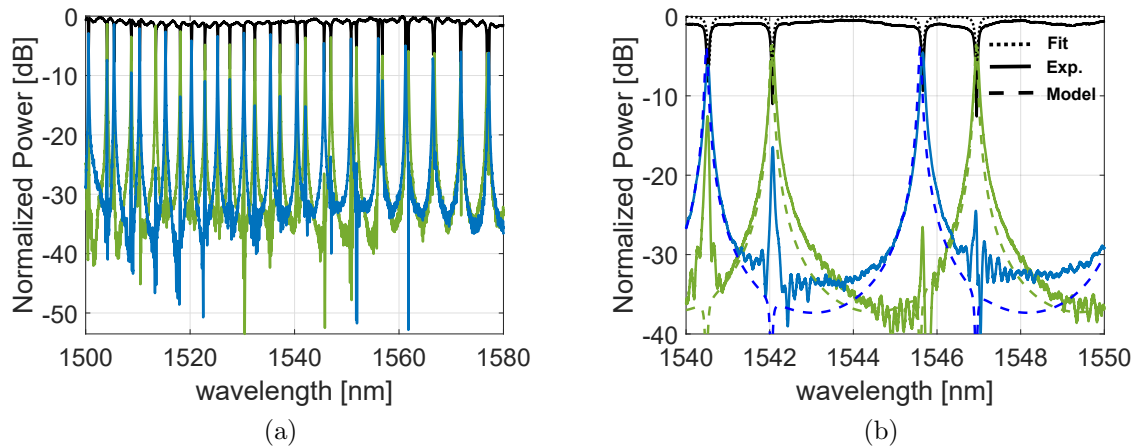
Figure 5.5: (a) Measured transmission spectra of Through (Black), North drop (Green) and South drop (Blue) ports in the OFF state (no applied voltage to the electrodes); (b) enlarged view in the $1540 \div 1550$ nm wavelength range. In this figure, the dotted Black curve is the fit, with the analytical model, of the Through port. In the same plot, the calculated drop outputs are also illustrated (dashed curves). In this situation, all the resonances in the considered portion of the spectrum are asynchronous, and therefore separated.

In order to compare the model outputs with the experimental results, we first extracted the technological parameters, such as group index, coupling and loss coefficients, by fitting our model to the measurements in the OFF state. The fitting plot of the through port is the dotted Black curve of Fig. 5.5(b). The parameters extracted from this fit are reported in Table 5.1. The fitted loss coefficients α_1 and α_2 are in good agreement with the expected propagation losses in the cavity, considering 3 dB/cm waveguide loss. The curves of the North (dashed Green) and South (dashed Blue) drop ports obtained through the transfer matrix model using the parameters obtained from the fitting are also plotted in Fig. 5.5(b). The same fitted parame-

ng	$\partial n_{eff}/\partial \lambda$	R_1	R_2	k_1	k_2	k_3	α_1	α_2
4.08	$1.046 \cdot 10^6$	18.02	19.01	0.232	0.236	0.182	0.986	0.987

Table 5.1: The extracted parameters obtained by fitting the parameters of the model
with experimental results.

ters have been also used in the analytical model to reproduce device responses when
the resonators are synchronized (ON state) for the common resonance. In this case,
thermally induced effective index change is introduced in the model.

To configure the device as a reflector, i.e. to turn it from the OFF to the ON
state, 1.7 V have been applied to the electrodes of the North ring. This causes a
shift of 1.7 nm on the peak of E_{p4}, which now superimposes to the peak of E_{p2} for
$\lambda \simeq 1547$ nm. The power required for this shift is about 14 mW. As seen in Fig. 5.6(b),
in this situation the power of the dropped wavelength is reduced to about -10 dB and
the power reduction compared to the OFF state is close to 5 dB. Furthermore, the ER
of E_{p3} increased up to 22 dB, with a difference of ΔER = 11 dB with respect to the
non synchronized case.
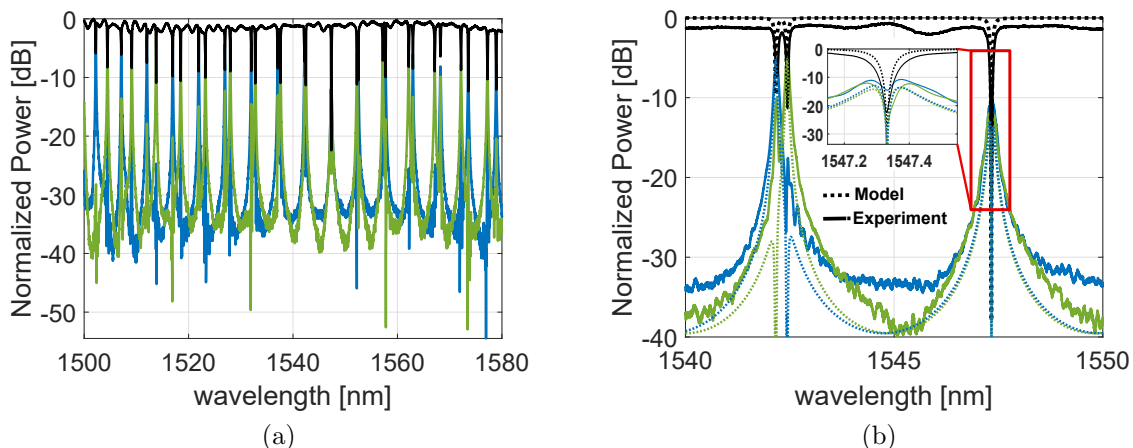
Figure 5.6: (a) Measured transmission spectra of Through (Black), North drop (Green)
and South drop (Blue) ports with an applied voltage of 1.7 V to the North ring; (b)
enlarged view in the 1540 ÷ 1550 nm wavelength range. As it can be noticed, the phase
synchronization is present for $\lambda \simeq 1547$ nm

The measured spectra of E_1^- (reflection) and E_{p3} (through) are shown in Fig. 5.7(a).
When the rings are tuned to have a common resonance at $\lambda \simeq 1547$ nm, a very narrow
band reflection peak ($Q \approx 30,000$) with 50 pm (6.4 GHz) of linewidth and 11 dB of
ER becomes maximized at the resonance ($\lambda \simeq 1547$ nm). The measured reflection to
transmission ratio is found to be 0.96 (linear scale). As seen in Fig. 5.7(b), a secondary
peak 9.87 nm on the right from the main resonance appears. This secondary peak has
an intensity 2 dB below the intensity of the main peak.

This undesired peak occurs because of the proximity of two non-degenerate resonant
modes. The suppression of side modes gets higher when resonances are more separated

in wavelength. We also found from the model results that reflection port suppression depends on Q-factor: the higher the Q factor, the higher the side mode suppression.

(a)

(b)
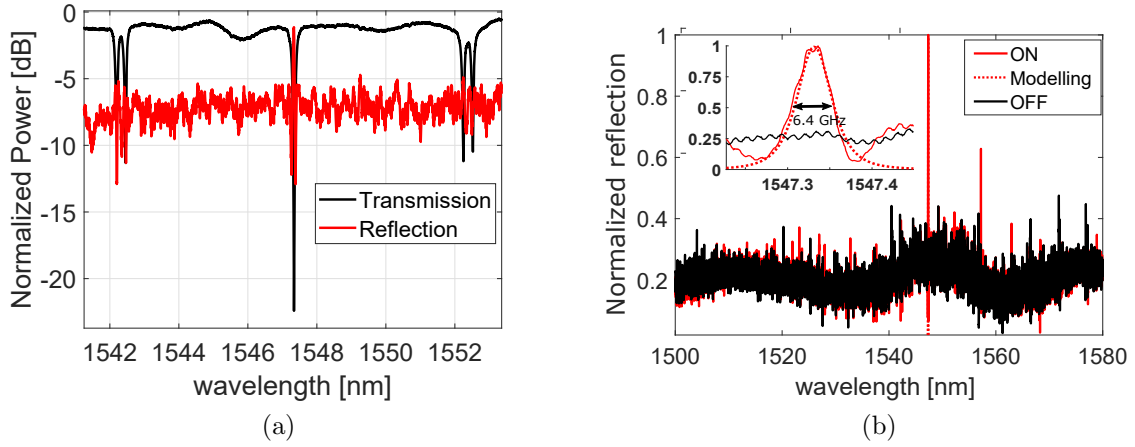
Figure 5.7: Transmission and reflection as a function of the wavelength when the device is in the ON state (a). Comparison of the measured reflection spectra in the OFF (Black curve) and ON (Red curve) states (b). The enlarged view shows the spectra in the region of the peak comparing also measurements with simulated results (Red dotted curve) for $\lambda \simeq 1547\,\mathrm{nm}$.

Evaluation of the actual reflectivity by comparing the ratio between reflected and the transmitted signals is not straightforward. In fact, thermal tuning for phase alignment is sensitive to measurement errors and the maximum reflection is achievable in a very small wavelength range. Moreover, other contributions to the reflection such as fiber to waveguide coupling, back scattering and Fabry-Pérot oscillations between input and output gratings, result in a reflection floor distributed over the spectrum even in the OFF state, as shown in Fig. 5.7(b). Since the measurements of ON and OFF states can have different reflection floors, we calculated the reflectivity by measuring the reflection enhancement with respect to the floor level at the wavelength of the resonance. As a result, each reflection peak is investigated with its own reflection floor and the difference is considered as the actual reflectivity coefficient.

The reflector has been tested in the wavelength range of 1520 - 1560 nm by applying suitable polarization voltages to the integrated heaters in order to tune the reflection, i.e. in order to superimpose two ring resonances, at the desired wavelength. Fig. 5.8 shows the measured reflectivity over a span of 37 nm. The maximum measured value is found to be 0.63 (linear scale), similar to the predicted value of 0.68 obtained from the model using the fitted parameters. The measured reflectivity has an average value of 0.55 in the considered wavelength span and the maximum oscillation of about 15%. The change in the measured reflectivity, which was not foreseen in the analytical model, is due to the dependence on the wavelength of the coupling coefficients of the couplers. Since the horizontal and the vertical couplers are different, their ratio changes when tuning the device and therefore also the reflectivity, as shown in the reflection plot of Fig. 3.24.
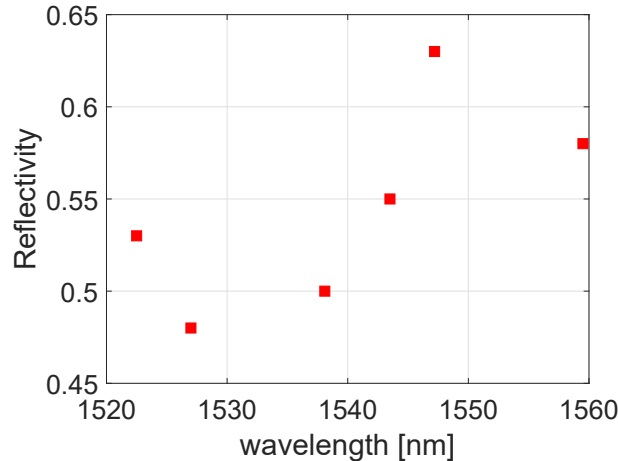
Figure 5.8: Measured reflectivity as a function of the wavelength obtained through thermal-tuning.

In order to have a uniform reflections in the tested wavelength range, the difference between the cavity lengths should be reduced. However, in this case, the identical radii will increase the strength of the side mode reflections and eventually lead to a periodic comb reflection spectrum, since more resonances could be simultaneously phase synchronized. Using different radii, for example 18 and 19 μm, allows to restrict the number of simultaneous resonances to a single one at a fixed wavelength.

As stated earlier, higher reflectivity and side mode suppression require low losses in the cavity. According to simulations, a propagation loss of 1 dB/cm in the rings, neglecting the bend loss, would be sufficient to achieve a reflectivity higher than 0.9 and to improve side mode suppression up to 10 dB.

Wavelength dependence of other important quantities such as ER and FWHM of the reflection peaks are shown in Fig. 5.9(a). The linewidth of reflected resonances varies from 40 to 52 pm while the ER range is between 6.65 and 11 dB. Since the propagation losses in bend sections can be minimized by increasing the radius, the preliminary study on the coupling coefficient takes an important role for the critical coupling condition to achieve narrow linewidth reflection spectra.

Fig. 5.9(b) shows the measured ER in the ON state (synchronous rings at the resonance) and its increase ΔER compared with respect to the OFF state (asynchronous rings at the resonance). The maximum observed ER is near a wavelength of 1560 nm, where the ΔER $= 29$ dB.

From this plot it is possible to observe that, even though the reflection condition requires a high ER in through port transmission, reflectivity strength and ER can be uncorrelated. In fact, as it can be noticed from the plots in the first row of Fig. 3.24, there is no correspondence between high reflection and high ER. Moreover, regardless the phase matching condition is satisfied (bottom row in the same figure), the through port always presents a high ER region depending on the coupling ratio of the horizontal and vertical couplers. As an example, by considering the asynchronous case ($\theta_1 \neq \theta_2$)
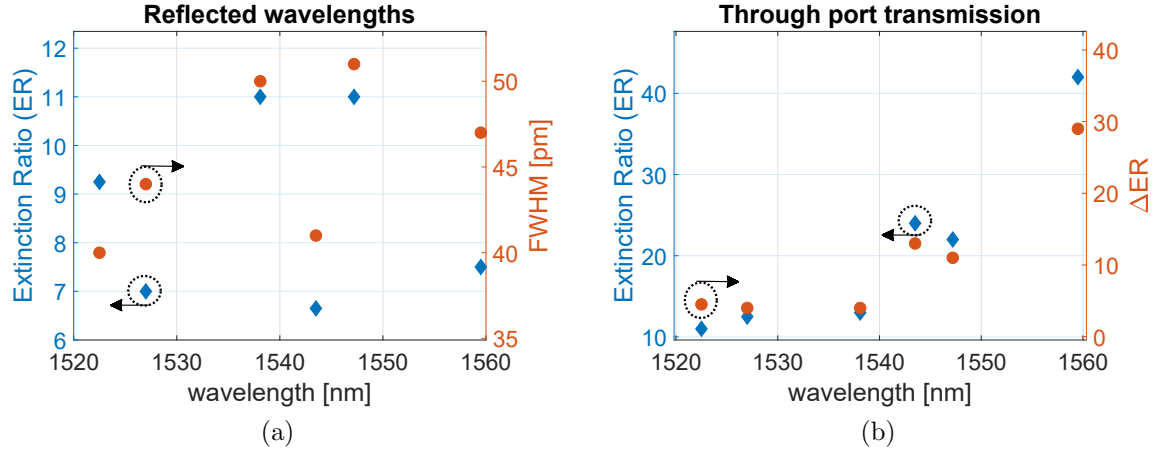
Figure 5.9: (a) Measured ER and FWHM of the reflected peaks as a function of the wavelength while tuning the common resonance of the two rings through the heaters; (b) measured ER of the through port transmissions with its enhancement ΔER compared to OFF state.

Reference	Device Type	Material	Reflectivity	FWHM (pm)
[107]	Directly coupled double MRRs[†]	Polymer	0.23	120
[108]	Grating assisted single MRR[‡]	Si_3N_4	0.92	400
[109]	Single microdisk resonator [‡]	Silicon	N/A	17
[110]	Directly coupled double MRRs[†]	Silicon	0.7*	160
[111]	Grating assisted racetrack resonator [‡]	Silicon	0.74**	147
This thesis	Indirectly coupled double MRRs [†]	Silicon	0.63	51

‡: not tunable, †: tunable, *: estimated, **: simulated

Table 5.2: Comparison of experimental demonstrations of ring based reflectors.

with the values of $K_h/K_v = 2$ and a loss coefficient $\alpha \approx 0.95$, it is still possible to obtain the highest ER achievable and keep the reflection power to less than -15 dB.

Comparisons among previously reported ring based reflectors [107–111] and the device proposed in this work are shown in Table 5.2. Only the experimental works are included in the list. While the grating assisted resonators show higher reflectivity [108, 111] our device, together with the reflector in [109], produces much narrower reflection bandwidth. Unfortunately, the results reported in [109] do not provide the reflectivity value. That device is a different implementation of the one originally fabricated in Polymer [102] (not in the list because of lack of information on both reflectivity and FWHM), where the ring is substituted by a microdisk. The reflectors in [107] and [110] are made by two rings that are side by side coupled to each other. While the former was fabricated in Polymer, the latter was made of silicon and used as an external cavity to realize a tunable laser. As said before, the working principle of these mirrors is based on counter propagating modes coupling. The devices presented in [109] and [111] combine a resonator with two Y-branch splitters that connect the input and output ports to implement Mach-Zehnder interferometer, where the branches of such interferometer are coupled to a resonator as in add/drop configuration.

All reflectors listed in Table 5.2 use MRRs in either all-pass or add/drop configurations while ICR uses a cross-grid configuration.

In this section, we experimentally demonstrated that ICRs with the rings that have different radii can provide very narrow tunable single wavelength reflection. In the next section we provide the results of multiple wavelength reflection measurements obtained from racetrack version of ICR fabricated in the IMOS technology.

5.4   Multiple-wavelength reflection implemented by a racetrack ICR fabricated in IMOS

According to the theory, an ICR with identical resonators can generate multiple reflections as a comb-like spectrum as a result of fully synchronized resonators in terms of symmetric coupling coefficients, dispersion and loss. To test this statement, ICR reflectors with identical rings have been designed and fabricated via IMOS MPW run at the Eindhoven University of Technology, together with the characterized directional couplers described in section 2.2. A Scanning Electron Microscope (SEM) image of a racetrack Type-I ICR is shown in Fig. 5.10. Each ring has 15 μm curvatures that are connected by 1 μm and 5 μm long straight waveguides, which are coupled to bus waveguide via 3×3 and 2×2 couplers, respectively. The couplers have 100 nm of gap and the waveguides are polarized by quasi-TE mode.
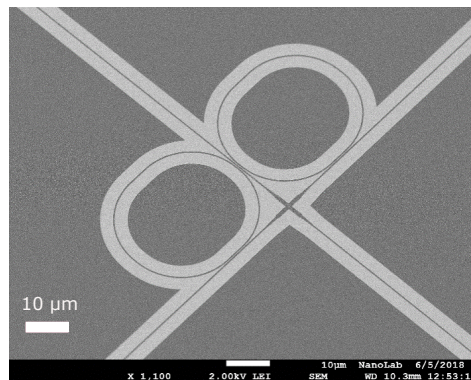
Figure 5.10: A SEM image (by NanoLab@TU/e) of an ICR fabricated in IMOS.

The devices have integrated heaters, but unfortunately thermal tuning for reflection measurements have not been carried out yet. Therefore, we can present transfer functions obtained by keeping the chip temperature at 24 °C. Results shown in Fig. 5.11(b) can only provide a proof-of-concept demonstration. Perfect matching can in fact achieved only tuning the device because of unavoidable fabrication tolerances. The reflected peak near 1508.5 nm (b) has ~0.77 (linear scale) transmission/reflection ratio and Q-factor of ~11,000. However, non perfect symmetry of the transfer function plots allow to deduce that these results could be improved using thermal tuning.

The normalized multiple resonance peaks with ~5.72 nm of FSR are shown in Fig. 5.12. Due to focusing grating coupler response, a group of 8 reflections have a comb-like
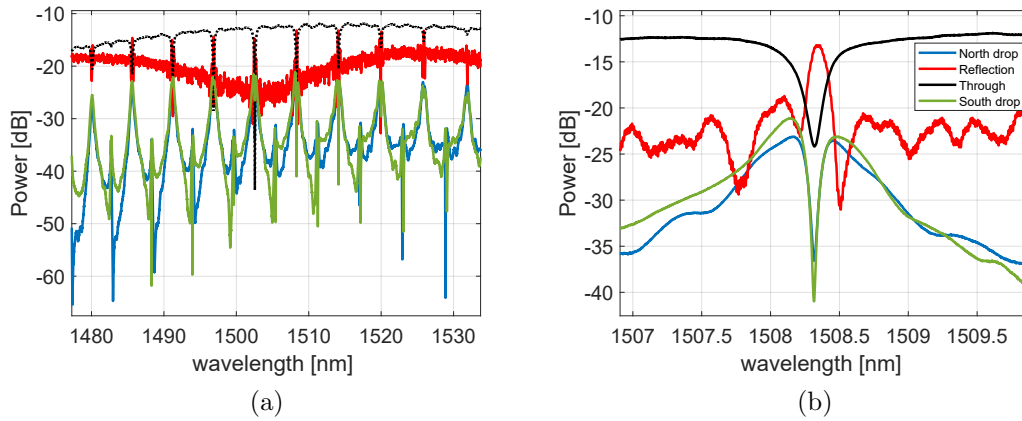
Figure 5.11: Transmissions of the measured drop, through and reflection (a) and zoom view at 1508.5 nm (b).

spectrum between 1490 and 1525 nm. Depending on reflection floor, the peaks have different power levels with a maximum variation is 1.84 dB.
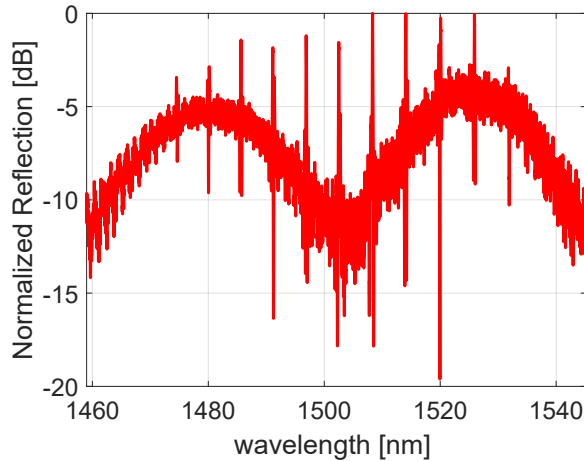
Figure 5.12: Normalized reflection spectrum of IMOS ICR.

A rough guess of the reflectivity can be made, considering the peak magnitude and comparing it to the corresponding reflection floor. For instance, at 1500.2 nm one finds a 7.16 dB of difference between maximum of the peak and its reflection floor, which corresponds to a reflectivity of 0.8. Despite this is a non optimal operating condition, the reflectivity is anyway much higher than that achieved in SOI devices. This is a good starting point to make performance comparison of ICR reflectors, considering single and multiple wavelength reflection conditions.

5.5 Conclusions

In this chapter, Type-I ICR has been investigated as a highly frequency selective optical mirror. An ICR device that has the rings with different radii can be configured through thermal tuning to obtain a single narrow-band selective mirror. On the contrary, if rings

with same radii are considered, multiple reflections and a comb-like reflection pattern can be obtained. Both SOI and IMOS devices have been designed, fabricated and measured.

The SOI ones have been extensively characterized. For these devices, the tuned reflections (FWHM < 55 pm) in a 37 nm wavelength range showed $Q \approx 30,000$ and an average reflection coefficient of 0.55. The reflection strength was found to be sensitive to round trip propagation losses. However, as the analytical model suggests, higher reflectivity can be obtained by improving the fabrication quality. For IMOS devices, though characterization was not so extensive, preliminary results showed that a much better reflectivity can be expected.

The design considerations allowing to achieve a single wavelength reflection with high side mode suppression have been addressed. Unlike conventional directly coupled ring based reflectors, which require the backward coupling of counter propagation modes, the ICR topology uses forward propagation and needs only phase shift alignment of the resonators to achieve reflection condition.

As foreseen from the analytical model of the ICR, identical rings can impose a condition that the reflection spectra of Type-I can perform multiple wavelength reflections. This condition has been experimentally demonstrated by the racetrack ICRs fabricated in IMOS technology. A set of eight reflection peaks spaced by 5.72 nm in the wavelength spectrum had around 11,000 Q-factor and 1.84 dB peak power variation in a wavelength range of 1490 and 1525 nm. The maximum measured transmission/ reflection ratio was 0.77 (linear scale). Due to the lack of thermal-optic tuning measurements, the reflectivity of the fabricated IMOS ICR has been estimated using the reflection floor where the actual reflections were measured and found be 0.80. This value, however, can be reasonably increased if the perfect match between the two rings can be obtained.

The ICRs driven in simultaneous resonance condition can offer more precisely tuned reflected wavelength and can be an alternative device to Distributed Bragg gratings and photonic crystals for the use of an external reflective cavity as well as an internal cavity in the integration platforms that use active materials for single wavelength laser applications, sensing schemes as well as feedback systems in scalable ring based switching architectures.

Chapter 6

Theoretical study of a differential optical sensing scheme

In this chapter, we introduce a proof of concept of a differential optical sensing scheme for biosensing applications. The aim of this study is to provide an on-chip thermal calibration method and to theoretically compare sensing performance of the presented scheme with a single ring micro resonator through a case study.

The content of this chapter is largely transcribed from the conference paper : Ali Emre Kaplan, Gaetano Bellanca and Paolo Bassi, "Differential Optical Sensing through Coupled Micro Ring Resonators," The Thirteenth International Conference on Quantum, Nano/Bio, and Micro Technologies ICQNM, October 27- 31, 2019 - Nice, France.

6.1   Introduction

Integration of microfluidics with PICs promotes new emerging biosensing applications. So far, various types of on-chip Si PICs, such as MRR, Mach–Zehnder interferometer, photonic crystal and Bragg grating have been investigated for label-free detection [119]. Among them, MRR based sensors provide higher sensitivity and denser integration [120]. The add-drop configuration of MRR allows a sensing application that measures the resonance wavelength shift according to upper cladding index change induced by microfluids [121]. Figure 6.1 illustrates a schematic view a ring based biosensing platform. A suitable measurement setup for this scheme consists of a tunable laser source (TLS) that provides the incoming light, a splitter that connects output signals to a spectrum analyser for signal monitoring during measurements and to a tester that has a photodetector array for read-out process. A computer controls both TLS and tester for wavelength tuning and collects the measured data via the tester.

The characterization of wavelength interrogation is based on the extraction of refractive index change via resonant wavelength shifts induced by the interaction of fluids and the evanescent field of a resonant cavity. The amount of the wavelength shift depends on how much the analyte flow alters the effective refractive index. Such a shift
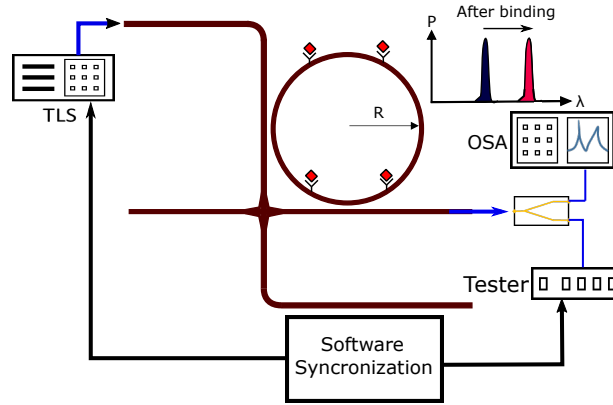
Figure 6.1: Schematic view of a micro ring resonator based biosensing scheme: The index change in the resonator can be either by analyte binding (as in this example) or analyte concentration change in the microfluid flow.

can be formulated as [122]

$$\Delta\lambda = \frac{\Delta n_{clad}\lambda_{res}}{n_g} \tag{6.1}$$

where Δn_{clad} is the refractive index change of the cladding induced by the interaction of the fluids and the ring resonator. This interaction can occur either by analyte binding or concentration change of substances and the types of sensing are then called label-free and bulk sensing, respectively. A MRR with high Q-factor is desirable for enhanced detection limit of sensing applications. However, environmental and microfluidics induced thermal perturbations must be considered since such spurious effects may significantly affect wavelength shift at high Q-factor. Previously, a sensing scheme based on cascaded MRRs has been investigated using shared flow channel above the reference and sensing rings where two solutions flow independently [123]. However, it was found difficult to control precisely the temperature and pressure of each solution. Another approach uses two frequency locked laser sources for imprinting the temperature difference of the rings in radio-frequency domain and achieves the state of the art sensitivity in the order of 10^{-8} RIU (Refractive Index Unit) [124]. Unfortunately, this method still suffers from lack of thermal equilibrium of the sensor and requires more than one laser source. The previously reported differential sensing platforms with thermal compensation perform only wavelength interrogation, which relates the induced index change to resonance shifts in the spectrum. Here, we propose an alternative scheme based on ICR that is able to also support the intensity interrogation, which considers change in optical power. This property also can help to eliminate the need of external thermal stabilization systems and a reference fluid flow.

The schematic view of the ICR based sensor is depicted in Fig. 6.2. It is assumed that the rings are identical and the induced effective index change occurs in one of the rings, while the other ring is used as reference. Since the overall output transmission depends only on the phase difference between sensing and reference resonator, we refer

to this scheme as a differential sensing scheme.
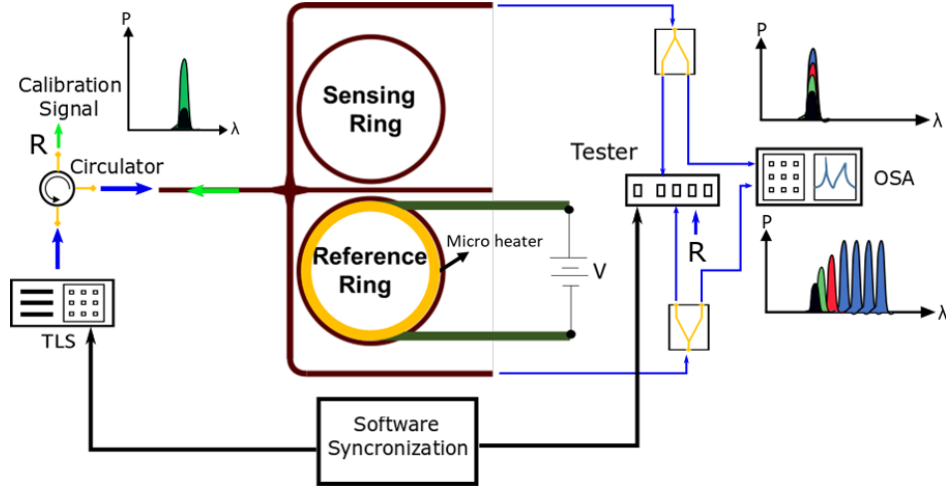
Figure 6.2: Schematic view of a ICR based differential sensing scheme: prior to measurement process, ICR is set in reflection condition by tuning reference ring via integrated heater. TLS and tester provide continuous transmission measurements. Once the calibration signal is obtained via circulator, measurement process begins. The microfluid induced index change in the sensing ring puts the device in routing condition (phase mismatch) and two separated resonances at North and South drop ports are measured by a tester. The sensing signal shift in the South drop spectrum (lower inset) is read relative to the fixed reference signal in the North drop port spectrum (upper inset).

The basic principles of the measurement can be described as it follows: prior to initiate the actual measurement, the device is set in the reflection condition by tuning reference ring via its integrated heater. Phase alignments can be done by monitoring the sensing and reference signals by OSA. This process allows to calibrate the sensor for different ambient temperature conditions, therefore provides on-chip thermal stabilisation. Once the calibration signal (reflection) is maximized, i.e. the two resonators are synchronized, and therefore drop ports have transmission dips, the microfluid initiates to flow over the sensing ring and system begins performing spectral measurement through the TLS signals. Resonance shifts in the sensing ring spectrum due to refractive index change induced by the fluids flow on the sensing ring and the reference signals are then obtained by the tester. Finally, the extracted data is obtained from the resonance shifts of the sensing signal relative to the reference ones. As shown in the insets of Fig. 6.2, reference signals remain at the same wavelength, while sensing wavelengths experience red shift and also intensity change till a certain point which will be explained later.

It can be noticed that, the response of ICR to operation condition change (from reflection to routing) causes a rapid change in transmission, as transition from a transmission dip to a peak, depending on the index change. Therefore, as shown in the lower inset of Fig. 6.2, the sensing signals experience, in additional to resonance shifts, transmission enhancements (represented by the different colours in the lower inset).

This is not the case for single MRR, because its resonance transmission ideally remains constant. Power enhancement at the sensing ring drop port saturates at a certain wavelength and after this point it performs only wavelength shifts as in single ring case. This property is what we refer to as intensity interrogation. In this case power enhancements are used to relate the induced index change. In the following, we will illustrate these two approaches through a theoretical case study, by using identical design parameters for both single and ICR structures in their analytical models presented in chapter 3.

6.2 Figures of merit

In order to evaluate pros and cons of the presented scheme over the single ring one, we first need to calculate its sensitivity using the following parameter [125]:

$$S = \frac{\Delta\lambda}{\Delta n_{clad}} \tag{6.2}$$

As we analyse the device theoretically, it is convenient to use the effective refractive index Δn_{eff} instead of the Δn_{clad} because the rings are identical in both single and ICR ring schemes. The minimum detectable change of the n_{neff} determines the Limit of Detection (LOD), which corresponds also to the minimum wavelength shift $\Delta\lambda$. Since this sensing scheme requires a spectrum analysis, minimum detection depends on the setup. To eliminate setup dependency of the measurements, an intrinsic LOD ($iLOD$) can be defined as [125]:

$$iLOD = \frac{FWHM}{S} \tag{6.3}$$

meaning that the FWHM of the resonance peak is the lower limit of the wavelength shift needed to distinguish two successive wavelengths. S and $iLOD$ are used as the test parameters to investigate the performance of the device.

6.3 Performance comparison of single ring and ICR

An the case study, wavelength shifting at the drop ports obtained from n_{eff} detuning is illustrated in Fig 6.3. Both rings have equal radii of 20 μm and the coupling ratios is fixed at 0.1 for both single ring and ICR (including three-waveguide coupler) configurations. We set the parameter obtained from SOI ring as follows: the initial $n_{eff} = 2.4044$ and $n_g = 4.08$ at 1550 nm and index change span $\Delta n_{eff} = 10^{-3}$ divided in three steps.

The green curves and the blue curves in Fig. 6.3(a) represent reference and sensing signals, respectively. In the ICR scheme, the sensing signal exhibits a red-shift and an intensity increase, while the reference signal intensity increases by maintaining the

fixed wavelength. On the other hand, the single ring sensor (see Figure 6.3(b)) has only wavelength shift with negligible peak intensity variations. Thus, the proposed ICR configuration also allows to analyse intensity interrogation in addition to wavelength interrogation.
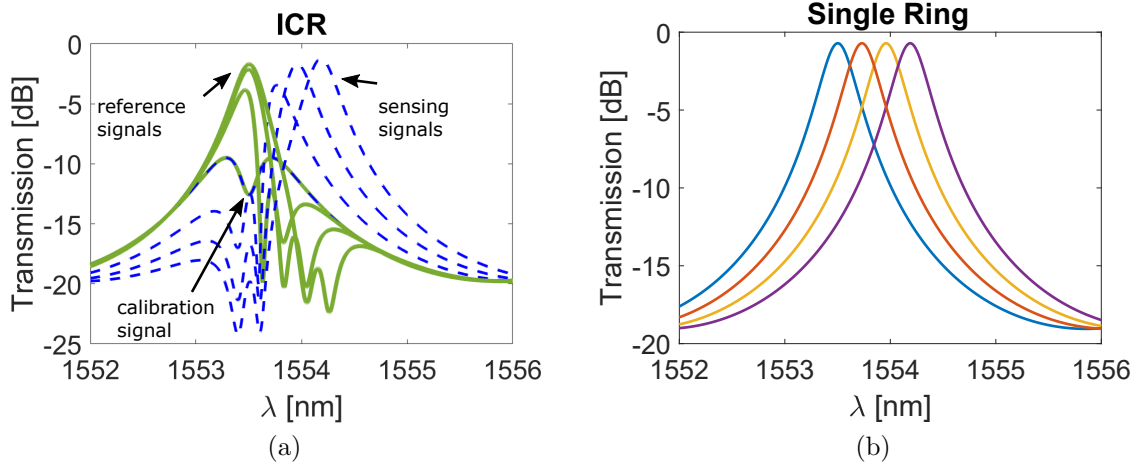
Figure 6.3: (a) Wavelength shifts induced by the change in effective refractive index (from zero to 10^{-3} with three steps) in the drop ports of the ICR (Green curves are the reference signals, while Blue ones are for the sensing ones) and (b) single ring drop port responses (each colour represents index change cumulative index change).

The comparison of the model outcomes of the two approaches is shown in Fig. 6.4. According to the Δn_{eff}, the wavelength shifts $\Delta\lambda$ (red lines) linearly increase in both devices, where shifts in the ICR are defined peak-to-peak distance of sensing and reference signals. However, the peak intensity variation ΔP (blue curves) is available only for the ICR sensor and it shows a rapid increase for a small range of Δn_{eff}, as shown in Figure 6.4(a). On the contrary, the single ring sensor has a very small change in peak intensities which are basically floating-point errors so the ΔP remains in principle constant, as shown in Figure 6.4(b). Table I summarizes the calculated sensing parameters. The wavelength shift sensitivity $S_{\Delta\lambda}$ nm/RIU is calculated from the slopes of the $\Delta\lambda$ and, since both devices have identical rings, $S_{\Delta\lambda}$ is found to be the same (918 nm/RIU). As opposed to the single ring case, the minimum resonance intensity sensitivity of 515 dB/RIU within the range $\Delta n_{eff} = 0.001$ of the ICR sensor demonstrates that it is possible to achieve intensity interrogation for a very accurate sensing performance in a small Δn_{eff} span. The $S_{\Delta P}$ increases as the index change span decreases. The most significant difference of the sensors seems the limit of detection. The resonance line width determines the $iLOD$ such that it ensures at least 3 dB bandwidth separation of two successive resonances. We found that the ICR based sensor requires smaller effective refractive index change to meet $iLOD$ condition than single ring does and the detection limit of the ICR sensor is found to be enhanced by a factor of 5.6 at the price of increased insertion loss of the sensor.

The limiting factor for the intensity sensing is based on the convergence of the ΔP

(a)   (b)
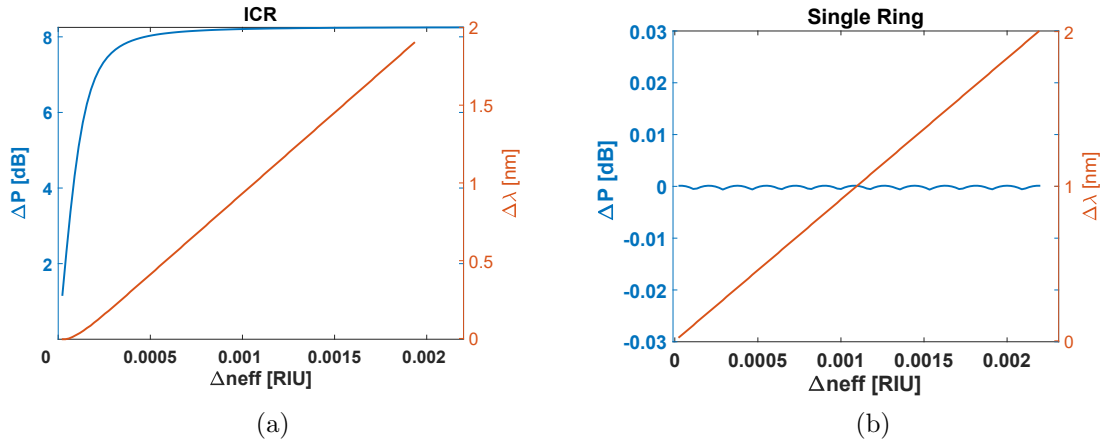
Figure 6.4: Comparison of ΔP (blue curve) and $\Delta\lambda$ (red curve) with respect to the induced Δn_{eff} for coupled ICR (a) and single ring (b) sensing schemes.

TABLE 6.1. CALCULATED SENSOR PARAMETERS: SENSITIVITIES FOR WAVELENGTH $S_{\Delta\lambda}$ AND INTENSITY $S_{\Delta P}$ INTERROGATIONS AND DETECTION LIMITS.

	$S_{\Delta\lambda}$ [nm/RIU]	$S_{\Delta P}$ [dB/RIU]	$iLOD$ [RIU]
Single Ring	918	–	$2.47 \cdot 10^{-4}$
ICR	918	515	$0.44 \cdot 10^{-4}$

curve. For instance, when Δn_{eff} is equivalent to around 0.8 nm wavelength shift, the change in the transmitted power becomes negligible. This effect can be noticed from Fig. 6.3(a), where the green curves around the maximum transmission are very close to each other. However, minimum detectable intensity change is limited by the power measurement accuracy. The curve of ΔP shown in Fig. 6.4(a) can give different values of $S_{\Delta P}$ depending on the minimum acceptable intensity interval; we fixed such value at 0.1 dB and considered that changes below this value are negligible. Therefore, the reported $S_{\Delta P}$ in Table I is the minimum sensitivity. The maximum intensity sensitivity can be achieved in smallest Δn_{eff} such that the power of peaks increases very rapidly and reaches very high sensitivity up to $4.5 \cdot 10^4$ dB/RIU within the value of $iLOD$. Furthermore, it is possible to enhance the intensity interrogation range by increasing the coupling ratio, as shown in Figure 6.5. Stronger coupling strength gives rise to smoother transitions over the x-axes. But, as a consequence of an increased coupling ratio, the FWHM rises and results in $iLOD$ impairment.

One of the main noise sources for biosensors is thermal noise. Either environmental or resonator based self-induced thermal noise becomes critical for very highly sensitive sensors, hence the temperature of the sensor should be precisely controlled during the measurement [126]. This adds another difficulty to realize reliable sensors. To overcome this issue, the proposed differential sensing scheme based on the coupled resonators can in fact provide an alternative approach to compensate environmental thermal noise by an initial calibration of the reference ring phase shift by searching the local maximum of reflection that guarantees single resonance wavelength. Once two
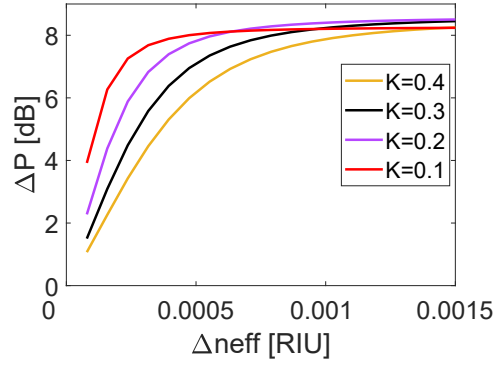
Figure 6.5. Effect of coupling ratio increments on the range of detectable Δn_{eff} in the intensity interrogation scheme.

coupled rings are synchronized, which implies $\theta_1 = \theta_2$, then the resulting $S_{\Delta\lambda}$ and $S_{\Delta P}$ can be disposed of the environmental thermal noise: during the sensing process, it is possible to retrieve spurious wavelength shift by monitoring the reference resonance wavelength. The amount of wavelength shift gives the portion of resonance shifts of the sensing wavelengths caused by thermal noises.

6.4 Conclusions

In this chapter, we proposed and theoretically studied a novel optical biosensing scheme based on differential sensing through the coupled micro ring resonators in SOI technology. The assessment of the sensitivity and limit of detection of the proposed device have been provided by comparing the results obtained from the conventional single ring sensor, having the same technology design parameters such as coupling ratio and radius. Sensitivity of the wavelength interrogation was found to be identical for each type of device, while the ICR based sensor has enhanced limit of detection by a factor of 5.6 compared to the single ring sensor.

In addition, the presented device also supports intensity interrogation which is not the case for single ring if only the spectral measurement is considered. However, such interrogation was found to be possible only for a very small effective refractive index change. The way of increasing the range of a detectable index change was reported and possible resulting impairment on the limit of detection has been described.

Thanks to the possibility of an initial calibration of the device by monitoring the back reflection, differential sensing scheme can eliminate environmental and self-induced thermal noises. Therefore, this scheme can provide on-chip thermal control by integrated micro resistors on the reference ring for realizing reliable integrated biosensors and cost effective measurements.

Chapter 7

Conclusions and future works

In this thesis, applications of coupled ring resonators have been extensively investigated. The theoretical and experimental outcomes have been elaborated, aiming at introducing indirectly coupled micro ring resonators as a novel Building Block for Photonic Integrated Circuits. The methodology followed in the thesis includes modelling, design and experimental characterization of devices fabricated through Multi Project Wafer runs. Two different integration platforms (SOI, IMOS) have been considered to investigate potential features of the proposed indirectly coupled resonators (ICR).

The presented research has first focused on basic photonic circuits elements such as single mode waveguides and directional couplers. In Chapter 2, material structures of the Silicon-on-Insulator (SOI) and Indium-phosphide Membrane on Silicon (IMOS) integration platforms have been introduced. The experimental characterization results of TE and TM mode directional couplers fabricated with IMOS technology have been provided. According to obtained results TM mode couplers have exhibited better agreement with the theoretical expectations. The modal simulation results suggested that the critical issue for the TE mode coupler fabrication relies on the etching process for narrow trenches. Since Micro ring resonators (MRRs) have two main design aspects as coupling strength and length of the resonator, this part of the thesis has been carried out to support interpretations on possible implications of resonator performance that may happen. The findings of this analysis are valid to any integration technology that uses high-index-contrast structures if their waveguide thickness is precisely controlled.

In Chapter 3, analytical models of single and embedded ring resonators as well as ICR have been developed using the Transfer Matrix Method. The obtained transfer functions have been used throughout the thesis for fitting or/and interpreting fabricated devices' behaviours. Working conditions of Type-I ICR for wavelength routing and reflection have been addressed and commented to achieve best performance for reflection condition. Static transfer function measurements of the single Silicon ring resonators have been provided. The fabricated devices with ring radii in a range of 12 to 25 μm showed FSRs range from 3.75 up to 7.85 nm. The maximum obtained Q-factor was 19,500 corresponding to 0.08 nm of FWHM of the ring with 25 μm of radius.

The obtained thermal tuning parameters were 95 pm/°C for temperature variation and 110 pm/mW of applied power on integrated heaters.

Assessments of wavelength routing properties of ICRs have been made in Chapter 4, in the context of WDM technology based Flexible Optical Networking and Network-on-Chip applications. Non reciprocal wavelength routing provided by ICRs has been exploited to establish the concept of bidirectional communication in transponder aggregator units for the next generation Reconfigurable Optical Add/Drop Multiplexer (ROADM) systems. A 2-direction 4-channel colourless/directionless/contentionless transponder aggregator (TPA) scheme has been proposed. This scheme unifies add/drop sections which have been considered two separated units in the previously proposed TPA architectures. It has been demonstrated by the concept of bidirectional communication that the proposed architecture can reduce the cost of add/drop functions in ROADM systems. Furthermore, scalability analysis of ICR-based wavelength router topology has been carried out and compared with the conventional photonic switch element (PSE) based λ-router topology. The comparison was made according to the number of rings required to construct N×N network. It has been demonstrated that ICR-based topology can implement equal number of connectivities with a reduced number of rings up to ~ 50%. The proposed topology has been compared with also non-ring based switching fabric approaches in terms of number of switching element and, according to generalized formulations of scalable networks, the ICR-based topology up to 16×16 network has the fewest number of switching element than any other fabrics reported in the literature. Through Bit-Error-Rate measurements with 3×10Gbps DWDM links, networking performances of the first-stage single Silicon MRR, PSE and ICR have been carried out by means of interferometric crosstalk and the results have shown similar performances for all the devices with minimal power penalties.

Then, directly coupled two embedded ring resonators have also been reviewed by experiments on SOI devices. The target application was a bandwidth variable add/drop channel filter. Both horizontally and vertically embedded rings have been measured and results have been provided and commented. However, it has been observed by experiments that operating embedded rings for achieving desired phase difference of the two resonators was difficult. In particular, the resonance spectrum of the tested devices was not uniform enough; therefore, bandwidth tuning has been performed insufficiently in terms of insertion loss. A positive outcome has been attained from the two cascaded horizontally embedded ring resonator circuits. Overcoupled rings have performed flat-top passbands with a linewidth of 166 GHz in a wavelength range of 1540 and 1550 nm, which was almost entirely demultiplexed by the drop ports transmission. This transmission profile has been considered for the implementation of interleavers in the proposed transponder aggregator where the add/drop wavelengths were assigned with even and odd numbers.

As the second field of application, ICR Type-I has been considered as a reflector

and results of this analysis have been presented in Chapter 5. By implementing phase synchronization of coupled resonators, an ICR realized with different radii acts as a single wavelength reflector. The experimental results of SOI ICR showed a good agreement with the model outcomes. The average measured reflectivity over a wavelength span of 37 nm was 0.55, with a peak of about 50 pm full-width-half-maximum, which corresponds to a quality factor of ~ 30,000. On the other hand, an ICR with identical rings fabricated with the IMOS platform has been tested without thermal tuning and the device has performed a comb-like reflection spectrum consists of 8 wavelengths in 50 nm of wavelength span (1490-1540 nm) with a maximum fluctuation of 1.84 dB.

As the last type of application, a differential optical sensing scheme based on the ICR has been proposed and theoretically investigated in Chapter 6. An on-chip sensor calibration method to limit the environmentally induced thermal noise has been introduced. A theoretical case study has been carried out to compare its performance with that of a single ring based sensor. According to the model based analysis, the achieved limit of detection enhancement was a factor of 5.6 in the ICR type sensor. By leveraging reflection and routing conditions, ICRs can support both wavelength and intensity interrogation measurements, in which the latter can provide very high sensitivity in a short range of effective refractive index change.

In overall, outcomes of the conducted research of my doctoral activities have been presented in this thesis. One of the strongest assets of ICRs is the versatility: they are easy designable and easy operable. This is important since photonic circuits designers can use the presented analytical function and related working regimes to implement desired photonic functions and hopefully explore novel applications. ICRs as a new set of Building Block can improve PDK portfolio of any photonic integration fabs.

Looking forward

Throughout the thesis, a number of application fields have been inspected to assess potential features of ICRs. A variety of the investigated applications together with the outcomes of the presented research have arisen also questions not only answers. Future work considerations cover several continuum subjects. First of all, the proposed ICR-based wavelength router fabric has been investigated only in terms of power consumption of the switching matrix. However, in order to reveal true potentials of such routers, crosstalk analysis also need to be elaborated to make possible realization of the proposed transponder aggregator and to validate bidirectional communication performance in real applications.

Monitoring actual routing wavelength assignments in integrated switching fabrics is an important issue for power management and stabilization. This process is mainly carried out by distributed integrated photodetectors that use a portion of the routing wavelength on networks for feedbacks. Looking for a possible answer for the following question can be a part of the future works: would it be viable using ICRs to provide a

feedback system in switching matrices when an ICR is in reflection state?

Type-II ICR has been considered only for routing applications. However, its phase shift synchronization regime, instead of reflection, can split the power of the common resonance equally. One of the next studies will consider Type-II ICRs as a tunable wavelength selective 50:50 power splitter.

Finally, a possible implementation of differential optical sensing scheme would be definitely helpful to determine feasibility of the proposed sensing scheme.

Bibliography

[1] Meint Smit et al. An introduction to InP-based generic integration technology. Semiconductor Science and Technology, 29(8):083001, jun 2014.

[2] A. Eu-Jin Lim, J. Song, Q. Fang, C. Li, X. Tu, N. Duan, K. Kiong Chen, R. Poh-Cher Tern, and T. Liow. Review of silicon photonics foundry efforts. IEEE Journal of Selected Topics in Quantum Electronics, 20:405–416, 2014.

[3] L. Chrostowski, H. Shoman, M. Hammood, H. Yun, J. Jhoja, E. Luan, S. Lin, A. Mistry, D. Witt, N. A. F. Jaeger, S. Shekhar, H. Jayatilleka, P. Jean, S. B. . Villers, J. Cauchon, W. Shi, C. Horvath, J. N. Westwood-Bachman, K. Setzer, M. Aktary, N. S. Patrick, R. J. Bojko, A. Khavasi, X. Wang, T. Ferreira de Lima, A. N. Tait, P. R. Prucnal, D. E. Hagan, D. Stevanovic, and A. P. Knights. Silicon photonic circuit design using rapid prototyping foundry process design kits. IEEE Journal of Selected Topics in Quantum Electronics, 25(5):1–26, Sep. 2019.

[4] A. Rahim, J. Goyvaerts, B. Szelag, J. Fedeli, P. Absil, T. Aalto, M. Harjanne, C. Littlejohns, G. Reed, G. Winzer, S. Lischke, L. Zimmermann, D. Knoll, D. Geuzebroek, A. Leinse, M. Geiselmann, M. Zervas, H. Jans, A. Stassen, C. Domínguez, P. Muñoz, D. Domenech, A. L. Giesecke, M. C. Lemme, and R. Baets. Open-access silicon photonics platforms in europe. IEEE Journal of Selected Topics in Quantum Electronics, 25(5):1–18, Sep. 2019.

[5] P. Muñoz, P. W. L. van Dijk, D. Geuzebroek, M. Geiselmann, C. Domínguez, A. Stassen, J. D. Doménech, M. Zervas, A. Leinse, C. G. H. Roeloffzen, B. Gargallo, R. Baños, J. Fernández, G. M. Cabanes, L. A. Bru, and D. Pastor. Foundry developments toward silicon nitride photonics from visible to the mid-infrared. IEEE Journal of Selected Topics in Quantum Electronics, 25(5):1–13, Sep. 2019.

[6] C. Kopp, S. Bernabé, B. B. Bakir, J. Fedeli, R. Orobtchouk, F. Schrank, H. Porte, L. Zimmermann, and T. Tekin. Silicon photonic circuits: On-cmos integration, fiber optical coupling, and packaging. IEEE Journal of Selected Topics in Quantum Electronics, 17(3):498–509, May 2011.

[7] Vladimir Stojanović, Rajeev J. Ram, Milos Popović, Sen Lin, Sajjad Moazeni, Mark Wade, Chen Sun, Luca Alloatti, Amir Atabaki, Fabio Pavanello, Nandish

Mehta, and Pavan Bhargava. Monolithic silicon-photonic platforms in state-of-the-art cmos soi processes. Opt. Express, 26(10):13106–13121, May 2018.

[8] J. J. G. M. van der Tol, Y. Jiao, L. Shen, A. Millan-Mejia, V. Pogoretskii, J. P. van Engelen, and M. K. Smit. Indium phosphide integrated photonics in membranes. IEEE Journal of Selected Topics in Quantum Electronics, 24(1):1–9, Jan 2018.

[9] M. Smit, J. J. G. M. van der Tol, and M. Hill. Moore's law in photonics. Laser Photonics Rev., 6:1–13, 2012.

[10] M. U. Khan, Y. Xing, Y. Ye, and W. Bogaerts. Photonic integrated circuit design in a foundry+fabless ecosystem. IEEE Journal of Selected Topics in Quantum Electronics, 25(5):1–14, Sep. 2019.

[11] E. A. J. Marcatili. Bends in optical dielectric guides. The Bell System Technical Journal, 48(7):2103–2132, Sep. 1969.

[12] B. E. Little, J. S. Foresi, G. Steinmeyer, E. R. Thoen, S. T. Chu, H. A. Haus, E. P. Ippen, L. C. Kimerling, and W. Greene. Ultra-compact si-sio2 microring resonator optical channel dropping filters. IEEE Photonics Technology Letters, 10(4):549–551, April 1998.

[13] C. Manolatou, M. J. Khan, S. Fan, P. R. Villeneuve, H. A. Haus, and J. D. Joannopoulos. Coupling of modes analysis of resonant channel add-drop filters. IEEE Journal of Quantum Electronics, 35(9):1322–1331, Sep. 1999.

[14] O. Schwelb. Transmission, group delay, and dispersion in single-ring optical resonators and add/drop filters-a tutorial overview. Journal of Lightwave Technology, 22(5):1380–1394, May 2004.

[15] J. P. Hohimer and G. A. Vawter. Passive mode locking of monolithic semiconductor ring lasers at 86 ghz. Applied Physics Letters, 63(12):1598–1600, 1993.

[16] Bin Liu, Ali Shakouri, , and John E. Bowers. Passive microring-resonator-coupled lasers. Applied Physics Letters, 79(22):3561–3563, 2001.

[17] Qianfan Xu, Bradley Schmidt, Sameer Pradhan, and Michal Lipson. Micrometre-scale silicon electro-optic modulator. Nature, 435:325–327, 2005.

[18] Iosif Demirtzioglou, Cosimo Lacava, Kyle R. H. Bottrill, David J. Thomson, Graham T. Reed, David J. Richardson, and Periklis Petropoulos. Frequency comb generation in a silicon ring resonator modulator. Opt. Express, 26(2):790–796, Jan 2018.

[19] A. W. Poon, X. Luo, F. Xu, and H. Chen. Cascaded microresonator-based matrix switch for silicon on-chip optical interconnection. Proceedings of the IEEE, 97(7):1216–1238, July 2009.

[20] F. Testa, C. J. Oton, C. Kopp, J. Lee, R. Ortuño, R. Enne, S. Tondini, G. Chiaretti, A. Bianchi, P. Pintus, M. Kim, D. Fowler, J. A. Ayúcar, M. Hofbauer, M. Mancinelli, M. Fournier, G. B. Preve, N. Zecevic, C. L. Manganelli, C. Castellan, G. Parès, O. Lemonnier, F. Gambini, P. Labeye, M. Romagnoli, L. Pavesi, H. Zimmermann, F. Di Pasquale, and S. Stracca. Design and implementation of an integrated reconfigurable silicon photonics switch matrix in iris project. IEEE Journal of Selected Topics in Quantum Electronics, 22(6):155–168, Nov 2016.

[21] Nicolás Sherwood-Droz, Howard Wang, Long Chen, Benjamin G. Lee, Aleksandr Biberman, Keren Bergman, and Michal Lipson. Optical 4×4 hitless silicon router for optical networks-on-chip (noc). Opt. Express, 16(20):15915–15922, Sep 2008.

[22] A. Parini, G. Bellanca, A. Annoni, F. Morichetti, A. Melloni, M. J. Strain, M. Sorel, M. Gay, C. Pareige, L. Bramerie, and M. Thual. Ber evaluation of a passive soi wdm router. IEEE Photonics Technology Letters, 25(23):2285–2288, Dec 2013.

[23] Q. Cheng, M. Bahadori, Y. Hung, Y. Huang, N. Abrams, and K. Bergman. Scalable microring-based silicon clos switch fabric with switch-and-select stages. IEEE Journal of Selected Topics in Quantum Electronics, 25(5):1–11, Sep. 2019.

[24] Y. Huang, Q. Cheng, Y. Hung, H. Guan, X. Meng, A. Novack, M. Streshinsky, M. Hochberg, and K. Bergman. Multi-stage 8×8 silicon photonic switch based on dual-microring switching elements. Journal of Lightwave Technology, 38(2):194–201, Jan 2020.

[25] Indranil Chakraborty, Gobinda Saha, Abhronil Sengupta, and Kaushik Roy. Toward fast neural computing using all-photonic phase change spiking neurons. Scientific Reports, 8(1):12980, 2018.

[26] Alexander N. Tait, Thomas Ferreira de Lima, Ellen Zhou, Allie X. Wu, Mitchell A. Nahmias, Bhavin J. Shastri, and Paul R. Prucnal. Neuromorphic photonic networks using silicon photonic weight banks. Scientific Reports, 7(1):7430, 2017.

[27] V. Bangari, B. A. Marquez, H. Miller, A. N. Tait, M. A. Nahmias, T. F. de Lima, H. Peng, P. R. Prucnal, and B. J. Shastri. Digital electronics and analog photonics for convolutional neural networks (deap-cnns). IEEE Journal of Selected Topics in Quantum Electronics, 26(1):1–13, Jan 2020.

[28] F. D. Coarer, M. Sciamanna, A. Katumba, M. Freiberger, J. Dambre, P. Bienstman, and D. Rontani. All-optical reservoir computing on a photonic chip using silicon-based ring resonators. IEEE Journal of Selected Topics in Quantum Electronics, 24(6):1–8, Nov 2018.

[29] W. Bogaerts, P. De Heyn, T. Van Vaerenbergh, K. De Vos, S. Kumar Selvaraja, T. Claes, P. Dumon, P. Bienstman, D. Van Thourhout, and R. Baets. Silicon microring resonators. Laser & Photonics Reviews, 6(1):47–73, 2012.

[30] F. Morichetti, C. Ferrari, A. Canciamilla, and A. Melloni. The first decade of coupled resonator optical waveguides: bringing slow light to applications. Laser & Photonics Reviews, 6(1):74–96, 2012.

[31] M. Mancinelli, R. Guider, P. Bettotti, M. Masi, M. R. Vanacharla, and L. Pavesi. Coupled-resonator-induced-transparency concept for wavelength routing applications. Opt. Express, 19(13):12227–12240, Jun 2011.

[32] Mikhail F. Limonov, Mikhail V. Rybin, Alexander N. Poddubny, and Yuri S. Kivshar. Fano resonances in photonics. Nature Photonics, 11:543–554, 2017.

[33] Peng Bo, Özdemir Şahin Kaya, Chen Weijian, Nori Franco, and Yang Lan. What is and what is not electromagnetically induced transparency in whispering-gallery microcavities. Nature Communications, 5(1):5082–7119, 2014.

[34] Zhenzheng Wang, Qi Lu, Yi Wang, Jinsong Xia, and Qingzhong Huang. Electromagnetically induced transparency and absorption in a compact silicon ring-bus-ring-bus system. Opt. Express, 25(13):14368–14377, Jun 2017.

[35] Shuang Zheng, Zhengsen Ruan, Shengqian Gao, Yun Long, Shimao Li, Mingbo He, Nan Zhou, Jing Du, Li Shen, Xinlun Cai, and Jian Wang. Compact tunable electromagnetically induced transparency and fano resonance on silicon platform. Opt. Express, 25(21):25655–25662, Oct 2017.

[36] Jacob Scheuer, Andrey A. Sukhorukov, and Yuri S. Kivshar. All-optical switching of dark states in nonlinear coupled microring resonators. Opt. Lett., 35(21):3712–3714, Nov 2010.

[37] Lin Zhang, Muping Song, Teng Wu, Lianggang Zou, Raymond G. Beausoleil, and Alan E. Willner. Embedded ring resonators for microphotonic applications. Opt. Lett., 33(17):1978–1980, Sep 2008.

[38] C. Qiu, T. Hu, P. Yu, A. Shen, F. Wang, X. Q. Jiang, and J. Y. Yang. A temperature sensor based on silicon eye-like microring with sharp asymmetric fano resonance. In The 9th International Conference on Group IV Photonics (GFP), pages 123–125, Aug 2012.

[39] Gencheng Wang, Tingge Dai, Jianfei Jiang, Hui Yu, Yinlei Hao, Yuehai Wang, Yubo Li, Xiaoqing Jiang, and Jianyi Yang. Slope tunable fano resonances in asymmetric embedded microring resonators. Journal of Optics, 19(2):025803, jan 2017.

[40] Yundong Zhang, Kai Ma, Yongfeng Wu, Huaiyin Su, Hui Li, and Ping Yuan. Superluminal and slow light in eye-like ring resonator. In Selim M. Shahriar and Jacob Scheuer, editors, Slow Light, Fast Light, and Opto-Atomic Precision Metrology X, volume 10119, pages 61 – 67. International Society for Optics and Photonics, SPIE, 2017.

[41] COMSOL Multiphysics. https://www.comsol.com.

[42] A. Melloni, R. Costa, G. Cusmai, F. Morichetti, and M. Martinelli. Waveguide index contrast: implications for passive integrated optical components. In Proceedings of 2005 IEEE/LEOS Workshop on Fibres and Optical Passive Components, 2005., pages 246–253, June 2005.

[43] OptoDesigner. https://www.synopsys.com/.

[44] B. M. A. Rahman, D. M. H. Leung, S. S. A. Obayya, and K. T. V. Grattan. Numerical analysis of bent waveguides: bending loss, transmission loss, mode coupling, and polarization coupling. Appl. Opt., 47(16):2961–2970, Jun 2008.

[45] O. Schwelb. Transmission, group delay, and dispersion in single-ring optical resonators and add/drop filters-a tutorial overview. Journal of Lightwave Technology, 22(5):1380–1394, May 2004.

[46] E. A. J. Marcatili. Dielectric rectangular waveguide and directional coupler for integrated optics. The Bell System Technical Journal, 48(7):2071–2102, Sep. 1969.

[47] D. Marcuse. The coupling of degenerate modes in two parallel dielectric waveguides. The Bell System Technical Journal, 50(6):1791–1816, July 1971.

[48] A. Yariv. Coupled-mode theory for guided-wave optics. IEEE Journal of Quantum Electronics, 9(9):919–933, Sep. 1973.

[49] H. Kogelnik and R. Schmidt. Switched directional couplers with alternating $\Delta\beta$. IEEE Journal of Quantum Electronics, 12(7):396 – 401, July 1976.

[50] R. Schmidt and R. Alferness. Directional coupler switches, modulators, and filters using alternating $\Delta\beta$ techniques. IEEE Transactions on Circuits and Systems, 26(12):1099–1108, December 1979.

[51] H. Haus and C. Fonstad. Three-waveguide couplers for improved sampling and filtering. IEEE Journal of Quantum Electronics, 17(12):2321–2325, December 1981.

[52] H. A. Haus and W. Huang. Coupled-mode theory. Proceedings of the IEEE, 79(10):1505–1518, Oct 1991.

[53] A. Takagi, K. Jinguji, and M. Kawachi. Wavelength characteristics of (2*2) optical channel-type directional couplers with symmetric or nonsymmetric coupling structures. Journal of Lightwave Technology, 10(6):735–746, June 1992.

[54] Wei-Ping Huang. Coupled-mode theory for optical waveguides: an overview. J. Opt. Soc. Am. A, 11(3):963–983, Mar 1994.

[55] Chang-Min Kim and Young-Joon Im. Switching operations of three-waveguide optical switches. IEEE Journal of Selected Topics in Quantum Electronics, 6(1):170–174, Jan 2000.

[56] Gaetano Bellanca, Piero Orlandi, and Paolo Bassi. Assessment of the orthogonal and non-orthogonal coupled-mode theory for parallel optical waveguide couplers. J. Opt. Soc. Am. A, 35(4):577–585, Apr 2018.

[57] Y. Jiao, J. Liu, A. M. Mejia, L. Shen, and J. van der Tol. Ultra-sharp and highly tolerant waveguide bends for inp photonic membrane circuits. IEEE Photonics Technology Letters, 28(15):1637–1640, Aug 2016.

[58] R. G. Hunsperger. Integrated Optics, chapter 8. Springer, 5th edition, 2013.

[59] Lukas Chrostowski and Michael Hochberg. Silicon Photonics Design: From Devices to Systems, chapter 4. Cambridge University Press, 2015.

[60] The MathWorks. https://www.mathworks.com.

[61] Andreas Prinzen, Michael Waldow, and Heinrich Kurz. Fabrication tolerances of soi based directional couplers and ring resonators. Opt. Express, 21(14):17212–17220, Jul 2013.

[62] B. E. Little, S. T. Chu, W. Pan, and Y. Kokubun. Microring resonator arrays for vlsi photonics. IEEE Photonics Technology Letters, 12(3):323–325, March 2000.

[63] Lumerical FDTD. https://www.lumerical.com.

[64] A. Yariv. Universal relations for coupling of optical power between microresonators and dielectric waveguides. Electronics Letters, 36(4):321–322, Feb 2000.

[65] A. Yariv. Critical coupling and its control in optical waveguide-ring resonator systems. IEEE Photonics Technology Letters, 14(4):483–485, April 2002.

[66] Dominik G. Rabus. <u>Integrated Ring Resonator The Compendium</u>, chapter 2. Springer-Verlag Berlin Heidelberg, 1st edition, 2007.

[67] Dajian Liu, Chong Zhang, Di Liang, and Daoxin Dai. Submicron-resonator-based add-drop optical filter with an ultra-large free spectral range. <u>Opt. Express</u>, 27(2):416–422, Jan 2019.

[68] I. Tomkos, S. Azodolmolky, J. Solé-Pareta, D. Careglio, and E. Palkopoulou. A tutorial on the flexible optical networking paradigm: State of the art, trends, and research challenges. <u>Proceedings of the IEEE</u>, 102(9):1317–1337, Sep. 2014.

[69] A. Yariv. Coupled-mode theory for guided-wave optics. <u>IEEE Journal of Quantum Electronics</u>, 9(9):919–933, Sep. 1973.

[70] Xiaoyan Zhou, Lin Zhang, Andrea M. Armani, Raymond G. Beausoleil, Alan E. Willner, and Wei Pang. Power enhancement and phase regimes in embedded microring resonators in analogy with electromagnetically induced transparency. <u>Opt. Express</u>, 21(17):20179–20186, Aug 2013.

[71] Chang-Min Kim and Young-Joon Im. Switching operations of three-waveguide optical switches. <u>IEEE Journal of Selected Topics in Quantum Electronics</u>, 6(1):170–174, Jan 2000.

[72] Qixiang Cheng, Meisam Bahadori, Madeleine Glick, Sébastien Rumley, and Keren Bergman. Recent advances in optical technologies for data centers: a review. <u>Optica</u>, 5(11):1354–1370, Nov 2018.

[73] T. Alexoudi, N. Terzenidis, S. Pitris, M. Moralis-Pegios, P. Maniotis, C. Vagionas, C. Mitsolidou, G. Mourgias-Alexandris, G. T. Kanellos, A. Miliou, K. Vyrsokinos, and N. Pleros. Optics in computing: From photonic network-on-chip to chip-to-chip interconnects and disintegrated architectures. <u>Journal of Lightwave Technology</u>, 37(2):363–379, Jan 2019.

[74] Guofang Fan, Regis Orobtchouk, Bing Han, Yuan Li, and Hongyu Li. 8 x 8 wavelength router of optical network on chip. <u>Opt. Express</u>, 25(20):23677–23683, Oct 2017.

[75] Z. Yao, K. Wu, B. X. Tan, J. Wang, Y. Li, Y. Zhang, and A. W. Poon. Integrated silicon photonic microresonators: Emerging technologies. <u>IEEE Journal of Selected Topics in Quantum Electronics</u>, 24(6):1–24, Nov 2018.

[76] M. Jinno, H. Takara, B. Kozicki, Y. Tsukishima, Y. Sone, and S. Matsuoka. Spectrum-efficient and scalable elastic optical path network: architecture, benefits, and enabling technologies. <u>IEEE Communications Magazine</u>, 47(11):66–73, November 2009.

[77] O. Gerstel, M. Jinno, A. Lord, and S. J. B. Yoo. Elastic optical networking: a new dawn for the optical layer? IEEE Communications Magazine, 50(2):s12–s20, February 2012.

[78] B. C. Chatterjee, N. Sarma, and E. Oki. Routing and spectrum allocation in elastic optical networks: A tutorial. IEEE Communications Surveys Tutorials, 17(3):1776–1800, thirdquarter 2015.

[79] D. M. Marom, P. D. Colbourne, A. D'errico, N. K. Fontaine, Y. Ikuma, R. Proietti, L. Zong, J. M. Rivas-Moscoso, and I. Tomkos. Survey of photonic switching architectures and technologies in support of spatially and spectrally flexible optical networking. IEEE/OSA Journal of Optical Communications and Networking, 9(1):1–26, Jan 2017.

[80] Simmons Jane M. Optical Network Design and Planning. Springer, Cham, 2014.

[81] T. Watanabe, K. Suzuki, T. Goh, K. Hattori, A. Mori, T. Takahashi, T. Sakamoto, K. Morita, S. Sohma, and S. Kamei. Compact plc-based transponder aggregator for colorless and directionless ROADM. In 2011 Optical Fiber Communication Conference and Exposition and the National Fiber Optic Engineers Conference, pages 1–3, March 2011.

[82] Y. Ikuma, K. Suzuki, N. Nemoto, E. Hashimoto, O. Moriwaki, and T. Takahashi. Low-loss transponder aggregator using spatial and planar optical circuit. Journal of Lightwave Technology, 34(1):67–72, Jan 2016.

[83] A. Shacham, K. Bergman, and L. P. Carloni. On the design of a photonic network-on-chip. In First International Symposium on Networks-on-Chip (NOCS'07), pages 53–64, May 2007.

[84] R. Hendry, D. Nikolova, S. Rumley, and K. Bergman. Modeling and evaluation of chip-to-chip scale silicon photonic networks. In 2014 IEEE 22nd Annual Symposium on High-Performance Interconnects, pages 1–8, Aug 2014.

[85] P. Pintus, P. Contu, N. Andriolli, A. D'Errico, F. Di Pasquale, and F. Testa. Analysis and design of microring-based switching elements in a silicon photonic integrated transponder aggregator. Journal of Lightwave Technology, 31(24):3943–3955, Dec 2013.

[86] Edwin J. Klein, Patryk Urban, Gabriel Sengo, Lucy T. H. Hilderink, Marcel Hoekman, Rudy Pellens, Paul van Dijk, and Alfred Driessen. Densely integrated microring resonator based photonic devices for use in access networks. Opt. Express, 15(16):10346–10355, Aug 2007.

[87] T. Mizuno, Y. Hida, T. Kitoh, M. Kohtoku, M. Oguma, Y. Inoue, and Y. Hibino. 12.5-ghz spacing compact and low-loss interleave filter using 1.5% Δ silica-based waveguide. IEEE Photonics Technology Letters, 16(11):2484–2486, Nov 2004.

[88] Duanni Huang, Paolo Pintus, Chong Zhang, Paul Morton, Yuya Shoji, Tetsuya Mizumoto, and John E. Bowers. Dynamically reconfigurable integrated optical circulators. Optica, 4(1):23–30, Jan 2017.

[89] R. Jensen, A. Lord, and N. Parsons. Colourless, directionless, contentionless roadm architecture using low-loss optical matrix switches. In 36th European Conference and Exhibition on Optical Communication, pages 1–3, Sep. 2010.

[90] Sebastian Werner, Javier Navaridas, and Mikel Luján. A survey on optical network-on-chip architectures. ACM Comput. Surv., 50(6), December 2017.

[91] H. Jayatilleka, K. Murray, M. Caverley, N. A. F. Jaeger, L. Chrostowski, and S. Shekhar. Crosstalk in soi microring resonator-based filters. Journal of Lightwave Technology, 34(12):2886–2896, June 2016.

[92] M. Nikdast, J. Xu, L. H. K. Duong, X. Wu, X. Wang, Z. Wang, Z. Wang, P. Yang, Y. Ye, and Q. Hao. Crosstalk noise in wdm-based optical networks-on-chip: A formal study and comparison. IEEE Transactions on Very Large Scale Integration (VLSI) Systems, 23(11):2552–2565, Nov 2015.

[93] M. Briere, B. Girodias, Y. Bouchebaba, G. Nicolescu, F. Mieyeville, F. Gaffiot, and I. O'Connor. System level assessment of an optical noc in an mpsoc platform. In 2007 Design, Automation Test in Europe Conference Exhibition, pages 1–6, April 2007.

[94] A. Scandurra and I. OConnor. Scalable cmos-compatible photonic routing topologies for versatile networks on chip. In Network on Chip Architecture (NoCArc 2008), Nov 2008.

[95] K. Suzuki, R. Konoike, S. Suda, H. Matsuura, S. Namiki, H. Kawashima, and K. Ikeda. Low-loss, low-crosstalk, and large-scale optical switch based on silicon photonics. Journal of Lightwave Technology, 38(2):233–239, Jan 2020.

[96] Lin Shen, Liangjun Lu, Zhanzhi Guo, Linjie Zhou, and Jianping Chen. Silicon optical filters reconfigured from a 16×16 benes switch matrix. Opt. Express, 27(12):16945–16957, Jun 2019.

[97] Q. Cheng, Y. Huang, H. Yang, M. Bahadori, N. Abrams, X. Meng, M. Glick, Y. Liu, M. Hochberg, and K. Bergman. Silicon photonic switch topologies and routing strategies for disaggregated data centers. IEEE Journal of Selected Topics in Quantum Electronics, pages 1–1, 2019.

[98] P. Pintus, C. Manganelli, S. Tondini, M. Mancinelli, F. Gambini, C. Castellan, F. Di Pasquale, L. Pavesi, F. Testa, and C. J. Oton. Silicon photonic toolkit for integrated switching matrices. In 18th Italian National Conference on Photonic Technologies (Fotonica 2016), pages 1–4, June 2016.

[99] Haishan Sun, Antao Chen, and Larry R. Dalton. A reflective microring notch filter and sensor. Opt. Express, 17(13):10731–10737, Jun 2009.

[100] Wei Shi, Raha Vafaei, Miguel Ángel Guillén Torres, Nicolas A. F. Jaeger, and Lukas Chrostowski. Design and characterization of microring reflectors with a waveguide crossing. Opt. Lett., 35(17):2901–2903, Sep 2010.

[101] J. Montalvo, C. Vázquez, and D. S. Montero. Cwdm self-referencing sensor network based on ring resonators in reflective configuration. Opt. Express, 14(11):4601–4610, May 2006.

[102] G. T. Paloczi, J. Scheuer, and A. Yariv. Compact microring-based wavelength-selective inline optical reflector. IEEE Photonics Technology Letters, 17(2):390–392, Feb 2005.

[103] Jacob Scheuer, George T. Paloczi, and Amnon Yariv. All optically tunable wavelength-selective reflector consisting of coupled polymeric microring resonators. Applied Physics Letters, 87(25):251102, 2005.

[104] I. Chremmos and N. Uzunoglu. Reflective properties of double-ring resonator system coupled to a waveguide. IEEE Photonics Technology Letters, 17(10):2110–2112, Oct 2005.

[105] Y. Chung, Doo-Gun Kim, and N. Dagli. Reflection properties of coupled-ring reflectors. Journal of Lightwave Technology, 24(4):1865–1874, April 2006.

[106] J. K. S. Poon, J. Scheuer, and A. Yariv. Wavelength-selective reflector based on a circular array of coupled microring resonators. IEEE Photonics Technology Letters, 16(5):1331–1333, May 2004.

[107] J. Park, T. Lee, D. Lee, S. Kim, W. Hwang, and Y. Chung. Widely tunable coupled-ring-reflector filter based on planar polymer waveguide. IEEE Photonics Technology Letters, 20(12):988–990, June 2008.

[108] Amir Arbabi, Young Mo Kang, Ching-Ying Lu, Edmond Chow, and Lynford L. Goddard. Realization of a narrowband single wavelength microring mirror. Applied Physics Letters, 99(9):091105, 2011.

[109] Wei Shi, Han Yun, Wen Zhang, Charlie Lin, Ting Kai Chang, Yun Wang, Nicolas A. F. Jaeger, and Lukas Chrostowski. Ultra-compact, high-q silicon microdisk reflectors. Opt. Express, 20(20):21840–21846, Sep 2012.

[110] Min Ren, Hong Cai, Lip Ket Chin, K. Radhakrishnan, Yuandong Gu, Guo-Qiang Lo, Dim Lee Kwong, and Ai Qun Liu. Coupled-ring reflector in an external-cavity tunable laser. Optica, 2(11):940–943, Nov 2015.

[111] Robert Boeck, Michael Caverley, Lukas Chrostowski, and Nicolas A. F. Jaeger. Grating-assisted silicon-on-insulator racetrack resonator reflector. Opt. Express, 23(20):25509–25522, Oct 2015.

[112] Otto Schwelb and István Frigyes. Vernier operation of series-coupled optical microring resonator filters. Microwave and Optical Technology Letters, 39(4):257–261, 2003.

[113] B. E. Little, S. T. Chu, H. A. Haus, J. Foresi, and J. . Laine. Microring resonator channel dropping filters. Journal of Lightwave Technology, 15(6):998–1005, June 1997.

[114] C. L. Manganelli, P. Pintus, F. Gambini, D. Fowler, M. Fournier, S. Faralli, C. Kopp, and C. J. Oton. Large-fsr thermally tunable double-ring filters for wdm applications in silicon photonics. IEEE Photonics Journal, 9(1):1–10, Feb 2017.

[115] Y. Chung, Doo-Gun Kim, and N. Dagli. Widely tunable coupled-ring reflector laser diode. IEEE Photonics Technology Letters, 17(9):1773–1775, Sep. 2005.

[116] T. Yen and Y. Hung. Narrowband dual-wavelength silicon waveguide bragg reflectors. Journal of Lightwave Technology, 37(20):5326–5332, Oct 2019.

[117] F. Morichetti, A. Canciamilla, M. Martinelli, A. Samarelli, R. M. De La Rue, M. Sorel, and A. Melloni. Coherent backscattering in optical microring resonators. Applied Physics Letters, 96(8):081112, 2010.

[118] Maziyar Milanizadeh, Douglas Aguiar, Andrea Melloni, and Francesco Morichetti. Canceling thermal cross-talk effects in photonic integrated circuits. J. Lightwave Technol., 37(4):1325–1332, Feb 2019.

[119] Enxiao Luan, Hossam Shoman, Daniel M. Ratner, Karen C. Cheung, and Lukas Chrostowski. Silicon photonic biosensors using label-free detection. Sensors, 18(10, 3519), 2018.

[120] Gilberto A. Rodriguez, Shuren Hu, and Sharon M. Weiss. Porous silicon ring resonator for compact, high sensitivity biosensing applications. Opt. Express, 23(6):7111–7119, 2015.

[121] Tomoya Taniguchi et al. Detection of antibody-antigen reaction by silicon nitride slot-ring biosensors using protein g. Optics Communications, 365:16 – 23, 2016.

[122] T. Claes *et al.* Label-free biosensing with a slot-waveguide-based ring resonator in silicon on insulator. IEEE Photonics Journal, 1(3):197–204, Sep. 2009.

[123] Dongwan Kim *et al.* On-chip integrated differential optical microring refractive index sensing platform based on a laminar flow scheme. Opt. Lett., 40(17):4106–4109, Sep 2015.

[124] Liron Stern *et al.* Ultra-precise optical to radio frequency based chip-scale refractive index and temperature sensor. Optica, 4(1):1–7, Jan 2017.

[125] Patrick Steglich, Marcel Hülsemann, Birgit Dietzel, and Andreas Mai. Optical biosensors based on silicon-on-insulator ring resonators: A review. Molecules, 24(3, 519), 2019.

[126] Xiaoguang Tu, Junfeng Song, Tsung-Yang Liow, Mi Kyoung Park, Jessie Quah Yiying, Jack Sheng Kee, Mingbin Yu, and Guo-Qiang Lo. Thermal independent silicon-nitride slot waveguide biosensor with high sensitivity. Opt. Express, 20(3):2640–2648, Jan 2012.

Acknowledgements

The era of giants has (probably!) ended by the 20th century. Today's science stands on the shoulders of hundreds of thousands. We always need more collective, more collaborative and more interdisciplinary framework to do science, and without the other's support no one goes further. I have been privileged to meet and work with many great people during three years of my doctoral activities in three cities and two countries. In this section, I would like to share my sincere gratitudes to those who contributed not only to this dissertation, but also to my human side.

First and foremost, I would like to thank to Prof. Geatano Bellanca who gave me the opportunity to pursue my PhD. His greatest support, patience and providing an excellent working environment made this thesis possible. Our workday used to start in Bologna-Ferrara train at 8.15 o'clock in the morning and many times last till to midnight Skype calls. I am really thankful to be his student.

I would like to express my deepest gratitudes to my co-supervisor Prof. Paolo Bassi who was with me from the beginning and he never stopped supporting my research. He first supervised my Master's degree studies at the University of Bologna, and now this thesis. I am grateful for his invaluable inspiring guidance. On the same day he went for pension I started working at UniBo as a research fellow and I also wish for him the best in his new life.

During my PhD, I spent almost a year at the Eindhoven University of Technology, and I was extremely lucky to work with Dr. Jos van der Tol who supervised my works during my visit. I would like to express my warm thanks to him for also giving me the possibility to design my IMOS devices and thanks to this occasion, it was possible to present the results of the directional couplers and ring resonators in this thesis. This visit led fruitful collaborations, I would like to thank to Prof. Kevin Williams for allowing me to join the photonic integration group. I would like to extend my gratitudes to Dr. Yuqing, for his technical support for the IMOS mask design, to Dr. Xaveer for checking my designs of the generic InP chips, to Dr. Erwin for his advices when I was dealing with the free-space setup, to Barry for letting me attend his wet etching training in the clean room. I owe many thanks to many other colleagues; Jorn, Sander, Stefanos, Valeria, Perry, Florian, Michalis, Dan, Jeroen, Victor, Amir, Rastko, Vadim, Dzmitry, Manuel, Marija, Weiming and Marc. Thank you all of you for your great company when I was with the group.

I am grateful to my department colleagues at the University of Ferrara. I would like to thank to Prof. Davide Bertozzi for critical discussions on the scalability analysis of the presented routers. Special thanks to Andrea Balbo for providing the test SEM images. Mahdi and Hilal, thanks for being supportive for my works at Unife.

I am also indebted to Dr. Nicola Andriolli at the Scuola Superiore Sant' Anna, Pisa for his very helpful supervising of the SOI mask layout. I would also like to thank to the staff of the INPHOTEC for providing the structures. In fact, their competences in fabrication led this thesis possible, considering all the results presented regarding of SOI devices in this thesis have been obtained from a single chip.

I would like to thank to Dr. Giovanna Calò and Badrul at the University of Bari and to Dr. Marina Barbiroli, Dr. Franco Fuschini and Jacopo at the University of Bologna, and to all co-authors for strong collaborations for the project PRIN during three years.

A huge thanks to Jessica for her infinite patience to me during my PhD journey.

Finally, I would like to express my sincere thanks to those who supported me thousands of kilometres far from Bologna.

Canı gönülden beni destekleyen anneme, babama ve abime çok teşekkür ediyorum. Belki babam bu tezi göremedi ama yaşamımda bana kattığı değerler bana hala güç veriyor. Destekleriniz için çok sağolun.

<div align="right">

Ali Emre Kaplan

Bologna, March 2020

</div>

Publications List

Publications resulted from this thesis

Journal Papers

1. **Ali Emre Kaplan**, Paolo Bassi and Gaetano Bellanca, "Tunable narrow band optical reflector based on indirectly coupled micro ring resonators," submitted to OSA Optics Express (accepted, DOI: 10.1364/OE.389830).

2. **Ali Emre Kaplan**, Gaetano Bellanca, Jorn P. van Engelen, Yuqing Jiao, Jos J. G. M. van der Tol, and Paolo Bassi, "Experimental characterization of directional couplers in InP photonic membranes on silicon (IMOS)," OSA Continuum 2, 2844-2854 (2019).

Conference Contributions

1. **Ali Emre Kaplan**, Jos J. G. M. van der Tol, Paolo Bassi and Gaetano Bellanca, "Analysis of etch depth for polarization-free directional couplers," submitted to Italian Conference on Optics and Photonics (ICOP), June 9-11, 2020, Parma, Italy.

2. **Ali Emre Kaplan**, Gaetano Bellanca and Paolo Bassi, "Differential optical sensing through coupled micro ring resonators," The Thirteenth International Conference on Quantum, Nano/Bio, and Micro Technologies ICQNM, October 27- 31, 2019, Nice, France. (Best Paper Award)

3. **Ali Emre Kaplan**, Alberto Parini, Gaetano Bellanca, Paolo Bassi, Stefano Trillo, "A compact wavelength router dynamically reconfigurable through destructive interference," in Proceedings of XXVI International Workshop on Optical Wave and Waveguide Theory and Numerical Modelling, Bad Sassendorf, Germany, 2018, pp. 4-4.

4. **Ali Emre Kaplan**, Gaetano Bellanca, Jos Van Der Tol, Paolo Bassi," Coupled mode theory assessment for semiconductor codirectional couplers," in Proceedings of XXII RiNEm - Riunione Nazionale di ElettroMagnetismo, Cagliari, Italy, 2018, pp. 241 - 244.

Other Publications

Journal Papers

1. Giovanna Calò, Gaetano Bellanca, **Ali Emre Kaplan**, Paolo Bassi, Vincenzo Petruzzelli, "Double Vivaldi antenna for wireless optical networks on chip," Optical and Quantum Electronics, 50, p. 261, 2018.

2. Giovanna Calò, Gaetano Bellanca, Badrul Alam, **Ali Emre Kaplan**, Paolo Bassi, and Vincenzo Petruzzelli, "Array of plasmonic Vivaldi antennas coupled to silicon waveguides for wireless networks through on-chip optical technology - WiNOT," Opt. Express 26, pp. 30267-30277, 2018.

3. Gaetano Bellanca, Giovanna Calò, **Ali Emre Kaplan**, Paolo Bassi, and Vincenzo Petruzzelli, "Integrated Vivaldi plasmonic antenna for wireless on-chip optical communications," Opt. Express 25, pp. 16214-16227, 2017.

Conference Contributions

1. Tiziana Stomeo, Andrea Toma, Antonio Qualtieri, Giovanna Calò, Badrul Alam, Vincenzo Petruzzelli, Gaetano Bellanca, **Ali Emre Kaplan**, Massimo De Vittorio, "Silicon nitride nanoantennas for wireless on-chip optical networks", the Micro and Nano Engineering (MNE), 23-26 September 2019, Rhodes, Greece.

2. Giovanna Calò, Badrul Alam, Gaetano Bellanca, Franco Fuschini, Marina Barbiroli, Velio Tralli, Paolo Bassi, Tiziana Stomeo, Michele Bozzetti, **Ali Emre Kaplan**, Jinous Shafiei Dehkordi, Marco Zoli, Jacopo Nanni, and Vincenzo Petruzzelli "Dielectric and plasmonic vivaldi antennas for on-chip wireless communication," 21st International Conference on Transparent Optical Networks (ICTON), July 9-13, 2019, Angers, France.

3. Badrul Alam, Giovanna Calò, Gaetano Bellanca, **Ali Emre Kaplan**, Jinous Shafiei Dehkordi, Velio Tralli, Marina Barbiroli, Paolo Bassi, Marco Zoli, Jacopo Nanni, Franco Fuschini, Vincenzo Petruzzelli, "Wireless networks through on-chip optical technology: antenna design, channel modelling and link performance," 4th International Workshop on Advanced Interconnect Solutions and Technologies for Emerging Computing Systems (AISTECS), January 21, 2019, Valencia, Spain.

4. Giovanna Calo, Gaetano Bellanca, **Ali Emre Kaplan**, Franco Fuschini, Marina Barbiroli, Michele Bozzetti, Paolo Bassi, Vincenzo Petruzzelli, "On-chip wireless optical communication through plasmonic nanoantennas," in Proceedings of 12th European Conference on Antennas and Propagation (EuCAP), London, United Kingdom, 2018, pp. 599-599.

5. Giovanna Calò, Gaetano Bellanca, **Ali Emre Kaplan**, Franco Fuschini, Marina Barbiroli, Michele Bozzetti, Paolo Bassi, Vincenzo Petruzzelli, "Integrated Vivaldi antennas, an enabling technology for optical wireless networks on chip," in Proceedings of the 3rd International Workshop on Advanced Interconnect Solutions and Technologies for Emerging Computing Systems, Manchester, United Kingdom, 2018, pp.1-4.

6. Giovanna Calò, Gaetano Bellanca, Franco Fuschini, Marina Barbiroli, **Ali Emre Kaplan**, Michele Bozzetti, Badrul Alam, Paolo Bassi, Vincenzo Petruzzelli, "On-Chip wireless optical communication: from antenna design to channel modelling," in Proceedings of 20th International Conference on Transparent Optical Networks (ICTON), Bucharest, Romania, 2018, pp. 1-4.

7. Franco Fuschini, Marina Barbiroli, Marco Zoli, Paolo Bassi, Gaetano Bellanca, **Ali Emre Kaplan**, Giovanna Calò, Vincenzo Petruzzelli, "Electromagnetic propagation for on-chip wireless communications," in Proceedings of XXII RiNEm - Riunione Nazionale di ElettroMagnetismo, Cagliari, Italy, 2018, pp. 233 - 236.

8. Gaetano Bellanca, Giovanna Calò, **Ali Emre Kaplan**, Paolo Bassi, Vincenzo Petruzzelli, "Design of plasmonic antennas for wireless optical network on chip," in Proceedings of Optical Wave and Waveguide Theory and Numerical Modelling, Eindhoven, The Netherlands, 2017, pp. 2-2.

Curriculum Vitae

Ali Emre Kaplan was born on 18 August 1989 in Antalya, Turkey. He received his Bachelor's degree in Electronic Engineering majoring in Digital Electronic circuit design and RF communication from the Uludağ University in 2012 in Bursa, Turkey. During his Bachelor studies he spent six months at the Università Degli Studi di Napoli Federico II in Naples, Italy as an Erasmus exchange student. In 2012 he worked at Bosch GmbH in Bursa, Turkey as a fixed-term software engineer in Automotive sector. In 2013 he moved to Italy to study Master of Science in Electronic and Communication Science and Technology at the Alma Mater Studiorum-University of Bologna and he received his MSc degree in 2016. In the same year he began to pursue his doctoral activities at the University of Ferrara, Italy in photonic integration. In 2018 he was with the Institute of Photonic Integration of the Eindhoven University of Technology, the Netherlands as a guest researcher. He is currently with the department of Electrical, Electronic and Information Engineering, "Guglielmo Marconi", Alma Mater Studiorum-University of Bologna, working as a research fellow.

Sezioni

Università degli Studi di Ferrara

Dottorati di ricerca

Il tuo indirizzo e-mail

    aliemre.kaplan@unife.it

Oggetto:

    Dichiarazione di conformità della tesi di Dottorato

Io sottoscritto Dott. (Cognome e Nome)

    KAPLAN ALI EMRE

Nato a:

    Antalya

Provincia:

    TURCHIA

Il giorno:

    18/08/1989

Avendo frequentato il Dottorato di Ricerca in:

    SCIENZE DELL'INGEGNERIA

Ciclo di Dottorato

    32

Titolo della tesi:

    APPLICATIONS OF COUPLED RESONATORS IN PHOTONIC INTEGRATED CIRCUITS

Titolo della tesi (traduzione):

    Tesi in inglese: APPLICAZIONI DI RISUONATORI ACCOPPIATI NEI CIRCUITI FOTONICI INTEGRATI

Tutore: Prof. (Cognome e Nome)

    BELLANCA GAETANO

Settore Scientifico Disciplinare (S.S.D.)

    INF/02

Parole chiave della tesi (max 10):

    Integrated Photonic Circuits, Micro Ring Resonators, Silicon-on-insulator, Coupled resonators, Optical reflector, Optical Router, Optical sensing

Consapevole, dichiara

    CONSAPEVOLE: (1) del fatto che in caso di dichiarazioni mendaci, oltre alle sanzioni previste dal codice penale e dalle Leggi speciali per l'ipotesi di falsità in atti ed uso di atti falsi, decade fin dall'inizio e senza necessità di alcuna formalità dai benefici conseguenti al provvedimento emanato sulla base di tali dichiarazioni; (2) dell'obbligo per l'Università di provvedere al deposito di legge delle tesi di dottorato al fine di assicurarne la conservazione e la consultabilità da parte di terzi; (3) della procedura adottata dall'Università di Ferrara ove si richiede che la tesi sia consegnata dal dottorando in 2 copie di cui una in formato cartaceo e una in formato pdf non modificabile su idonei supporti (CD-ROM, DVD) secondo le istruzioni pubblicate sul sito: http://www.unife.it/studenti/dottorato alla voce ESAME FINALE – disposizioni e modulistica; (4) del fatto che l'Università, sulla base dei dati forniti, archivierà e renderà consultabile in rete il testo completo della tesi di dottorato di cui alla presente dichiarazione attraverso l'Archivio istituzionale ad accesso aperto "EPRINTS.unife.it" oltre che attraverso i Cataloghi delle

Biblioteche Nazionali Centrali di Roma e Firenze; DICHIARO SOTTO LA MIA RESPONSABILITA': (1) che la copia della tesi depositata presso l'Università di Ferrara in formato cartaceo è del tutto identica a quella presentata in formato elettronico (CD-ROM, DVD), a quelle da inviare ai Commissari di esame finale e alla copia che produrrò in seduta d'esame finale. Di conseguenza va esclusa qualsiasi responsabilità dell'Ateneo stesso per quanto riguarda eventuali errori, imprecisioni o omissioni nei contenuti della tesi; (2) di prendere atto che la tesi in formato cartaceo è l'unica alla quale farà riferimento l'Università per rilasciare, a mia richiesta, la dichiarazione di conformità di eventuali copie; (3) che il contenuto e l'organizzazione della tesi è opera originale da me realizzata e non compromette in alcun modo i diritti di terzi, ivi compresi quelli relativi alla sicurezza dei dati personali; che pertanto l'Università è in ogni caso esente da responsabilità di qualsivoglia natura civile, amministrativa o penale e sarà da me tenuta indenne da qualsiasi richiesta o rivendicazione da parte di terzi; (4) che la tesi di dottorato non è il risultato di attività rientranti nella normativa sulla proprietà industriale, non è stata prodotta nell'ambito di progetti finanziati da soggetti pubblici o privati con vincoli alla divulgazione dei risultati, non è oggetto di eventuali registrazioni di tipo brevettale o di tutela. PER ACCETTAZIONE DI QUANTO SOPRA RIPORTATO

Firma del dottorando

Ferrara, li _____30/03/2020_____ (data) Firma del Dottorando

Firma del Tutore

Visto: Il Tutore Prof. Geatano Bellanca Si approva Firma del Tutore